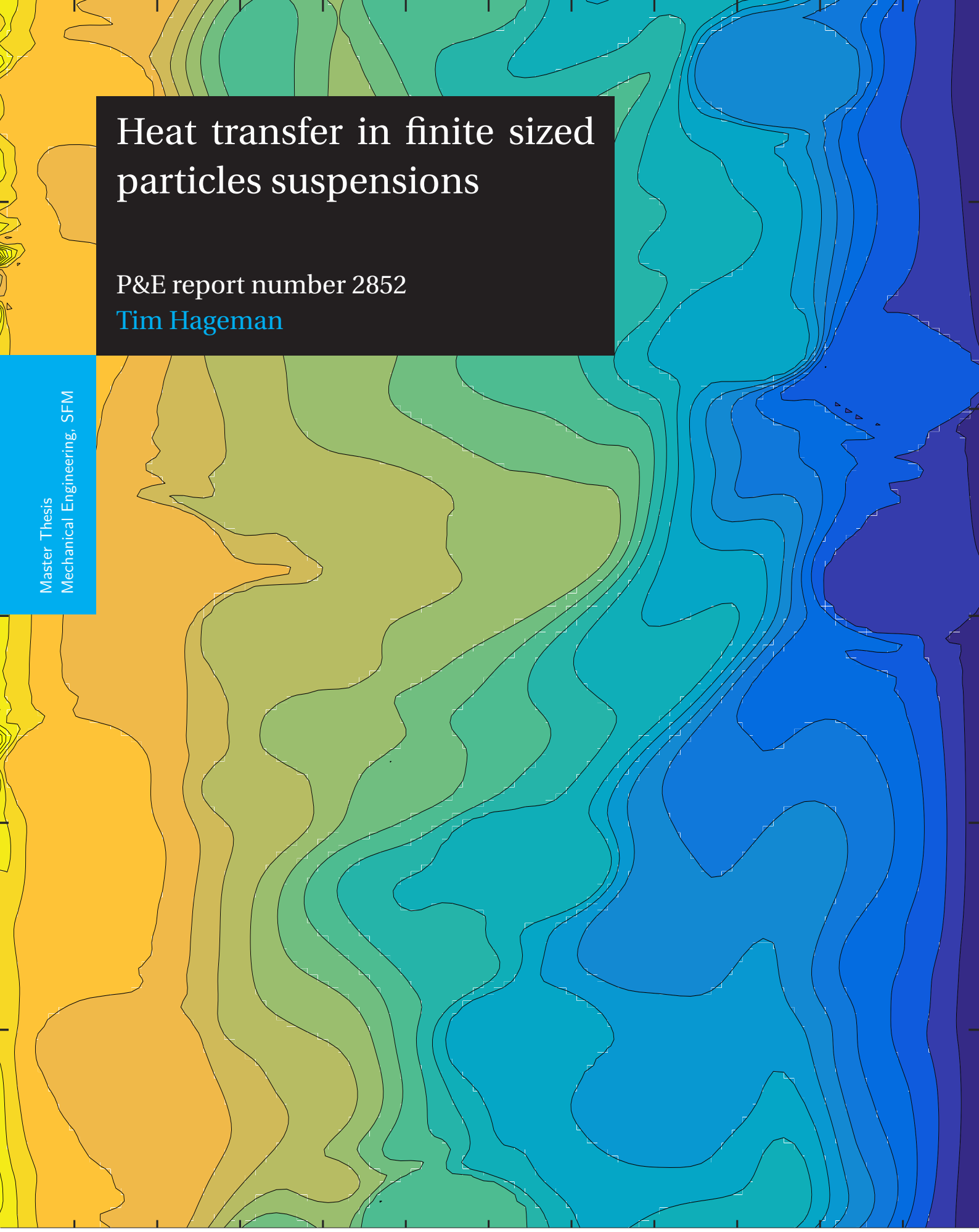

# Heat transfer in finite sized particles suspensions

P&E report number 2852

Tim Hageman

Master Thesis
Mechanical Engineering, SFM

TU Delft Delft University of Technology

Challenge the future

# ABSTRACT

Heat transfer is important in many applications. For instance, due to the decrease in size of electronics, it becomes more necessary to have efficient and smaller cooling systems. In order to increase the effect of the cooling liquids used, it might be interesting to add extra solid particles with a high conductivity, to possibly increase the effective heat transfer from the wall to the liquid. These particles can be separated in 2 categories: point particles, with a very small size compared to the flow phenomena, and finite sized particles, which due to their larger size are able to significantly influence the fluid flow. In this thesis, the finite sized particles and their effect on the effective conductivity have been analyzed by using a CFD code. The main focus has been on the effect of the mechanical and thermal Stokes numbers, which give an indication about the time required for the particles to react to changes in surrounding flow and temperature compared to the relevant flow time scale.

To investigate the effect of large particles on the effective conductivity of a fluid a numerical method to solve heat transfer inside a fluid and between fluid and particles has been implemented. This method, based on an immersed boundary method combined with DNS, is able to solve both isolated particles and extremely high conductivity particles. To solve the heat transfer for finite conductivities, a volume of fluid method has also been implemented. These methods have been verified by comparing the simulation results to known results for single sphere heat transfer and conservation of energy.

With this code, the influence of the thermal and mechanical Stokes numbers have been analyzed for laminar Couette flow. In order to gain a better understanding of the underlying heat transfer mechanics, it has been assumed that the natural convection is negligible and the density ratio between the particle and the fluid is taken to be equal to one (no effects of gravity). From this it appeared that the effective conductivity of a suspension can be split in 3 components: the non-moving conductivity, an enhancement due to fluid convection induced by the particles and an increase in heat transfer due to particle convective heat transfer.

The non-moving conductivity is only dependent on the conductivity of the particles and the fluid, and on the particle concentration. It stays close to constant independent of Stokes numbers. In contrast, the fluid convection appeared to scale significantly with the mechanical Stokes number and with the particle concentration. This appeared to be due to the increase in particle inertia resulting in more movement in wall normal direction and as a result moving more fluid in wall normal direction. The particle convection appeared to not only scale with the thermal Stokes number and the particle concentration, but also with the mechanical Stokes number. This increase was caused by the particles being able to absorb and release more thermal energy for higher thermal Stokes numbers, and thus transport more heat from the hot wall to the cold wall.

Finally the resulting effective conductivity and effective viscosity of the suspension were compared and it was shown that it is possible to enhance the heat transfer more than the viscosity, but only by either introducing a small amount of highly conductive particles, or by introducing well-conducting particles with very low mechanical Stokes numbers. It appeared to not be possible to increase the heat conductivity more than the viscosity for particles with equal or lower conductivity compared to the fluid.

# CONTENTS

# NOMENCLATURE

| | |
|---|---|
| $[]^*$ | Before correction |
| $[]^r$ | Current Runge-Kutta iteration step |
| $[]_0$ | Non-moving |
| $[]_L$ | Related to a Lagrangian point |
| $[]_f$ | Related to the fluid |
| $[]_p$ | Related to the particle |
| $\overline{[]}$ | Height averaged |

| | |
|---|---|
| $\alpha$ | Runge-Kutta time integration parameter |
| $\beta$ | Runge-Kutta time integration parameter |
| $\delta$ | Distributed delta interpolation function |
| $\kappa$ | $\frac{k}{\rho c_p}$, thermal diffusivity |
| $\nu$ | Kinematic viscosity |
| $\rho$ | Density |
| $\tau_m$ | Mechanical particle time scale |
| $\tau_{th}$ | Thermal particle time scale |
| $\theta$ | Heat flux |
| $\phi$ | Particle volume fraction |
| $\varphi$ | Phase indicator function |
| $\chi$ | interface phase indicator |
| $\Omega$ | Fluid particle interface |
| $\boldsymbol{\omega}$ | Rotation rate vector |

| | |
|---|---|
| $b$ | Thermal expansion coefficient |
| $Bi$ | $\frac{h_c D}{k_p}$, Biot number |
| $c_p$ | Specific heat capacity |
| $d_p$ | Particle diameter |
| $dx, dy, dz$ | Dimension of a single grid cell |
| $\boldsymbol{f}$ | External force |
| $Gr$ | $\frac{gb\Delta TL^3}{\nu^2}$, Grashof number |
| $H$ | Cell enthalpy |
| $I_p$ | Moment of inertia of a particle |
| $k$ | Thermal conductivity |
| $L_x, L_y, L_z$ | Dimension of the complete simulated fluid domain |
| $N$ | Number of fluid cells |
| $N_p$ | Number of particles |
| $Nu$ | $\frac{h_c d_p}{k_f}$, Nusselt number |
| $p$ | Pressure |
| $Pr$ | $\frac{\nu}{\kappa}$, Prandtl number |
| $Q$ | Total heat change for a particle per second |
| $q$ | Heat change per fluid cell per second |
| $Re$ | Reynolds number |
| $Stk$ | Stokes number |
| $T$ | Temperature |
| $\boldsymbol{u}$ | Velocity vector (u,v,w) |
| $u$ | Velocity in x direction |
| $v$ | Velocity in y direction |
| $V_p$ | Volume of a particle |
| $w$ | Velocity in z direction |

# 1

# LITERATURE STUDY

Heat transfer is important in many applications. For instance, due to the decrease in size of electronics, it becomes more necessary to have efficient and smaller cooling systems such as heat exchangers. In order to increase the effect of the cooling liquids used, it might be interesting to add extra solid particles with a high conductivity, to possibly increase the effective cooling of the heat exchanger. While the effect of these particles is quite well understood if the particles are extremely small (nanometer size) [4], the effect of larger (micro /millimeter sized) particles, which have a size able to significantly alter the flow and heat transfer profiles, is much less understood. These particles commonly have mass densities comparable to the fluid density in order to be well distributed throughout the fluid, and thus have lower conductivities than the nanometer sized particles, which can be metal particles since the density has a smaller inluence on the total distribution in the nanometer scale.

## 1.1. HEAT TRANSFER IN NANOFLUIDS

Much research has been done on the effect of nanoparticles in fluids. These particles are assumed to be small enough compared to the flow scales that they can be considered as point particles. These particles furthermore have high thermal conductivities and densities compared to the fluid. This work has not only been focused on the effect of particles on the temperature and velocity profiles in channel flow [26], but work has also been done to better understand the statistical heat transfer properties of nanofluids, which could be used to simplify calculations with nanofluids by specifying the effective parameters $c_{p,eff}$, $\rho_{eff}$, $k_{eff}$ [23] [4]. These papers show that, by introducing a small concentration of nanometer sized highly conductive particles, the thermal conductivity can be greatly enhanced.

It is further shown in [23] that increasing the diameter of these suspension particles further enhances the effective thermal conductivity. This increase has to do with the increase of the particle time scales for the mechanical and thermal response, respectively[14]:

$$\tau_m = \frac{d_p^2}{18\nu_f}\frac{\rho_p}{\rho_f} \tag{1.1.1}$$

$$\tau_{th} = 6\tau_m \frac{Pr}{Nu}\frac{c_{p,p}}{c_{p,f}} \tag{1.1.2}$$

These timescales are defined for spherical particles in the Stokes flow regime. The thermal timescale can be further simplified by assuming the heat transfer from the particles to be conduction dominated, resulting in a Nusselt number of 2. This assumption is valid as long as the velocity difference between the particle and surrounding fluid is small.

In the same paper of [14], however, it is shown that, for a turbulent flow, increasing the inertia of the particles, and thus increasing the mechanical timescale, causes the particles to be less affected by turbophoresis (movement of particles to regions of lower turbulence intensity) and thus be less concentrated near the wall compared to low inertia particles (which are more affected by turbophoresis). This decrease in concentration of highly conductive particles near the wall causes the effective heat transfer towards the flow to decrease by 14-27% [14]. This indicates that for larger particles, the thermal conductivity does not necessarily increase by introducing highly conductive particles.

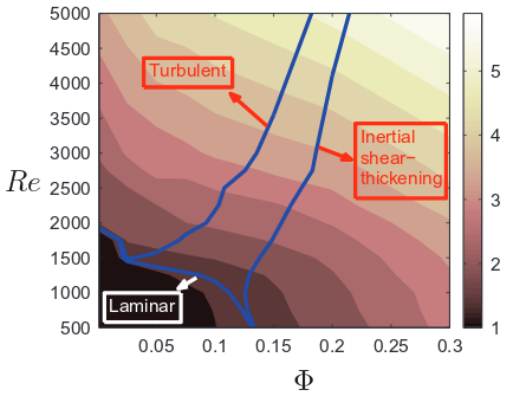


Figure 1.1: Different flow regions for finite sized particle suspensions in Poiseuille flow and estimation for the effective viscosity ratio [10].

All the articles mentioned in this subsection, however, have been regarding particles which are small compared to the lowest length scales of the flow (the Kolmogorov and Batchelor scales in a turbulent flow), and can thus be considered as point particles. Significantly less research has been done for the effects of larger particles.

## 1.2. FINITE SIZED PARTICLES

When the suspension particles become larger and the particle volume fraction increases, the particles can no longer be considered point particles. Since the particles are comparable in size to flow phenomena like eddies, the particles now significantly influence the flow. This was shown in [10], where it was noted that for high Reynolds number channel flows, the main contribution of momentum transport switches from Reynolds stresses towards particle stresses for increasing particle concentration flows. This effect was shown to cause the flow to have an extra flow regime next to laminar and turbulent flow: inertial shear thickening flow. In this regime, turbulent effects are limited to the near wall region, while the centre of the flow is dominated by a smooth, laminar like flow. The different regions, depending on Reynolds number and particle concentration, can be seen in figure 1.1.

It was shown in [15] that, for low Reynold number flows, the effective viscosity of a suspension containing finite sized particles can be described as function of the particle volume fraction and an effect due to the particle inertia. The effect of particle inertia can be estimated by an increase in the effective volume of the particle due to the formation of micro structures within the flow. The result from this is a simple equation for the effective viscosity:

$$\frac{\mu_{eff}}{\mu_f} = \left(1 + B\frac{\phi + \Delta\phi}{1 - (\phi + \Delta\phi)/\phi_{max}}\right)^2 \tag{1.2.1}$$

In this equation, B is a constant (approx. 1.25-1.5), $\phi$ is the volume fraction of the particles, $\phi_{max}$ the maximum concentration for random packed spheres ($\approx 0.6$) and $\Delta\phi$ is the extra excluded volume due to the particles forming micro-structures in the flow. In the low particle concentration, low Reynolds number (no extra excluded volume) limit, this equation becomes $\frac{\mu_{eff}}{\mu_f} = 1 + 2B\phi$. Using B=1.25, this becomes equal to the analytic solution for the dilute suspension viscosity as formulated by [6].

## 1.3. METHODS FOR SIMULATING FINITE SIZED PARTICLE SUSPENSIONS

Several methods exist for simulating the motion of a fluid with finite sized particles. These methods range in accuracy of describing the fluid motion and the ability to correctly represent the interface conditions between the particles and the fluid (see figure 1.2). In the first 3 methods mentioned in figure 1.2, the interactions between the fluid and the particles (or in case of the figure, gas bubbles) is modeled based on (semi-)empirical relations. This is required due to the resolution of chosen mesh and the solving method, while being sufficiently small to represent the overall behaviour of the mixture quite well, not being sufficient enough to be able to accurately represent the boundary interactions and small scale flow phenomena.

The fourth method mentioned in the figure is direct numerical simulation (DNS). In this method, the grid

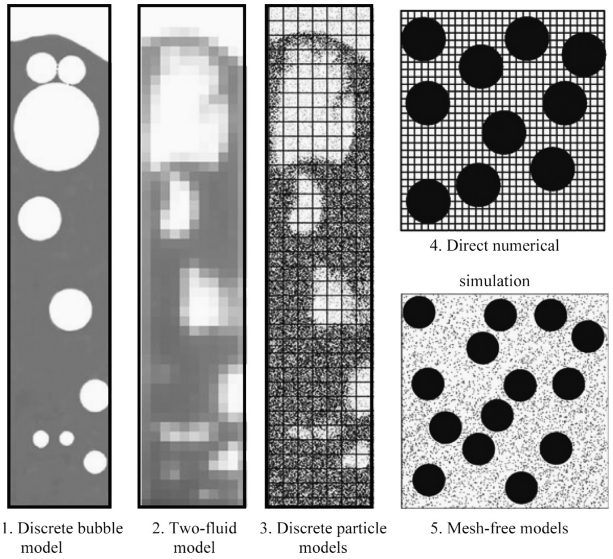


Figure 1.2: Methods for solving particle flows [5]

cells on which the fluid equations are solved are sufficiently small to be able to represent all of the fluid scales and also to accurately represent the fluid-particle interactions. The downside of this, however, is that the grid cells need to be much smaller than in the other methods, resulting in significantly more computing time. While this might be a problem for this method if used for engineering, it is not for research. The capability to fully and accurately represent all scales of the fluid motion and fully represent the particle-fluid interactions makes this method ideal for research into better understanding the physical phenomena appearing during heat and mass transfer. This knowledge can then be used to determine the relations for the interactions and the statistical mean properties of the suspension for the other methods mentioned in figure 1.2. The suspension particles can be included in DNS in two different manners: either as point particle or as finite sized particle. While for both methods the fluid phase gets completely resolved, the point particle approach models the particles by means of drag forces based on relations. In contrast, for the finite sized particles, the particle-fluid interface is completely resolved, which results in the forces acting on the particle without the need for other relations.

One final group of methods are the mesh free methods [5], in which instead of a mesh, the fluid is seeded with tracer particles flowing freely with the fluid [18]. On these tracer particles, the equations for the fluid are then solved. While these methods allow for great flexibility concerning the geometry and the amount of particles and fluid phases, the implementation is quite complex due to the large amount of interpolations needed and the boundary conditions implementation is less intuitive [18].

Considering these different methods, a DNS method is best suited to determine the effect of finite sized particles in suspensions due to being able to fully solve the flow and heat transfer, and being implementable in a physical manner which allows for creating a better understanding of the suspension mechanics. In the remainder of this section, several DNS methods will be explained and some of their advantages and disadvantages will be given.

### 1.3.1. ARBITRARY LAGRANGIAN-EULERIAN METHOD

In the arbitrary Lagrangian-Eulerian (ALE) method, a grid is used to discretize the complete fluid volume, while going around the volume occupied by the particles. If the particles in the fluid move, the grid around the particles needs to be adapted to conform to the new particle position [7]. This allows for precise control of the size of the grid cells, refining the grid near the particle boundary to better represent the boundary conditions, while allowing for a larger cell size away from the particles to limit the required amount of total grid cells needed. The downside of this, however, is that the movement of the grid involves adapted equations for the fluid phase to incorporate the moving grid and extra equations for the movement of the grid itself, which need to be solved for each time step. Furthermore, since the grid itself can deteriorate due to large movements of the solid phase (like particles flowing away from their original position), the whole domain needs to be re-meshed occasionally, which involves not only generating a new grid, but also interpolating

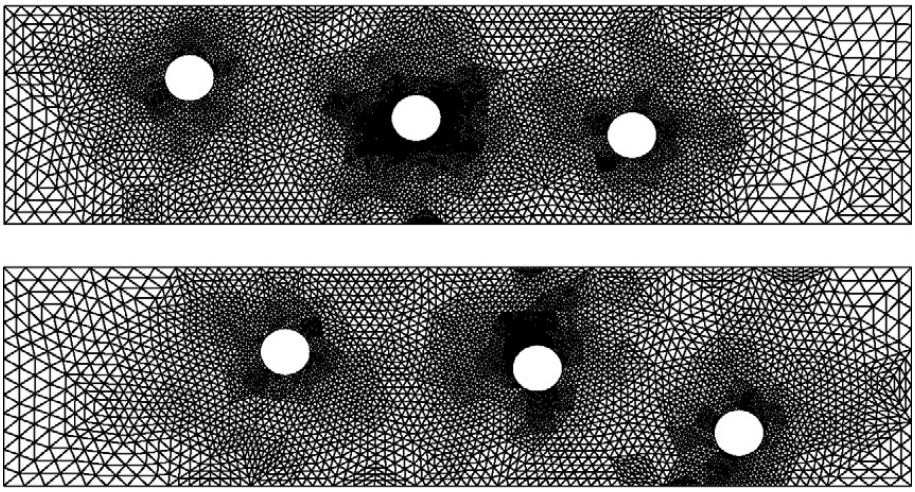

Figure 1.3: Grid used for ALE method for two different particle positions[7]

the data from the old grid onto the new grid [7]. Due to this, the ALE method is unsuitable for solving heat transfer and mass transfer for finite sized particle suspensions since the particles inside these suspensions exhibit large movements.

### 1.3.2. IMMERSED BOUNDARY METHOD

In the immersed boundary method (IBM), a Cartesian grid is used over the whole fluid domain [22]. This grid needs to be sufficiently small to be able to fully represent both the fluid movement and the boundary conditions. Due to the grid size being constant, in contrast to the ALE method, this method results in more grid cells compared to other methods. The increase in computational time due to this increase in grid cells, however, is partly lowered due to the grid being Cartesian and thus allowing for simple and efficient solvers [7].

In the IBM, the boundary condition between the particles and the fluid is applied by means of an additional force in the Navier-Stokes equations [3] and an additional heat source in the thermal energy equation [20]:

$$\rho_f \left( \frac{\partial \boldsymbol{u}}{\partial t} + (\boldsymbol{u} \cdot \boldsymbol{\nabla}) \boldsymbol{u} \right) = -\boldsymbol{\nabla} p + \mu_f \boldsymbol{\nabla}^2 \boldsymbol{u} + \boldsymbol{f} \tag{1.3.1}$$

$$\rho_f c_{p,f} \left( \frac{\partial T}{\partial t} + (\boldsymbol{u} \cdot \boldsymbol{\nabla}) T \right) = \boldsymbol{\nabla} \cdot (k_f \boldsymbol{\nabla} T) + q \tag{1.3.2}$$

The advantage of describing the boundary conditions in this manner is that the interaction force for the boundary condition is equal to the force that is exerted on the particle combined with the force exerted on

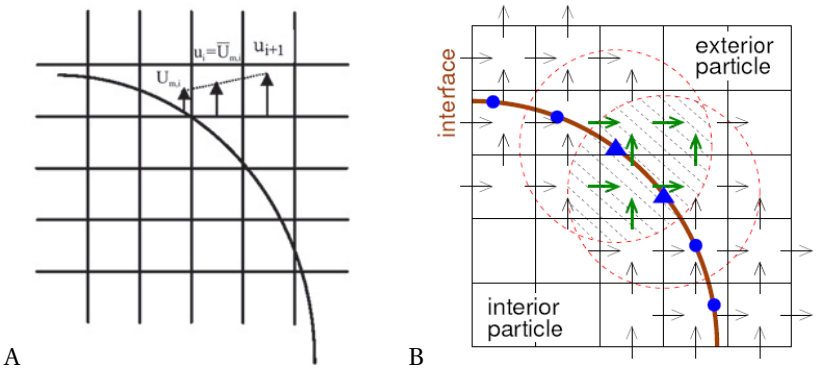


Figure 1.4: A: determining the boundary velocity by means of linear interpolation and distributing the force to the nearest fluid element [7]. B: interpolating the velocity and distributing the forces by means of a distributed delta function [3]. The blue triangles and dots represent the Lagrangian points located on the boundary, with the triangles corresponding to the two drawn interpolation kernels

the fluid occupying the particle volume. This results in the following coupling between the force exerted on the particle and the force applied to the fluid in order to fulfill the boundary conditions [3]:

$$\boldsymbol{F}_p = -\left(\int_{V_p} \boldsymbol{f}\, dV - \rho_f \frac{d}{dt}\int_{V_p} \boldsymbol{u_f}\, dV\right) \tag{1.3.3}$$

There are several options for determining the fluid velocity on the boundary, in order to calculate the required force, and the distribution of this boundary force. The most simple is to use linear interpolation between the Lagrangian boundary point and the two neighbouring fluid cells to determine the velocity (see figure 1.4), and then exert the calculated boundary force onto the nearest fluid grid cell outside the particle. While this fulfills the boundary condition, it causes oscillations in the forces each time the particle passes over a fluid cell centre and the forcing term is switched to the next fluid cell [7]. Furthermore, the direction which is used for the interpolation becomes fairly arbitrary.

A more accurate method for determining the velocity at the particle boundary and for distributing the boundary forces is to use an interpolation function [7]. This function allows for a more even spreading of the velocity and forces over a small region, lowering the oscillations due to the particle velocity. The downside of this, however, is that multiple Lagrangian boundary points can spread their force to the same fluid point. This causes the boundary condition to not be exactly fulfilled [3]. A solution to this is to apply a multidirect forcing scheme [8], in which after the boundary forces are distributed the new boundary velocities are determined and the boundary conditions are checked. If they are not fulfilled, new boundary forces are determined and distributed and added to the already distributed forces. This iterative scheme enables accurate representation of the boundary conditions.

### 1.3.3. GHOST CELL METHOD

The ghost cell method is an adaptation of the immersed boundary method, in which the forcing is not applied both inside and outside of the particle on the fluid domain, but the forcing is applied only on a fluid cell inside the particle, the so-called ghost cell [21]. In this method, ghost cells are mirrored on the particle boundary (see figure 1.5) and on these image points, the fluid properties are determined by interpolating from neighbouring points. Next, extrapolation between this mirror point and the boundary is used to determine the velocity required in the ghost cell point, which then is directly applied to the ghost cell in order to fulfill the boundary conditions on the particle boundary [21].

The advantage of directly applying a velocity on the interior ghost cell is that the boundary condition can be exactly fulfilled without the need of extrapolating forces from the particle boundary onto the fluid cells, and thus spreading the effect of the interface. One of the major disadvantages, however, is that by using cells on the edge of the particle domain the same oscillations occur as with the linear interpolation IBM [25]. Furthermore, by using linear interpolation between the image point and the ghost cell point, a linear flow profile is created in the near particle wall region, which might not be realistic. While it is possible to reduce these two disadvantages by using higher order interpolation (using more exterior fluid points),

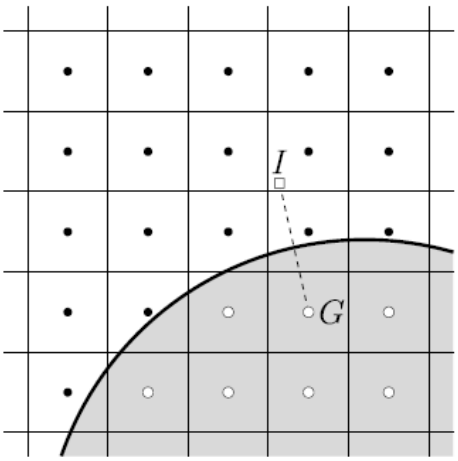


Figure 1.5: Interpolation used for the ghost cell method in which an interior fluid cell (G) is is mirrored to the point (I) on which the fluid properties are determined [2]

this will greatly increase the computational cost since this requires that data is interpolated to more points [24]. Furthermore, a disadvantage that is only increased by using higher order schemes, is that the ghost cell method is more complex to program due to not only the need of continuously updating which cells are considered the current ghost cells for the current particle position, but also due to the extrapolation of the velocity towards the ghost cell and the need for determining the exact location of all the interpolation points [24].

## 1.4. HEAT TRANSFER FOR FINITE SIZED PARTICLES

For heat transfer by means of finite sized particles an important parameter is the Biot number: the ratio of heat transfer between the fluid and particle, and inside the particle, defined as:

$$Bi = \frac{h_c d_p}{k_p} \tag{1.4.1}$$

In this equation $h_c$ is the heat transfer coefficient between the fluid and the particle. The two extreme cases of this Biot number are non conducting particles (Biot infinite) and perfectly conducting particles (Biot 0). These cause a different behaviour. For the Biot 0 particles, the large thermal conductivity causes the particle to have a uniform temperature. This results in the temperature of the fluid surrounding the particle getting forced to the particle temperature and thus the fluid directly surrounding the particle also has a uniform temperature. This furthermore causes the fluid near to a particle to display strong thermal gradients to match the particle temperature.

In contrast, for the Biot infinite particles, no heat gets transferred through the particle, and thus no temperature gradient exists in the fluid near the particle surface. The inside of the particle displays an extremely high gradient near the surface, while having a constant and uniform temperature on the inside. This results in the initial temperature of the particle not influencing the heat transfer, since no heat can be exchanged between the particle and the fluid.

### 1.4.1. COMPOSITE MATERIALS

The simplest case of heat transfer in suspensions is when there is no fluid flow and no particle movement. In this case, results developed for composite materials can be used. One of the earliest results predicting the increase in effective conductivity is from Maxwell, in which no interaction between the spherical particles is assumed, resulting in [16]:

$$\frac{k_0}{k_f} = 1 + \frac{3\phi}{\frac{k_p+2k_f}{k_p-k_f} - \phi} \tag{1.4.2}$$

When, in stead of a random particle distribution, a more even distribution is assumed, higher order approximations can be used. These approximations assume a small amount of influence between the particles. One of these models, formulated by Rayleigh, corrects the model of Maxwell by adding higher order terms, resulting in [16]:

$$\frac{k_0}{k_f} = 1 + \frac{3\phi}{\frac{k_p+2k_f}{k_p-k_f} - \phi + 1.569\left(\frac{k_p-k_f}{3k_p-4k_f}\right)\phi^{10/3} + \ldots} \tag{1.4.3}$$

A different model, which also incorporates the effects of thermal interface resistance between the particles and the fluid is formulated by Bruggeman [16]:

$$\begin{aligned} (1-\phi)^3 &= \left(\frac{k_f}{k_0}\right)^{(1+2\alpha)/(1-\alpha)} \left(\frac{\frac{k_0}{k_f} - \frac{k_p}{k_f}(1-\alpha)}{1-\frac{k_p}{k_f}(1-\alpha)}\right)^{3/(1-\alpha)} \\ \alpha &= \frac{2k_p R_{int}}{d_p} \end{aligned} \tag{1.4.4}$$

The parameter $R_{int}$ in this equation is the interface thermal resistance. A different model, based on empirical results, is the Lewis-Nielsen model. While this model does not include effects of interface resistance,

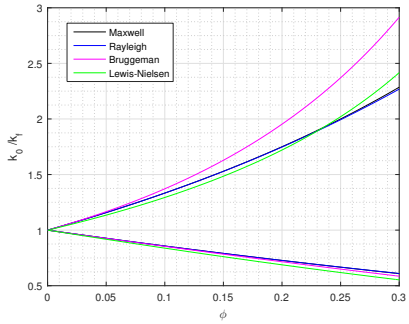


Figure 1.6: Non moving suspension conductivity as predicted by different models for composite materials for well conducting, Biot 0 particles, and for isolated, Biot $\infty$ particles.

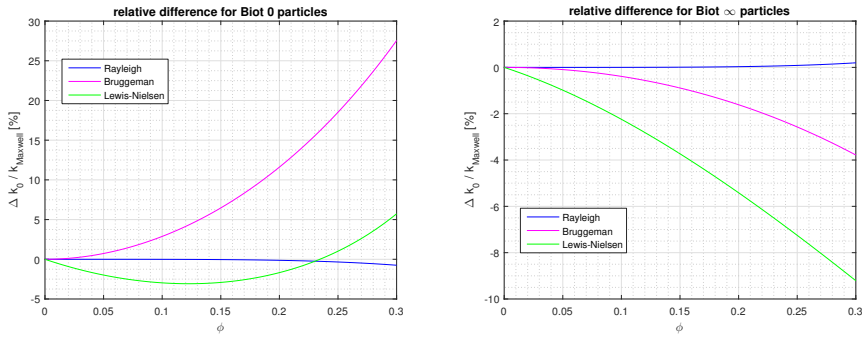


Figure 1.7: Difference between the conductivity as predicted with different composite conductivity models relative to the prediction based on the Maxwell model for well conducting, Biot 0 particles(left), and for isolated, Biot $\infty$ particles(right).

it is able to include the effects of particle size and particle pattern by introducing the maximum particle concentration[16]:

$$\begin{aligned} \frac{k_0}{k_f} &= \frac{1+AB\phi}{1-B\psi\phi} \\ B &= \frac{\frac{k_p}{k_f}-1}{\frac{k_p}{k_f}+A} \\ \psi &= 1+\left(\frac{1-\phi_{max}}{\phi_{max}^2}\right)\phi \end{aligned} \tag{1.4.5}$$

$A$ is defined as the shape factor of the particles, equal to 1.5 for spherical particles. A comparison between those models for the limiting cases of Biot 0 and Biot $\infty$ can be seen in figure 1.6, and the relative difference between the more advanced models and the model from Maxwell can be seen in figure 1.7. For the Bruggeman model, it is assumed that the contact resistance between the fluid and the particles is negligible, and for the Lewis-Nielsen model a maximum particle concentration of 60% is used, which corresponds to random loosed packed spheres.

What can be seen is that the difference between the Maxwell model and the Rayleigh model is extremely small. The difference between the Maxwell model and the other two models, however, is larger. Since, the Maxwell model is simplest in use, and does not require the interface thermal resistance (which will also not be modeled) and the maximum packing (which could range from 0.5 to 0.7 [16]), it is chosen to use this model for the rest of this master thesis when comparison to the non-moving particle conductivity is required. While this will give a rough approximation of the conductivity, it should be remembered that, depending on the particle distribution, differences up to 10% could occur for 20% particle concentrations.

### 1.4.2. HEAT TRANSFER IN SUSPENSIONS

Experimental research with regards to particle heat transfer in moving suspensions has been done by [11] with neutrally buoyant PMMA particles in a mixture of triton and water. Based on these experiments, they suggest that a linear relation exists between the effective heat transfer coefficient and the Peclet number and volume fraction. The relation they suggest is:

$$\frac{\kappa_{eff}}{\kappa_f} = 1 + \beta\phi Pe \tag{1.4.6}$$

Numerical research into the heat transfer by finite sized particles in Couette flow has been done by [1] by using an IBM to solve for the fluid and particle velocity field, and using a finite difference approach for the discretization of the heat transfer equation, combined with a volume of fluid approach for the local properties. In this volume of fluid approach, the volume fractions of the fluid and solid in the current cell are used to determine the heat conductivity of that cell. They furthermore assumed that the heat capacity per cell is constant ($\rho_f c_{p,f} = \rho_p c_{p,p}$ ).

They used this to investigate the effect of the particle inertia on the effective conductivity. While it appeared that for low particle inertia ($Re_p < 8$) the correlation mentioned in eq. 1.4.6 is approximately valid, for higher particle Reynolds numbers, and thus particle inertia, large deviations were shown from this equation. It was furthermore shown in [1] that while for low particle concentrations the main effect of the particles with regards to the effective heat conductivity is the enhanced fluid mixing caused by the presence of the particles, for larger particle concentrations, the convection of the thermal energy due to the particles itself also becomes a significant factor.

It is also shown in [1] that a similar effect exists as was shown for nanofluids [14], in which the effective conductivity for suspensions with low particle conductivity heavily depends on the particle Reynolds number, and thus on the particle inertia. For particles with conductivity up to the conductivity of the fluid itself, only an increase in effective conductivity can be reached when the particles have a high inertia, while a significant decrease in effective conductivity appears when the particles are small and thus have a low inertia. For highly conductive particles, even at low volume fractions and low particle Reynolds number, the effective conductivity was shown to always increase compared to the conductivity of the fluid.

### 1.4.3. IMMERSED BOUNDARY METHOD FOR HEAT TRANSFER

The method used to solve heat transfer with the IBM or the ghost cell method is very similar to using these methods to solve the velocity field. The only major difference is that, in contrast to the velocity field, several different boundary conditions are possible depending on the properties of the particles (high thermal conductivity, isolated particles) [17].

When the Biot number of the particles is very low, the particles can be assumed to have an uniform temperature. In this case, the IBM for the temperature distribution has only slight differences with the velocity IBM, with the only difference being one extra constant in the heat transfer equation ($\rho$ being replaced with $\rho c_p$). This does not influence the method itself, which can be applied in the same manner as the velocity IBM.

For high Biot number particles, however, the particles don't exchange any heat with the surrounding fluid. This is modeled by [17] by using an extra layer of Lagrangian points outside of the particle. The current temperature is interpolated to this point and the Lagrangian point on the surface, after which an IBM heat flux is applied on the point on the surface to force its temperature towards the temperature of the point inside the fluid. Since by distributing this heat flux to the surrounding few fluid elements by means of a discrete delta function not only the temperature on the boundary is influenced, but also the temperature of the interpolation point inside the fluid, this process needs to either be iterated until the boundary condition is fulfilled, or the outside interpolation point needs to be placed sufficiently far away from the particle surface point such that the heat flux spreading does not influence these points [17].

A different method to apply the boundary condition to the particle surface could be to directly impose that the temperature inside the particle should not change. This can be done by determining the change of internal temperature near the particle surface. At the surface, this temperature change can be compensated by creating 3 different correction terms (an imposed temperature gradient in x, y, and z direction) which then can be distributed over the surrounding fluid to force the thermal energy back to the outside of the particle. While this will fulfill the boundary condition (although, just like with all the IBM distributions, this needs to be iterated), this method has not been found in any scientific article. One possible drawback of this method is that it will create a strong, almost discontinuity like, temperature gradient at the particle interface.

This method will thus require a numerical discretization method for the fluid able to solve for discontinuous temperature distributions.

Both the IBM (using an extra shell of points in the fluid domain for the isolated particle boundary condition) and the ghost cell method, adapted for heat transfer are compared in [17]. While for a constant temperature boundary condition, the ghost cell method gives more accurate results near the boundary compared to the IBM without multidirect forcing scheme, applying the IBM with multidirect forcing significantly improves the accuracy near the boundary with just 1 extra IBM iteration. For the isolated and constant heat flux boundary conditions however, the only methods performing reasonably well are the ghost cell method and the IBM with 3 and 6 extra force iterations. What can be seen is that the IBM adapts not only the heat flux at the wall, but also inside of the fluid domain and thus on the interpolation point inside the fluid domain.This causes the IBM with six extra iterations to performs worse for the case of a constant heat flux boundary compared to the three iteration case [17] because extra energy gets added by the IBM.

## 1.5. OPEN QUESTIONS

As has been said in the above, a lot of research has already been done with regards to nanofluids [26] and the effect of their particles on the statistical heat transfer properties. For particles with a size comparable or larger than the small scale flow phenomena however, much less research has been done. Simulations have been done for dilute suspensions, in which the particles were still modeled as point particles by [9]. This point particle approach was chosen because the particle-particle interactions were negligible due to the small amount of particles. The effects of finite sized particles on the thermal conductivity has been analyzed in [11] (experimental) resulting in a relation for the average effective conductivity, but in [1] it has been shown that for more dense suspensions and for suspensions with a higher particle Reynolds number, this equation is not valid. What has not been investigated, however, is what the effect of the mechanical and thermal time scales (as defined for point particles) is on the statistical properties for finite sized particles. In [1] it is shown that some effect of particle inertia exists, but due to constraints by their assumptions, they were only able to investigate the effect of the particle size and the particle thermal conductivity, while having to keep the particle thermal capacity constant, which resulted in the thermal and mechanical time scales being coupled. No research has been done yet for finite sized particles with regards to the effects of the combination of these two time scales towards the effective thermal conductivity. The heat transfer in dense suspensions has neither been studied in much detail. Furthermore, while for heat transfer IBM studies have been done by imposing the Dirichlet boundary condition (imposed temperature on the boundary), only little is done with regards to the homogeneous Neumann boundary condition (constant heat flux or isolated particle) combined with IBM. The only applied techniques are the ghost cell method and applying an extra shell of Lagrangian points around the particle, while it has not been tried to impose that no temperature change occurs in the particle by using an extra imposed temperature gradient to force the thermal energy to return to outside the particle.

## 1.6. GOAL

The above open questions result in the following goal:

Determine if a relation exists for the statistical mean effective thermal conductivity for a dense suspension in the inertial shear thickening flow regime ($\phi \approx 0.2$) and a more dilute suspension in the laminar flow regime ($\phi \leq 0.1$) composed of finite sized spherical particles by varying the thermal and mechanical particle time scales while keeping all other properties of the flow and the particles constant. Furthermore, determine if this contribution is due to the enhanced mixing caused by the finite sized particles or if this is caused by the increase in thermal conductivity resulting from the addition of the particles or particle convective heat transfer.

In order to limit the scope, the following assumptions and limitations are made: Only particles with a density equal to the surrounding fluid density ($\rho_f = \rho_p$) are investigated, while in the flow regime in which the forced convection dominates over the natural convection ($Gr/Re^2 << 1$). Furthermore, the complete analysis will only be done for, what would be without the addition of particles, laminar Couette flow. This is the same type of flow as used in other papers by [1] [11], allowing for the results to be compared. Furthermore, this will cause a more even distribution of the particles compared to Poiseuille flow.

## 1.7. CHOSEN METHOD

In order to reach the above goal, the IBM code from [3] is adapted to be able to solve the temperature distribution for the cases of constant temperature particles, isolated particles and conducting particles. 2 methods for solving the heat transfer inside the particles, which is required for finite Biot numbers, are also implemented: One based on the volume of fluid method, the other based on the IBM with an interior particle grid. For the implementations required for these particles, first the relevant equations and boundary conditions will be determined in chapter 2. These equations are implemented in the code according to the numerical method as detailed in chapter 3.

This code will be verified by comparing the results for the following cases in chapter 4:

- Flow without particles
  - Check if a linear temperature profile is formed for both constant wall heat flux and constant wall temperature without and with a flow velocity
  - Check if a parabolic profile is formed with uniform wall heat flux boundary conditions and a distributed heat sink for all the fluid
- Single fixed particle
  - Compare heat transfer from particle with results based on heat transfer from a sphere
  - Verify correct boundary condition by having isolated walls and an initial condition in which the particle and flow have different temperatures, check if all heat is conserved and an uniform temperature is reached
  - Check if an isolated particle doesn't add any heat to the flow
- Single moving particle
  - Verify correct boundary condition by having isolated walls and an initial condition in which the particle and flow have different temperatures, check if all heat is conserved and a uniform temperature is reached
- Two colliding particles
  - Verify that collision heat transfer is working correctly (no thermal energy created or lost during the collision).
- Large amount of non moving particles
  - Compare with results for heat conductivity for composite materials (see section 1.4.1) to verify correct overall performance of the code
  - Change simulation parameters to determine limits of applied method with regards to numerical stability

The successfully validated particle simulation code will be used for Couette flow to analyze the effects of changes in thermal and mechanical time scales. The flow through a channel for multiple different combinations of these time scales for isolated particles and uniform temperature particles will be analyzed.

The method implemented for finite Biot number particles will be used to investigate if the effects that appear for both the isolated and the perfectly conducting particles also occur for more realistic particles and what the effect of the particle conductivity is on the overall heat transfer. Finally, a relation for the effective conductivity and the effective viscosity will be formulated based on the simulations, and these relations will be used to gain an insight in the effect of the mechanical and thermal timescales on the increase in conductivity compared to the increase in viscosity.

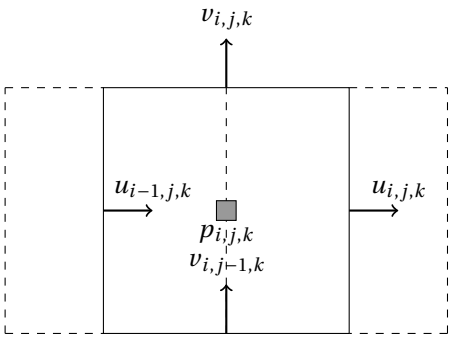


Figure 1.8: Grid cell (i,j,k) with the pressure being computed at the center of the cell and the velocities at the cell borders (with the lower borders belonging to the previous cell) by using the staggered grid (dotted line for the x-velocity cells)

## 1.8. STARTING POINT: AN ALREADY EXISTING CODE

Since the starting point is an already existing code [3] which solves the velocity and pressure within the fluid, and the rotation, velocity and location of the particles, the basis of this code will be explained here. For an overview of the code, see figure 1.10.

### 1.8.1. FLUID DISCRETIZATION

The code uses a staggered Cartesian grid. On this grid, the Navier-Stokes equations are solved. In order to do this, the forces acting on the fluid cells are determined, after which the equations are integrated using a low storage Runge-Kutta 3 scheme:

$$u^{*t+1,1} = u^{t,3} + \frac{\Delta t}{\rho_f}\left(-(\frac{32}{60})\nabla p + \frac{32}{60} rhs^{t,3}\right) \tag{1.8.1}$$

$$u^{*t+1,2} = u^{t+1,1} + \frac{\Delta t}{\rho_f}\left(-(\frac{25}{60} - \frac{17}{60})\nabla p + \frac{25}{60} rhs^{t+1,1} - \frac{17}{60} rhs^{t,3}\right) \tag{1.8.2}$$

$$u^{*t+1,3} = u^{t+1,2} + \frac{\Delta t}{\rho_f}\left(-(\frac{45}{60} - \frac{25}{60})\nabla p + \frac{45}{60} rhs^{t+1,2} - \frac{25}{60} rhs^{t+1,1}\right) \tag{1.8.3}$$

The definition of the location of the pressure and velocities is given in figure 1.8. These velocities are eventually corrected by a pressure correction scheme in order to fulfill the conservation of mass equation. Furthermore, the boundary conditions are enforced by assigning velocities to the fluid cells just outside the top and bottom wall. This allows for enforcing the no slip (or matching wall velocity) and no penetration boundary conditions.

### 1.8.2. IMMERSED BOUNDARY METHOD

The immersed boundary method forces are determined by first interpolating the velocity with a discrete delta function [7] to the Lagrangian points on the particles. Next, the IBM forces are determined on these Lagrangian particle points, after which these forces are distributed back to the fluid points:

$$U_L^* = \sum \delta_{V_f}(\boldsymbol{x} - \boldsymbol{X}_L) u^{r\,*} \tag{1.8.4}$$

$$F_x^* = \frac{U_p - U_L^*}{\Delta t(\alpha_r + \beta_r)} \tag{1.8.5}$$

$$f_x^r = \sum \delta_{V_L}(\boldsymbol{x}_b - \boldsymbol{X}_L) F_x^* \tag{1.8.6}$$

With these forces, the fluid velocities are corrected for the presence of the particles:

$$u^{p*t+1,r} = u^{*t+1,r} + f_x^r \Delta t(\alpha_r + \beta_r) \tag{1.8.7}$$

And finally, the pressure correction is applied to come to the correct velocity of the Runge-Kutta iteration step.

### 1.8.3. PARTICLE DISCRETIZATION

The particles are modeled as solid spheres. For these spheres, the velocity in the centre and the rotation around the centre are determined for each Runge-Kutta iteration step by:

$$U^{t+1,r} = U^{t+1,r-1} + F_x^r \frac{\Delta t(\alpha_r + \beta_r)}{V_p \frac{\rho_p}{\rho_f}} \tag{1.8.8}$$

$$\omega_x^{t+1,r} = \omega_x^{t+1,r-1} + M_x^r \frac{\Delta t(\alpha_r + \beta_r)}{I_p \frac{\rho_p}{\rho_f}} \tag{1.8.9}$$

The forces and moments acting on the particle are determined by:

$$F_x^r = -\left(\sum_{\Omega_p} F_x^* V_{Lagr.cell} - \sum_{V_p} \frac{u_{i,j,k}^r - u_{i,j,k}^{r-1}}{\Delta t(\alpha + \beta)} V_f (1-\varphi)\right) \tag{1.8.10}$$

$$M_x^r = -\left(\sum_{\Omega_p} (F_y^* r_y + F_z^* r_z) V_{Lagr.cell} - \sum_{V_p} \frac{v_{i,j,k}^r r_y - v_{i,j,k}^{r-1} r_y + w_{i,j,k}^r r_z - w_{i,j,k}^{r-1} r_z}{\Delta t(\alpha + \beta)} V_f (1-\varphi)\right) \tag{1.8.11}$$

In which the first term is the force or moment originating from the IBM force applied to fulfill the boundary condition, and the second term is a correction due to the ghost-fluid, the fluid in the cells occupied by the particle, also being influenced by the IBM force.

The particle position gets updated by means of central Euler time integration:

$$X_p^{t+1,r} = X_p^{t+1,r-1} + \Delta t(\alpha_r + \beta_r) \frac{U^{t+1,r} + U^{t+1,r-1}}{2} \tag{1.8.12}$$

Similar equations as described here for the velocity and displacement in x direction, and the rotation around the x axis are used for the other directions. The code also includes a model for the collision between particles and the behaviour of the fluid when particles get very close to each other. However, since these models are not necessary to understand the working of the already existing code, and to understand the additions made to this code to be able to solve the heat transfer, these models will not be explained here.

### 1.8.4. PARALLELIZATION

Since this code is a DNS code, it requires the fluid cells to be smaller than relevant flow phenomena to resolve all the relevant scales. This means that the grid cells get very small, and thus a lot of grid cells are used. In order to be able to do this, the code is written in such a manner that it can be run on multiple cores. For the fluid domain, this is done by splitting up the fluid domain in equally sized smaller parts. One core solves the fluid equations for one part of this total domain. In order to do this, it is necessary for the core to not only know the information of the grid cells in the domain that is being solved itself, but it is also necessary to know information about the surrounding cells. To give this information, a so called halo (see figure 1.9) is used. This is a shell of cells around the core its fluid domain, which are being solved by different cores. This halo

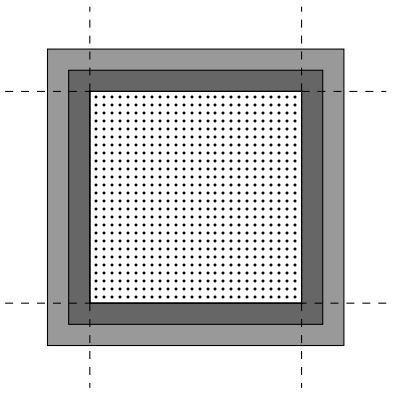

Figure 1.9: Fluid domain of a single core top view (dotted area) with the halo required for the fluid integration (dark grey) and the IBM force iterations (dark and light grey)

gets updated by sending information from the core solving the neighbouring fluid domain to the core solving this fluid domain. This is done each time before the fluid equations are solved.

For the interpolation of the fluid velocity towards the Lagrangian particle points a larger halo is necessary, since the interpolation function uses information from up to 1.5 cells away. This thicker halo is updated before each IBM force iteration. Furthermore, since the forces are also distributed up to 1.5 cells away from the current points, the forces applied to the halo need to be send to the relevant core and summed up to the other forces for those cells.

The particles are assigned to a core (a so called particle master) which contains the fluid domain they are located in. When the particles move, and they end up in a different fluid domain, all relevant information is transferred from the current core to the new core. It is also required, however, to provide information about Lagrangian points which are outside the current fluid domain of the particle master to the cores that calculate the information for this domain. In order to do this, the Lagrangian points of a a particle are distributed over the domains based on where they are located. During this distribution, not only the locations get assigned to different cores, but also the velocity of these Lagrangian points (dependent on the particle velocity and rotation rate) are assigned to these points. To do this, it is required that the master not only sends information to the neighbouring cores about the location of particles, but the particle master also sends the velocity and rotation rate to the relevant cores.

Finally, once the IBM forces of all Lagrangian points are determined, the total sum over all Lagrangian points in the fluid domain of the moments and forces acting on the particle are send to the particle master. This particle master then sums up the information send from the up to 3 other cores, and finally performs the integration for the particle velocity, position and rotation rate.

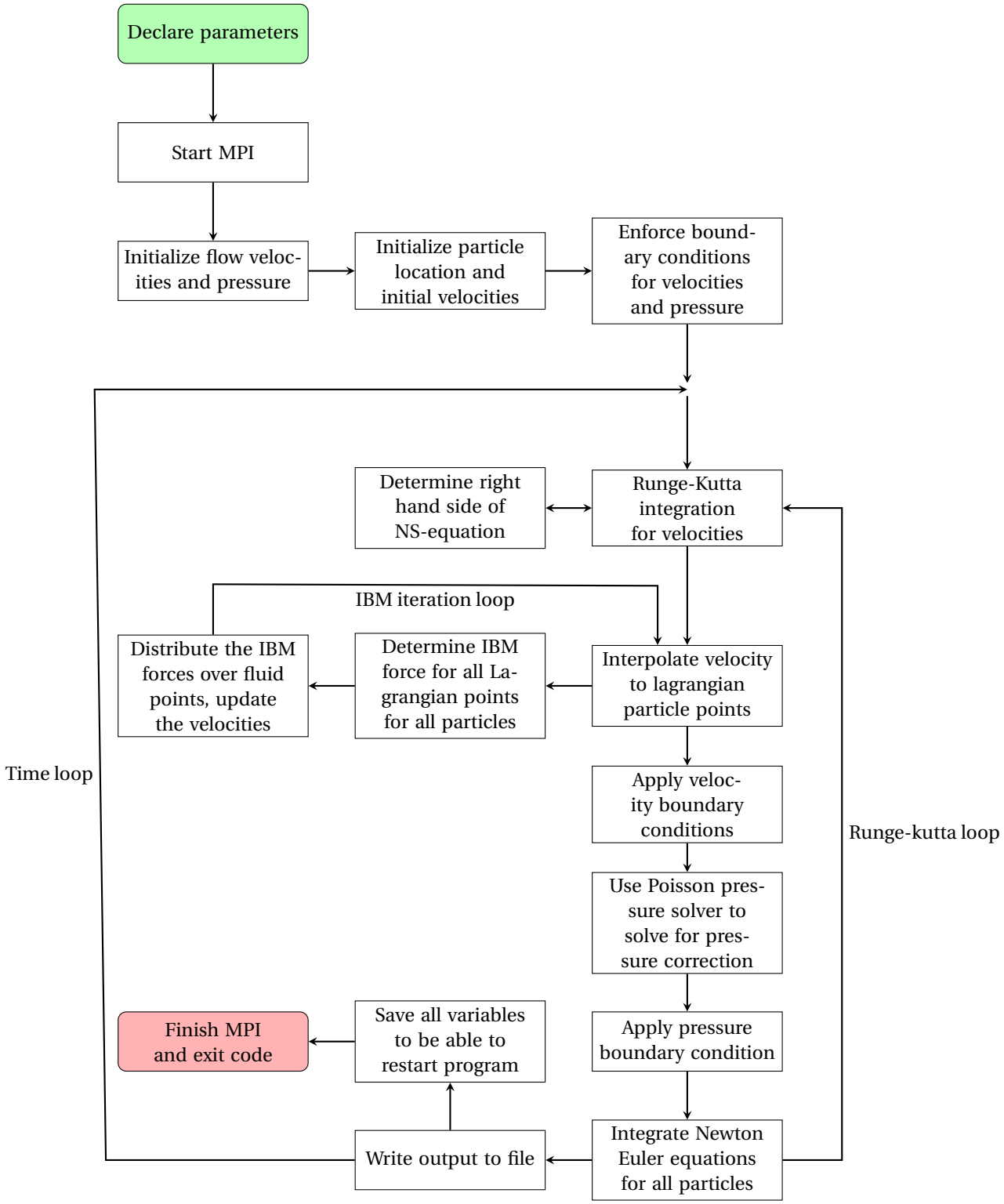


Figure 1.10: Program structure of the already existing CFD code

# 2

# EQUATIONS

In this chapter, the equations for the velocity and temperature will be given. Furthermore, the boundary conditions will be given.

## 2.1. MOTION EQUATIONS

These equations are already implemented in the code. The equations of motion are composed of the Navier-Stokes equations for the fluid:

$$\frac{\partial \boldsymbol{u}}{\partial t} + (\boldsymbol{u}\cdot\boldsymbol{\nabla})\boldsymbol{u} = -\frac{1}{\rho_f}\boldsymbol{\nabla} p + \nu_f \boldsymbol{\nabla}^2 \boldsymbol{u} + \boldsymbol{f} \tag{2.1.1}$$

$$\boldsymbol{\nabla}\cdot\boldsymbol{u} = 0 \tag{2.1.2}$$

And the Newton-Euler equations for the particle motion:

$$\rho_p V_p \frac{d\boldsymbol{U}_p}{dt} = -\rho_f \int_{V_p} \boldsymbol{f}\, dV + \rho_f \frac{D}{Dt}\int_{V_p} \boldsymbol{u} dV \tag{2.1.3}$$

$$I_p \frac{d\boldsymbol{\omega_p}}{dt} = -\rho_f \int_{V_p} \boldsymbol{r}\times\boldsymbol{f}\, dV + \rho_f \frac{D}{Dt}\int_{V_p} \boldsymbol{r}\times\boldsymbol{u} dV \tag{2.1.4}$$

### 2.1.1. BOUNDARY CONDITIONS

Fluid-wall no slip and no penetration boundary conditions:

$$u_x\big|_{wall} = u_z\big|_{wall} = 0 \tag{2.1.5}$$

$$u_y\big|_{wall} = v_{wall} \tag{2.1.6}$$

Fluid-particle no slip boundary conditions:

$$\boldsymbol{u}_f = \boldsymbol{U}_p + \boldsymbol{\omega}_p \times \boldsymbol{r} \tag{2.1.7}$$

## 2.2. HEAT TRANSFER EQUATIONS

The still to be implemented equations are the advection diffusion equation for the heat transfer in the fluid:

$$\rho_f c_{p,f}\left(\frac{\partial T_f}{\partial t} + (\boldsymbol{u}\cdot\boldsymbol{\nabla})T_f\right) = k_f \boldsymbol{\nabla}^2 T_f + q \tag{2.2.1}$$

The equations for the uniform temperature particles is given by:

$$\rho_p c_{p,p} V_p \frac{dT_p}{dt} = Q \tag{2.2.2}$$

While the equations for the finite Biot particles is given by:

$$\rho_p c_{p,p}\left(\frac{\partial T_p}{\partial t} + ((\boldsymbol{U_p} + \boldsymbol{\omega_p}\times\boldsymbol{r_p})\cdot\boldsymbol{\nabla})T_p\right) = \boldsymbol{\nabla}\cdot(k_p\boldsymbol{\nabla}T) + q \tag{2.2.3}$$

### 2.2.1. BOUNDARY CONDITIONS

Fluid-wall boundary conditions:

Isothermal wall:

$$T_f\big|_{wall} = T_{wall} \tag{2.2.4}$$

Constant heat flux or isolated wall:

$$(-k_f \boldsymbol{\nabla} T) \cdot \boldsymbol{n}\big|_{wall} = q_{wall} \tag{2.2.5}$$

Fluid-particle boundary condition:

Biot=0 (uniform particle temperature):

$$T_p = T_f \tag{2.2.6}$$

Biot=$\infty$ (isolated particle):

$$(k_f \boldsymbol{\nabla} T_f) \cdot \boldsymbol{n_p} = 0 \tag{2.2.7}$$

Finite Biot (conducting particles):

$$T_p = T_f \qquad and \qquad (k_f \boldsymbol{\nabla} T_f) \cdot \boldsymbol{n_p} = (k_p \boldsymbol{\nabla} T_p) \cdot \boldsymbol{n_p} \tag{2.2.8}$$

The fluid-particle boundary conditions are applied by using the heat flux terms in the equations for the fluid (q) and particles (Q). These 2 heat fluxes are coupled for Biot 0 particles by:

$$Q = -\left( \int_{\Omega} q_L dS - \int_{V_p} \rho_f c_{p,f} \frac{DT_f}{Dt} dV \right) \tag{2.2.9}$$

In this equation, $q_L$ is the heat flux being prescribed on the fluid before distributing this heat flux from the particle boundary towards the surrounding fluid elements. The second integral represents the extra heat added to the fluid occupying the same space as the particle, which is deduced from the total added heat in order to determine the heat flux from the particle to the fluid in the fluid domain.

# 3

# NUMERICAL METHOD

For the space discretization, the same grid is used as for the already existing fluid velocity solver. The temperature of each fluid cell is defined in the cell centre. The location of each cell is described with the subscript i,j,k , in which i is the cell number in x direction, j in y direction and k in z direction. Furthermore, the boundary conditions are defined at the bottom of cell i,j,1 for the lower wall and at the top of cell i,j,ktop for the top wall, by describing either a temperature or a flux at these cell edges.

## 3.1. DISCRETIZED EQUATIONS

The thermal energy equation (eq. 2.2.1) can be discretized by using a finite volume method combined with a central difference method for the space discretization, and the same third order low storage Runge-Kutta scheme as is used in the current code for the velocity field [3]. This results in:

$$T^{r*} = T^{r-1} + \alpha_r \Delta t RHS^{r-1} + \beta_r \Delta t RHS^{r-2} \tag{3.1.1}$$

For the first Runge-Kutta step (r=1) $T^{r-1} = T^n$, $RHS^{r-1} = RHS^n$ and the coefficients for the Runge-Kutta scheme are: $\alpha_1 = 32/60, \beta_1 = 0, \alpha_2 = 25/60, \beta_2 = -17/60, \alpha_3 = 45/60$ and $\beta_3 = -25/60$.

The expression for the right hand side can be determined by using a finite volume discretization resulting in:

$$RHS = (\theta_x + \theta_y + \theta_z) \tag{3.1.2}$$

with:

$$\theta_x = \kappa\left(\frac{T_{i+1,j,k} - 2T_{i,j,k} + T_{i-1,j,k}}{dx^2}\right) + \frac{(u_{i-1,j,k})(T_{i-1,j,k} + T_{i,j,k}) - (u_{i,j,k})(T_{i+1,j,k} + T_{i,j,k})}{2dx} \tag{3.1.3}$$

In this equation, $\kappa = \frac{k_f}{c_{p,f}\rho_f}$ and this equation can be used in a similar manner for the heat flux in y and z direction.

While this works for the uniform temperature particles, since these will result in a continuous temperature profile, this space discretization will result in oscillations for the isolated particles, which will have discontinuous temperature jumps between the inside and outside of the particle. In order to resolve this, a second order upwind discretization is also implemented for the fluid convection term, resulting in:

$$\begin{aligned}\theta_x = \kappa\left(\frac{T_{i+1,j,k} - 2T_{i,j,k} + T_{i-1,j,k}}{dx^2}\right) &+ \frac{u_{i-1,j,k}(\psi_- T_{i-1,j,k} + (1-\psi_-)T_{i,j,k}) - u_{i,j,k}((1-\psi_+)T_{i+1,j,k} + \psi_+ T_{i,j,k})}{dx} \\ &+ \gamma\frac{u_{i-1,j,k}\big(\psi_-(T_{i-1,j,k} - T_{i-2,j,k}) + (1-\psi_-)(T_{i,j,k} - T_{i+1,j,k})\big)}{2dx} \\ &- \gamma\frac{u_{i,j,k}\big((1-\psi_+)(T_{i+1,j,k} - T_{i+2,j,k}) + \psi_+(T_{i,j,k} - T_{i-1,j,k})\big)}{2dx}\end{aligned} \tag{3.1.4}$$

The variables $\psi_-$ and $\psi_+$ are either equal to one if the corresponding velocity at the cell edge is positive, or 0 if the velocity is negative, and $\gamma$ is one except when the fluid cell and its neighbour display large temperature

gradients. In this case, $\gamma$ is set to be 0, which causes the first order upwind scheme to be used locally. This scheme is, just like the central difference scheme, second order accurate, with the exception of the places where for stability reasons the first order upwind discretization is applied.

With this estimate for the temperature, the IBM heat flux can be determined after which the actual temperature can be determined by:

$$T^r = T^{r*} + \Delta t(\alpha_r + \beta_r)\frac{q^r}{\rho_f c_{p,f}} \tag{3.1.5}$$

The same discretization can be applied to the particles (only required for Biot=0) resulting in:

$$T_p^r = T_p^{r-1} + \frac{\Delta t(\alpha_r + \beta_r)}{\rho_p c_{p,p} V_p} Q^r \tag{3.1.6}$$

## 3.2. BOUNDARY CONDITION IMPLEMENTATION

The wall boundary conditions can be directly included in the equation for the RHS by substituting the terms for the heat transfer in z direction by the following expression for an isolated or constant heat flux top wall:

$$\theta_z \Rightarrow \kappa\left(\frac{-T_{i,j,k} + T_{i,j,k-1}}{dz^2}\right) + \frac{(w_{i,j,k-1})(T_{i,j,k-1} + T_{i,j,k})}{2dz} + \frac{q_{wall}}{\rho_f c_{p,f} dz} \tag{3.2.1}$$

For a constant temperature top wall the expression for the RHS becomes:

$$\theta_z \Rightarrow \kappa\left(\frac{2T_{wall} + T_{i,j,k-1} - 3T_{i,j,k}}{dz^2}\right) + \frac{(w_{i,j,k-1})(T_{i,j,k-1} + T_{i,j,k})}{2dz} \tag{3.2.2}$$

The same can be done for the lower wall. In these equations, the no-penetration wall boundary condition is already included by removing the advective heat flux terms at the top of the cell.

## 3.3. IBM HEAT FLUX TERM

### 3.3.1. UNIFORM TEMPERATURE PARTICLE (ZERO BIOT CASE)

For the case that the Biot number of the particle is very low, the boundary condition that needs to be fulfilled is that the temperature of the fluid on the particle boundary is equal to the temperature of the particle. This can be done by first interpolating the fluid temperature to each Lagrangian particle point:

$$T_L^* = \sum \delta_{V_f}(\boldsymbol{x} - \boldsymbol{X}_L) T^{r*} \tag{3.3.1}$$

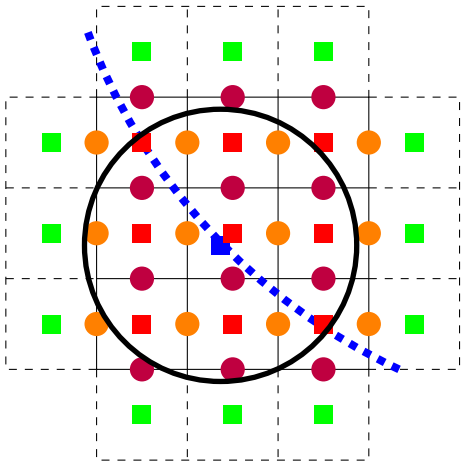

Figure 3.1: Fluid cells influenced by spreading of the IBM heat flux for single temperature particles (only red squares) and the IBM temperature gradient for isolated particles (red and green squares) from the Lagrangian point on the particle (blue square). The dots are the points to which the temperature gradients in x direction (orange dots) and in y direction (pink dots) are spread, which then influence the fluid points. Black circle indicates the range of the discrete regularized delta interpolation/spreading function for the shown Lagrangian point (blue dot).

After which an IBM heat flux correction can be determined based on the temperature difference between the Lagrangian point fluid temperature and the particle temperature:

$$Q^* = \rho_f c_{p,f} \frac{T_p - T_L^*}{\Delta t(\alpha + \beta)} \tag{3.3.2}$$

Which can then be distributed over the surrounding fluid cells using the same function as used for the fluid temperature interpolation:

$$q^r = \sum \delta_{V_L}(\boldsymbol{x} - \boldsymbol{X}_L) Q^* \tag{3.3.3}$$

In which $\delta_{V_L}(\boldsymbol{x} - \boldsymbol{X}_L)$ is the discrete regularized delta function used for the interpolation between the fluid points and the particle points. With this $q^r$ the final fluid temperature can be determined by 3.1.5. After determining this temperature, the above process can either be repeated to come to a more exact estimate, which better fulfills the boundary conditions, or, if the boundary conditions are sufficiently accurate, the total heat flux of the particle can be determined. It is required to iterate this to get a more exact boundary condition due to the overlap between interpolations and thermal energy spreading because of the discrete regularized delta function influencing cells up to 1.5 cell away. This causes the Lagrangian points to influence each other, resulting in that even though the amount of thermal energy distributed should force the temperature towards the particle temperature, the energy spread from neighbouring Lagrangian particle points results in this not being exact.

Once the IBM iterations are completed, the total heat change felt by the particle can be determined by:

$$Q^r = -\left( \sum_{\Omega_p} Q^* V_{Lagr.cell} - \sum_{V_p} \rho_f c_{p,f} V_f \frac{T^r_{i,j,k}\varphi^r_p - T^{r-1}_{i,j,k}\varphi^{r-1}_p}{\Delta t(\alpha + \beta)} \right) \tag{3.3.4}$$

After which this total heat flux can be used to update the particle temperature. In this expression, the first term is the total heat applied to both the fluid and the ghost fluid. The second term corresponds to the thermal energy change in the ghost fluid during the Runge-Kutta step and thus is subtracted to come to the heat flux applied from the particle to only the fluid domain.

### 3.3.2. ISOLATED PARTICLE (INFINITE BIOT CASE)

For an isolated particle, the boundary condition that has to be fulfilled is that no temperature change appears for the fluid elements inside the particle domain (the ghost fluid). In order to do this, the current and preferred temperatures are extrapolated to the particle boundary (see figure 3.2 for relevant cells):

$$T^*_{L,now} = \sum 2\delta_{V_f}(\boldsymbol{x} - \boldsymbol{X}_L) T^{r\,*} \varphi_p \tag{3.3.5}$$

$$T_{L,pref} = \sum 2\delta_{V_f}(\boldsymbol{x} - \boldsymbol{X}_L) T_{pref} \varphi_p \tag{3.3.6}$$

In which $\varphi_p$ indicates if the current element is inside the fluid ($\varphi_p = 0$) or particle ($\varphi_p = 1$) domain. Both the current fluid temperature and the preferred (constant) particle temperature are interpolated to reduce the error caused by using the interpolation only inside the particle. This preferred temperature is the temperature of the fluid underneath the particle when the particles and fluid are initialized at the beginning of the code. While this interpolation function only gives an approximation of the actual value if used one sided, by also interpolating the constant preferred temperature (which is also the internal fluid temperature that should be obtained for isolated particles) this function can be used without large errors.

These interpolated temperatures should be equal to each other once the IBM iterations are completed. To do this, a temperature gradient is determined at the particle surface. This gradient should force the heat that entered the particle during the fluid temperature solver to outside the particle, while conserving thermal energy. This temperature gradient, normal to the particle surface, can be determined by:

$$(\boldsymbol{\nabla} T \cdot \boldsymbol{n}_p)_{cor} = \frac{T_{L,pref} - T^*_{L,now}}{(\alpha + \beta)\Delta t} \frac{dx}{\kappa} \tag{3.3.7}$$

This temperature gradient can then be split in x, y and z components by multiplying them with the unit normal vector to the particle:

$$\boldsymbol{\nabla} T_{cor} = (\boldsymbol{\nabla} T \cdot \boldsymbol{n}_p)_{cor} \boldsymbol{n}_p \tag{3.3.8}$$

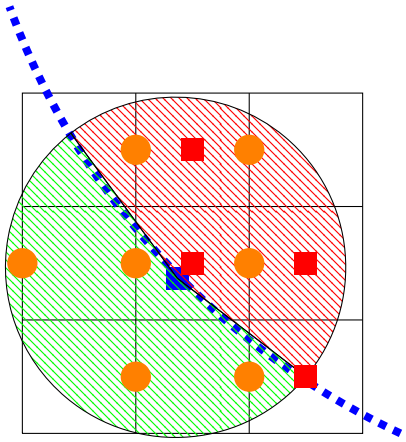

Figure 3.2: Example for the one sided interpolation region (shaded red) for the Biot infinite numerical method, the cells which are used for the temperature interpolation (red squares), the region to which the x temperature gradients are spread (red and green shaded) and the cell edges affected by the spreading (orange dots).

These gradients in x, y and z direction are then interpolated to the fluid cell edges both inside and outside the particle, where they influence two fluid cells, one of which looses thermal energy due to the gradient, and the other which obtains thermal energy.

$$dTdx_{cor}\big|_{xb} = \delta_{V_L}(\boldsymbol{x}_b - \boldsymbol{X}_L)(\boldsymbol{\nabla} T_{cor} \cdot \boldsymbol{n}_x) \tag{3.3.9}$$

This equation can be applied in a similar manner for dTdy and dTdz for all the y and z boundaries. From these gradients, the correction of the heat flux per cell can be determined using a finite volume approach to sum up the temperature gradients applied to the cell edges:

$$C = \kappa\left(\frac{dTdx_{cor}\big|_{-xb} - dTdx_{cor}\big|_{xb}}{dx} + \frac{dTdy_{cor}\big|_{-yb} - dTdy_{cor}\big|_{yb}}{dy} + \frac{dTdz_{cor}\big|_{-zb} - dTdz_{cor}\big|_{zb}}{dz}\right) \tag{3.3.10}$$

In which only the cells influenced by the spreading (see figure 3.1) are calculated. With this correction, the change in heat flux caused by the isolated particles can be determined by summing up all the contributions from all the Lagrangian particle points:

$$\frac{q^r}{\rho_f c_{p,f}} = \sum C \tag{3.3.11}$$

With this extra heat exchange determined, the new temperatures at the fluid cell centers can be determined and either the above process can be repeated to more accurately represent the boundary conditions, or the next Runge-Kutta iteration step can be started, since for isolated particles, there is no need to update the particle temperature.

This ensures that no heat is added or removed to the fluid, and that all the heat that initially, due to the fluid temperature solver, gets removed from the flow, gets re-added to the approximate same location. Due to the formulation using the gradients, this furthermore ensures that no heat is created or destroyed and if a small error still exists after the IBM iteration, this remaining heat gets removed in the next IBM loop.

In order to prevent large fluid temperature discontinuities due to the presence of the isolated particle, a new particle temperature is defined based on the particle position every few hundred time steps. When this is done, not only the particle temperature changes, but also the temperature of the fluid underneath the particle is adapted to prevent the particle from absorbing or releasing any thermal energy. The precise amount of time steps between these corrections is dependent on how much the particles move perpendicular. An as large as possible time in between corrections will ensure that the leftover heat from the previous IBM correction will get removed as much as possible, while a small time between corrections will reduce the size of the discontinuity in the fluid temperature field, which will increase the stability of the fluid temperature solver.

### 3.3.3. PARTICLE-WALL INTERACTIONS

Since the interpolation function requires the fluid temperature from up to 1.5 cells away, it is required to define the temperatures inside of the wall. To do this, two extra planes of fluid cells are added below the i,j,1

and above the i,j,ktop cell planes. These 4 additional planes are not updated with the fluid temperature solver, but instead are directly assigned the wall temperature. This wall temperature is either a constant value for a constant temperature wall, or the value of the fluid cell above the wall to enforce the no thermal gradient at the wall boundary condition. This causes the wall, from the perspective of the Lagrangian particle points, to behave as having a uniform temperature throughout its complete thickness.

The interpolation function is also used for the spreading of the thermal energy. The implementation of this is different depending on the wall boundary condition. For the isolated wall boundary condition the thermal energy that would be distributed to cells inside the wall is pushed up into the fluid domain. This makes the wall act as if it is not absorbing any heat, while assisting with the fluid cell stuck between the wall and the particle to quickly adapt its temperature to the particle temperature. In contrast, for a uniform temperature wall the IBM heat fluxes applied to the wall are added to the total thermal energy transported from the wall to the fluid. This means that the particles themselves are able to conduct heat directly to the wall if they come within 1.5 cells distance. After the complete IBM iteration loop, the wall temperatures are reassigned to fit with either the constant wall temperature, or isolated wall bounary condition.

## 3.4. STABILITY

In this section, the stability of the heat coupling between the particle and the fluid for the Biot 0 particles is examined. Since the new fluid temperature surrounding the particle is forced towards the old particle temperature, and based on this heat flux the particle temperature is updated, the coupling is explicit. This could create instabilities when low heat capacity ratios between the particle and fluid are chosen.

In order to investigate this, a few simplifications are made. First it is assumed that the heat transfer from the particle towards the fluid is large compared to the conductive heat transfer in the fluid. The initial conditions are chosen to be a uniform fluid temperature (both the fluid and the ghost fluid) and a temperature difference between the fluid and particle of $\Delta T_{old}$. Furthermore, to simplify the interpolation function, the position of all the Lagrangian points is assumed to be on fluid cell boundaries, resulting in the interpolation of the temperature and distribution of the thermal energy to only be dependent on 2 fluid cells in x, y and z direction (see figure 3.3). This allows to describe the volume of the particle itself and the affected fluid as:

$$V_p = \frac{4}{3}\pi r_p^3 \tag{3.4.1}$$

$$V_f = \frac{4}{3}\pi\left((r_p + dx)^3 - (r_p - dx)^3\right) \tag{3.4.2}$$

The heat capacity of the complete particle and the affected fluid can then be described as:

$$C_{p,p} = \rho_p c_{p,p} \cdot \frac{4}{3}\pi r_p^3 \tag{3.4.3}$$

$$C_{p,f} = \rho_f c_{p,f} \cdot \frac{4}{3}\pi\left(2dx^3 + 6dx r_p^2\right) \tag{3.4.4}$$

Assuming a temperature difference $\Delta T_{old}$ between the fluid and the particle, the heat transferred by the particle to the fluid to fulfill the Biot 0 particle boundary condition is equal to:

$$Q = C_{p,f}\Delta T_{old} \tag{3.4.5}$$

This heat transfer results in a thermal energy change in the particle of $\frac{1}{2}Q$, the other half of the energy being applied to the ghost fluid. This corresponds to equation 3.3.4, with the integral over the Lagrangian points

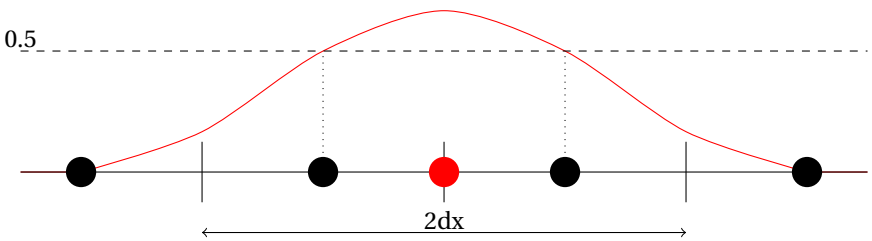


Figure 3.3: Assumption made for determining the stability with regards to the location of the fluid cell centres (black circles) and the Lagrangian particle points (red circle) causing the discrete delta interpolation function (red line) to only influence two fluid points.

being equal to $Q$, and the ghost fluid temperature change integral being $\frac{1}{2}Q$. This heat flux causes the fluid and ghost fluid temperature to be equal to the old particle temperature, and new temperature difference between the particle and the fluid ($\Delta T_{new}$) when the temperature of this particle is updated of:

$$\frac{\Delta T_{new}}{\Delta T_{old}} = \frac{\frac{1}{2}Q}{C_{p,p}} \frac{1}{\Delta T_{old}} = \frac{\rho_f c_{p,f}}{\rho_p c_{p,p}} \left( \left( \frac{dx}{r_p} \right)^3 + 3 \frac{dx}{r_p} \right) \tag{3.4.6}$$

This ratio, in order for the temperature difference between the particle and the fluid to decrease during the time steps, needs to be smaller than 1, resulting in the following criterion for the stability:

$$\frac{\rho_p c_{p,p}}{\rho_f c_{p,f}} > \left( \frac{dx}{r_p} \right)^3 + 3 \frac{dx}{r_p} \tag{3.4.7}$$

Using this criterion for the values for $\frac{dx}{r_p}$ 1/8, 1/16 and 1/24 results in a lower limit on $\frac{\rho_p c_{p,p}}{\rho_f c_{p,f}}$ of 0.38, 0.19 and 0.13. The actual method might be stable for lower values due to conduction and convection in the fluid resulting in an extra contribution towards decreasing the temperature difference.

## 3.5. HEAT TRANSFER INSIDE PARTICLES (FINITE BIOT CASE)

In this section, the numerical methods for two different methods to solve heat transfer for finite Biot numbers will be explained. One of these methods will be based on the immersed boundary method, coupled with a grid inside the particle to solve heat transfer on the particle inside. The other method will be based on the volume of fluid method, in which the heat transfer properties on the fluid grid are dependent on the presence of a particle. This method requires only the heat transfer to be solved on the fluid grid (which for this method combines both the fluid and particle temperatures), and only uses the immersed boundary method for the fluid and particle motion.

### 3.5.1. LAGRANGIAN PARTICLE GRID IBM

In order to simulate finite Biot number particles, it is necessary to solve the heat transfer equations inside the particles. To do this, a grid is created at the surface of the particle (figure 3.4). This grid is fixed to the particle, and also rotates with the particle. The centre of these cells corresponds to the location of the Lagrangian particle points. This grid can be scaled to also create grids on the inside. This results in the particle grid in radial direction only having two neighbors, the grid cell in the next and previous grid shell. The cells have up to 6 neighbors (most have 5) in the same particle shell. All the grid points are numbered, and the connections between these grid cells are saved as a connectivity list, which also contains the distances between the cell centres and the areas of the interfaces.

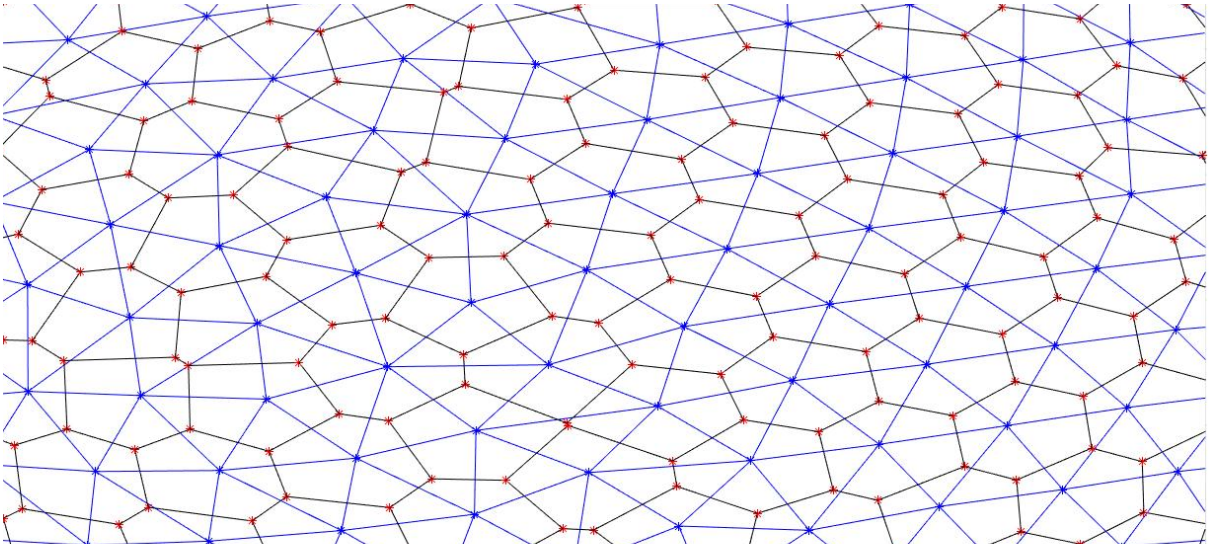

Figure 3.4: Small portion of the grid at the particle surface used to solve heat transfer inside the particle. The blue lines indicate the connections between neighbouring cells, the black lines indicate the cell edges

Since this grid moves and rotates with the particle, the only heat between grid cells is exchanged by conduction. This causes the discretized heat equation to become:

$$T^{r}_{p,i,shell} = T^{r-1}_{p,i,shell} + \Delta t(\alpha_r + \beta_r)\frac{\theta_{shell} + \theta_{rad} + Q_{cell}}{\rho_p c_{p,p} V_{cell}} \tag{3.5.1}$$

The IBM heat source Q only exists for the outside shell. In this above equation, the heat fluxes are determined by:

$$\theta_{shell} = \sum_{conn} A_{self,conn} k_p \frac{T_{conn} - T_{self}}{dist} \tag{3.5.2}$$

$$\theta_r = A_{self,r+1} k_p \frac{T_{r+1} - T_{self}}{dist} + A_{self,r-1} k_p \frac{T_{r-1} - T_{self}}{dist} \tag{3.5.3}$$

In these equations, $dist$ is the distance between the cell centres which varies slightly per grid cell and connection.

The heat source Q is, in contrast to the Biot 0 particle, determined on a per point basis. In order to do this, a correction factor to account for the energy lost or added by the ghost fluid is determined by:

$$corr = 1 - \frac{Q_{ghost}}{Q_{tot}} \tag{3.5.4}$$

The ghost thermal energy flux and the total flux are determined on a per particle level by:

$$Q_{tot} = \sum_{\Omega_p} Q^* V_{Lagr.cell} \tag{3.5.5}$$

$$Q_{ghost} = \sum_{V_p} \rho_f c_{p,f} \frac{T^{r}_{i,j,k} - T^{r-1}_{i,j,k}}{\Delta t(\alpha + \beta)} V_f \varphi_p \tag{3.5.6}$$

The term $Q^*$ is determined by using eq. 3.3.2 by using the temperature of the grid cell instead of the uniform particle temperature.

With this correction, the cell heat flux due to the heat exchange with the fluid can be approximated by:

$$Q_{cell} = Q^* V_{lagr.cell} \cdot corr \tag{3.5.7}$$

This approximation assumes that the change in thermal energy of the ghost fluid is caused by each Lagrangian particle point equally. This is a good approximation if either the particle temperature is high compared to the surrounding flow, or if the particle is in a surrounding fluid with almost no heat gradient. If none of these conditions are fulfilled, the correction applied will result in an extra contribution to the conductivity of the particle, by applying the heat flux not to the cell where the thermal energy should enter, but to a different cell. While this might be a problem when wanting to exactly determine the heat transfer properties of the suspension, this method is accurate enough to determine the overall behaviour of the suspension and the effect large changes in particle thermal conductivity will have on the overall thermal conductivity of the fluid.

Another disadvantages is that, due to the particle shell being influenced by the immersed boundary method being small compared to the complete particle, this method is only stable for larger values of $c_{p,p}$ compared to the Biot 0 particle method. The big advantage of this method, however, is that the particle and fluid grid can be sized differently, and thus allow for large differences in heat transfer properties between the particle and the fluid.

### 3.5.2. VOLUME OF FLUID METHOD

The volume of fluid method solves both the particle and fluid heat transfer on the same grid [1]. In order to do this, the heat conductivity is volume averaged over the cell walls and the thermal capacity of the cell is determined by using the volume average of the thermal capacities of the fluid and particle. This results in the following equations for the heat fluxes:

$$\theta = (\theta_{x,f} + \theta_{x,p} + \theta_{y,f} + \theta_{y,p} + \theta_{z,p} + \theta_{z,f}) \tag{3.5.8}$$

In this equation, the heat fluxes through the cell edges are determined by:

$$\theta_{x,f} = dy\,dz\Big(k_f\varphi_{f,x+}\frac{T_{i+1,j,k}-T_{i,j,k}}{dx} + k_f\varphi_{f,x-}\frac{T_{i-1,j,k}-T_{i,j,k}}{dx} + u_{i-1,j,k}\varphi_{f,x-}\rho_f c_{p,f}\frac{T_{i-1,j,k}+T_{i,j,k}}{2} - u_{i,j,k}\varphi_{f,x+}\rho_f c_{p,f}\frac{T_{i,j,k}+T_{i,j,k}}{2}\Big) \tag{3.5.9}$$

The interface phase indicator $\varphi_{f,x+}$ used in this equation is the amount of fluid present in volume between the cell centers of the i,j,k cell and the i+1,j,k cell. This volume corresponds to the cell used in the staggered grid for determining the $u_{i,j,k}$ velocity (see figure 1.8). Similar, the $\varphi_{f,x-}$ phase indicator corresponds to the fluid present in the $u_{i-1,j,k}$ staggered grid cell. The heat fluxes in y and z direction, and the heat fluxes due to the particles are determined in a similar manner.

When a particle moves, the heat capacity of the cells near the particle boundary changes if the particle heat capacity is not equal to the fluid heat capacity. If the temperature of the cell center was used as measure of the total thermal energy inside the cell, energy would be created when a particle boundary enters the cell due to the increase in cell averaged heat capacity [19]. The inverse, energy being lost, would happen behind particles when the particle leaves a cell. In order to prevent this, and allow this method to be applied for cases in which the particle and fluid heat capacity differ, the cell enthalpy instead of the cell temperature is used for the energy time integration:

$$H^r = H^{r-1} + \alpha_r \Delta t \theta^{r-1} + \beta_r \Delta t \theta^{r-2} \tag{3.5.10}$$

After which this cell enthalpy can be converted to the cell temperature by:

$$T^r = \frac{H^r}{dx\,dy\,dz(\rho_f c_{p,f}\varphi_f + \rho_p c_{p,p}\varphi_p)} \tag{3.5.11}$$

This temperature can then be used to determine the heat fluxes for the next Runge-Kutta time integration step, and to provide outputs using the same methods as used for the single particle temperature methods.

For this method, after having computed the new fluid temperatures, no temperature IBM correction to account for the presence of the particles is needed. It is furthermore not required to keep track of, and update, the temperature of each particle independently.

The advantage of this method is that no IBM correction is required for the temperature field to account for the presence of the particles. When, however, due to a large difference in heat conductivity or heat capacity between the fluid it is required to use smaller grid cells for solving the heat transfer inside the particle, it would be required to use smaller grid cells in the complete domain. The interface in this method is also smeared over a complete cell, which causes this method to smooth out the particle fluid interfaces not only on the fluid side (as is the case for the IBM method), but also on the particle side.

## 3.6. PARALLELIZATION

The parallelization for the heat transfer is implemented in a similar manner as was done in the already existing code. A halo region around the fluid domain of a core is used which contains information about the temperature of the neighbouring cells. This halo gets updated before the fluid heat transfer equation is solved (the velocity halos are updated beforehand, when the flow velocity is solved). For the IBM heat flux, it is required to have a 2 cell thick halo region around the domain for the fluid temperature. This halo needs to be updated each IBM iteration loop before the temperatures are interpolated from the fluid to the Lagrangian particle points. For the isolated particles, it is furthermore required to use a halo for the cell centered phase indicator, since for the isolated particles interpolation, the phase indicator is required for all the cells within 1.5 cells distance from the Lagrangian point. Finally, the IBM heat flux being applied to cells within a halo are sent back towards the core solving these fluid cells and are summed up with the already determined IBM heat flux for these cells. The heat fluxes being applied for each particle are also sent to each particle master, which then sums these heat fluxes (from at most itself and 3 other cores) to determine the new particle temperature and sends this back to all the cores containing Lagrangian points belonging to this particle.

For the Lagrangian grid IBM method, instead of sending one single temperature per particle, each master informs the other relevant cores of the temperature for each point on the outside shell. The master sends, next to these temperatures, also the grid cell number of these points to the other cores. With this grid cell number, the IBM heat fluxes on a per point basis can be send back to the particle master and applied to the correct points. The particle master can then perform the integration of the heat conduction equations for the inside of the particle.

In contrast to all other methods, for the volume of fluid method, it is not required to send any information about the particle temperature or the IBM fluxes to neighbouring cores or particle masters. The only sent and received information for the cores are halos. The halos that require updating are not only the temperature halo and velocities, but also the cell centered and border phase indicators. These all need to be updated before the heat fluxes for the fluid equations are determined.

# 4

# CODE VERIFICATION

It is not possible to compare the results from simulations for moving dense suspensions to actual test results because experimental results for finite sized, neutrally buoyant, well conducting and fully isolated particles are not available. Furthermore, comparing results directly to such complex cases will not indicate where possible errors are made within the code. For these reasons, it is necessary to verify the code by simulating simplified cases. This will be done in this chapter, which not only serves to show the code is working correct and accurate, but also will show the limitations with regards to the heat capacity ratio. In the end of this chapter, the two different methods for the heat transfer inside particles will also be compared, and the most suitable method will be selected for the remainder of the simulations.

## 4.1. FLUID TEMPERATURE SOLVER VERIFICATION

To verify the correct working of the fluid temperature solver, three benchmark cases were simulated (table 4.1), all without any particles in the flow. In the first two simulations, a heat flux boundary condition was used on the top wall, and a constant temperature boundary condition was used on the bottom wall. This, combined with the thermal properties, would cause a converged simulation to have a linear profile ranging from 100 $^{\circ}C$ at the top wall to 0 $^{\circ}C$ at the bottom wall. In order to verify this, both the temperature profile and the velocity profile were plotted. The initial temperature of the fluid was set to be a constant temperature profile to determine if indeed the solution would converge to the correct profile. The results from these simulations are given in figure 4.1. Since these results form a linear temperature profile from 0 $^{\circ}C$ at the bottom wall to 100 $^{\circ}C$ at the top wall for both the no flow case (only conduction) and the Couette flow case (conduction in wall normal and convection in parallel to wall direction), the implementation for the fluid temperature solver seems to be correct.

To further verify the correct working of the fluid temperature solver, a sink term was introduced into the heat flux equations. This heat sink term has a value such that the total energy of the fluid is kept constant, and

Table 4.1: Properties of the particleless flow verification cases

| Property | | 0 velocity | Couette flow | Wall bound flow |
|---|---|---|---|---|
| $L(x,y,z)$ | $[m]$ | 0.5x0.5x0.24 | 0.5x0.5x0.24 | 0.5x0.5x0.24 |
| $N(x,y,z)$ | | 50x50x48 | 50x50x48 | 50x50x48 |
| $cores(x,y,z)$ | | 2x2x1 | 2x2x1 | 1x1x1 |
| $V_{top}$ | $[m/s]$ | 0 | -1 | 1 |
| $V_{bot}$ | $[m/s]$ | 0 | 1 | 1 |
| $Re_{wall}/Re_{bulk}$ | | - | 1000 | 1000 |
| $c_{p,f}$ | $[J/(kgK)]$ | 40 | 40 | 40 |
| $\rho_f$ | $[kg/m^3]$ | 1000 | 1000 | 1000 |
| $k_f$ | $[J/(mKs)]$ | 6.0 | 6.0 | 6.0 |
| $BC_{top}$ | $[^{\circ}C]/[J/(m^2s)]$ | Q=2500 | Q=2500 | Q=500 |
| $BC_{bot}$ | $[^{\circ}C]/[J/(m^2s)]$ | T=0 | T=0 | Q=500 |
| $T_{init,fluid}$ | $[^{\circ}C]$ | 50 | 50 | 0 |

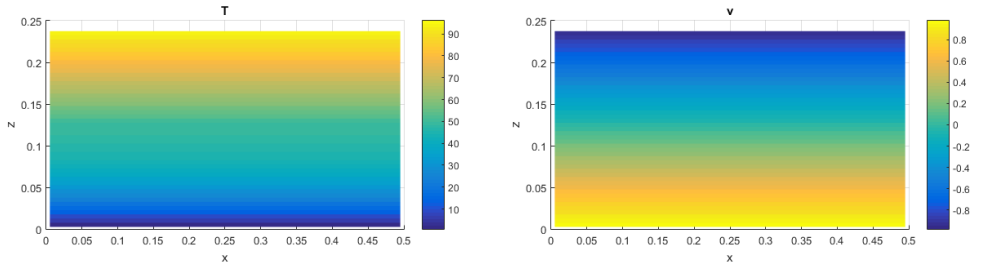


Figure 4.1: Results for the Couette flow verification case, when converged, plotted for a plane perpendicular to the flow direction. The no flow verification case shows the same temperature distribution.

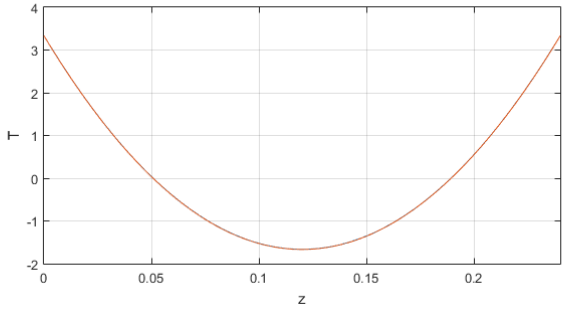


Figure 4.2: Results for the uniform particleless flow case with an evenly spread heat sink for a cut-through line in height direction

thus the heat added by the boundary conditions gets evenly removed throughout the fluid. If the temperature solver is indeed working correctly, this will result in a parabolic temperature profile for the fluid temperature with the following solution:

$$T(z) = \frac{\dot{q}}{2k_f}(z - \frac{1}{2}h)^2 + \frac{\dot{q}}{24k_f}h^2 \qquad 0 \leq z \leq h \tag{4.1.1}$$

Here $\dot{q}$ is the heat sink per volume term, equal to $\dot{q} = -(Q_{top} + Q_{bot})$. The results from this simulation are given in figure 4.2, with a line plot in wall normal direction which can be compared to the expected flow pattern. The root mean square error between the analytic solution and the result from the simulation is equal to:

$$error = \frac{\sqrt{\sum(T_{ana} - T_{sim})^2}}{\sqrt{\sum(T_{ana})^2}} \cdot 100\% = 0.053\,\% \tag{4.1.2}$$

This furthermore shows that the temperature solver for the fluid is correctly working and that all thermal energy is conserved during the simulation.

## 4.2. SINGLE UNIFORM CONSTANT TEMPERATURE SPHERE

To verify the correct working of the zero Biot boundary condition, a single sphere in the middle of a large volume of fluid is simulated (properties of simulation in table 4.2). This is done for both the case of no flow, and with an uniform flow velocity. In order for the uniform flow velocity case to correspond to known analytic solutions, the inflow temperature is set to $0°C$, compared to the circular boundary condition for all other cases. Furthermore, the u,v and w velocities are forced to be equal to 0,1 and 0 respectively at the first 1m in y direction to remove the effect of the circular boundary condition. While this will result in incorrect results in the velocity and temperature profiles close to the circular boundary, it is assumed that the particle is sufficiently far away from the boundary for this effect on the heat conductivity from the particle to the fluid to be negligible. Furthermore, the particle position is fixed to prevent the particle from moving from its centre position.

The results for this are compared to the analytic results from [13] ( $Nu = 2 + (0.4Re_d^{0.5} + 0.06Re_d^{2/3})Pr^{0.4}$ ) and [12] ( $Nu = 2 + 0.6Re_d^{0.5}Pr^{0.33}$ ) for a constant temperature sphere in an infinite fluid.

The results are a Nusselt number of 2.2 for the no flow case and a Nusselt number of 6.7 for the uniform flow velocity case. The temperature distribution for no flow velocity is shown in figure 4.3 and for a uniform flow velocity in figure 4.4. It can be seen that for the case of no flow, the fluid domain is too small to be considered infinite (which is required for the analytic solution). This explains why the Nusselt number of the simulation is slightly higher compared to the analytic solution.

Table 4.2: Properties of the single sphere verification cases

| Property | | 0 velocity | Uniform flow velocity |
|---|---|---|---|
| $L(x,y,z)$ | $[m]$ | 5.0x5.0x5.0 | 5.0x7.5x5.0 |
| $N(x,y,z)$ | | 80x80x80 | 80x120x80 |
| $cores(x,y,z)$ | | 2x2x1 | 2x2x1 |
| $V_{top}$ | $[m/s]$ | 0 | 1 |
| $V_{bot}$ | $[m/s]$ | 0 | 1 |
| $Re_{L_z}$ | | - | 1000 |
| $Re_{d_p}$ | | - | 200 |
| $Pr$ | | 0.25 | 0.25 |
| $c_{p,f}$ | $[J/(kgK)]$ | 40 | 40 |
| $\rho_f$ | $[kg/m^3]$ | 100 | 100 |
| $k_f$ | $[J/(mKs)]$ | 0.5 | 80.0 |
| $BC_{top}$ | $[°C]$ | T=0 | T=0 |
| $BC_{bot}$ | $[°C]$ | T=0 | T=0 |
| $T_{init,fluid}$ | $[°C]$ | 0 | 0 |
| $T_{inflow}$ | $[°C]$ | 0 | 0 |
| $N_p$ | | 1 | 1 |
| $X_p(x,y,z)$ | $[m]$ | 2.5,2.5,2.5 | 2.5,3.75,2.5 |
| $d_p$ | $[m]$ | 1 | 1 |
| $T_{init,p}$ | $[°C]$ | 1 (fixed) | 1 (fixed) |
| $Nu_{expected}$ [13] | | 2.0 | 6.4 |
| $Nu_{expected}$ [12] | | 2.0 | 7.3 |
| $Nu_{simulation}$ | | 2.2 | 6.7 |

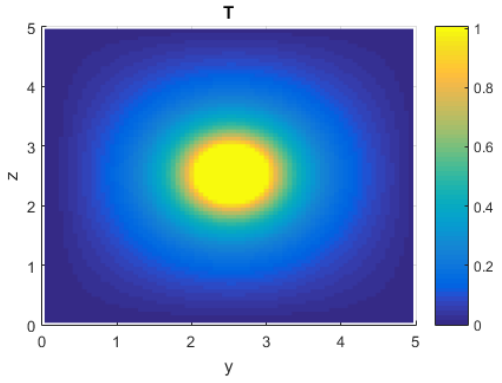


Figure 4.3: Resulting temperature for the single sphere no flow verification case when converged plotted for a plane parallel to the flow direction through the middle of the sphere.

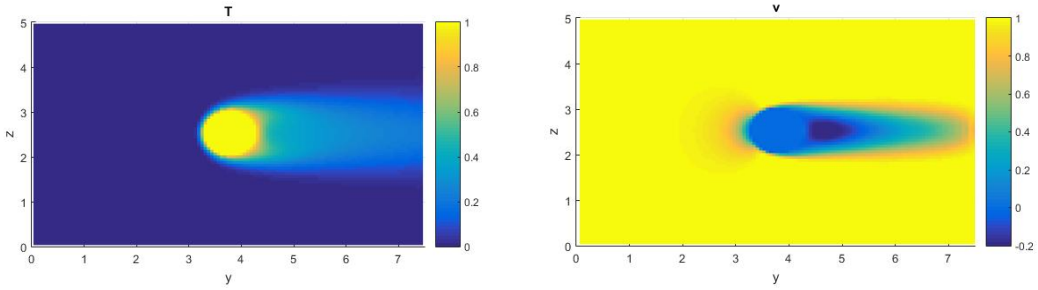


Figure 4.4: Resulting temperature and velocity for the single sphere with uniform flow verification case plotted for a plane parallel to the flow direction through the middle of the sphere.

## 4.3. SINGLE UNIFORM TEMPERATURE COOLING SPHERE

To verify the correct working of the heat equation of the particle, and to check if the heat in the fluid in the same spot as the particle is correctly calculated and extracted from the particle heat transfer, simulations were done for a cooling uniform temperature sphere in an initial cool fluid (see table 4.3). The parameters for the heat capacity were chosen such that, if the code was working correctly, both the particle and the fluid would end up with a temperature of $10°C$. Furthermore, the top and bottom boundary condition were set to be isolated walls, such that all the energy contained in the simulation at the start, should still be present at the end of the simulation. For the first two simulations (zero velocity and Couette flow), the particle was fixed in place, for the third simulation, the particle was free to move. This last simulation is to not only verify the conservation of the thermal energy in the simulation, but also to verify the particle information being correctly transferred between cores when the particle changes position.

The results of these simulations are an end temperature of $9.999°C$ for all the flow cases. This means that for the all cases, the thermal energy lost is at most 0.011% of the total thermal energy present at the start of the simulations. This loss is probably due to the correction for the heat transferred to the ghost fluid. Furthermore, since the moving particle case also shows these results, it can be concluded that the communication of particle data between cores is working correctly.

Table 4.3: Properties of the single cooling sphere verification cases

| Property | | 0 velocity | Couette flow | Poiseuille flow |
|---|---|---|---|---|
| $L(x,y,z)$ | $[m]$ | 3.0x3.0x3.0 | 3.0x3.0x3.0 | 3.0x3.0x3.0 |
| $N(x,y,z)$ | | 48x48x48 | 48x48x48 | 48x48x48 |
| $cores(x,y,z)$ | | 2x2x1 | 2x2x1 | 2x2x1 |
| $V_{top}$ | $[m/s]$ | 0 | -1 | 0 |
| $V_{bot}$ | $[m/s]$ | 0 | 1 | 0 |
| $Re_{wall}$ / $Re_{bulk}$ | | 0 | 1000 | 1000 |
| $c_{p,f}$ | $[J/(kgK)]$ | 100 | 100 | 100 |
| $\rho_f$ | $[kg/m^3]$ | 1000 | 1000 | 1000 |
| $k_f$ | $[J/(mKs)]$ | 1200.0 | 1200.0 | 1200.0 |
| $BC_{top}$ | $[W/m^2]$ | Q=0 | Q=0 | Q=0 |
| $BC_{bot}$ | $[W/m^2]$ | Q=0 | Q=0 | Q=0 |
| $T_{init,fluid}$ | $[°C]$ | 0 | 0 | 0 |
| $N_p$ | | 1 | 1 | 1 |
| $d_p$ | $[m]$ | 1 | 1 | 1 |
| $X_p(x,y,z)$ | $[m]$ | 1.5,1.5,1.5 | 1.5,1.5,1.5 | moving |
| $T_{init,p}$ | $[°C]$ | 100 | 100 | 100 |
| $c_{p,p}$ | $[J/(kgK)]$ | 561.845 | 561.845 | 561.845 |
| $\rho_p$ | $[kg/m^3]$ | 1000 | 1000 | 1000 |
| $T_{end,expected}$ | $[°C]$ | 10.000 | 10.000 | 10.000 |
| $T_{end,simulation}$ | $[°C]$ | 9.9991 | 9.9990 | 9.9989 |

## 4.4. SINGLE ISOLATED SPHERE

In order to verify the working of isolated particles, simulations were done in which instead of giving the particle temperature at the location of the particles, the temperature of the ghost fluid inside the particle is shown. The simulation parameters and initial conditions were used as shown in table 4.4. The results are shown in figure 4.5.

What can be seen from the results, is that the temperature of the fluid in the same position of the particle stays constant. This indicates that no heat is removed or added to the fluid domain by the addition of the isolated particle. what furthermore can be seen for the no flow case, is that the isotherm contour line approach the particle boundary perpendicular to the particle, which further shows the correct working of the isolated particle. The disturbances in the isotherm contour lines very close to the particle are caused by the finite resolution of the data (48 grid cells per direction, and thus data points), which causes the contour lines in the presence of the large temperature difference between the inside and outside of the particle to show small deviations from expected results.

Table 4.4: Properties of the single isolated sphere verification cases

| Property | | 0 velocity | Couette flow | Poiseuille flow |
|---|---|---|---|---|
| $L(x,y,z)$ | $[m]$ | 3.0x3.0x3.0 | 3.0x3.0x3.0 | 3.0x3.0x3.0 |
| $N(x,y,z)$ | | 48x48x48 | 48x48x48 | 48x48x48 |
| $cores(x,y,z)$ | | 1x1x1 | 2x2x1 | 2x2x1 |
| $V_{top}$ | $[m/s]$ | 0 | -1 | 0 |
| $V_{bot}$ | $[m/s]$ | 0 | 1 | 0 |
| $Re_{wall}$ / $Re_{bulk}$ | | 0 | 1000 | 1000 |
| $c_{p,f}$ | $[J/(kgK)]$ | 100 | 100 | 100 |
| $\rho_f$ | $[kg/m^3]$ | 1000 | 1000 | 1000 |
| $k_f$ | $[J/(mKs)]$ | 1200.0 | 1200.0 | 1200.0 |
| $BC_{top}$ | $[^\circ C]$ | T=100 | T=100 | T=100 |
| $BC_{bot}$ | $[^\circ C]$ | T=0 | T=0 | T=0 |
| $T_{init,fluid}$ | $[^\circ C]$ | 0 | 0 | 0 |
| $N_p$ | | 1 | 1 | 1 |
| $d_p$ | $[m]$ | 1 | 1 | 1 |
| $X_p(x,y,z)$ | $[m]$ | 1.5,1.5,1.5 | 1.5,1.5,1.5 | moving |

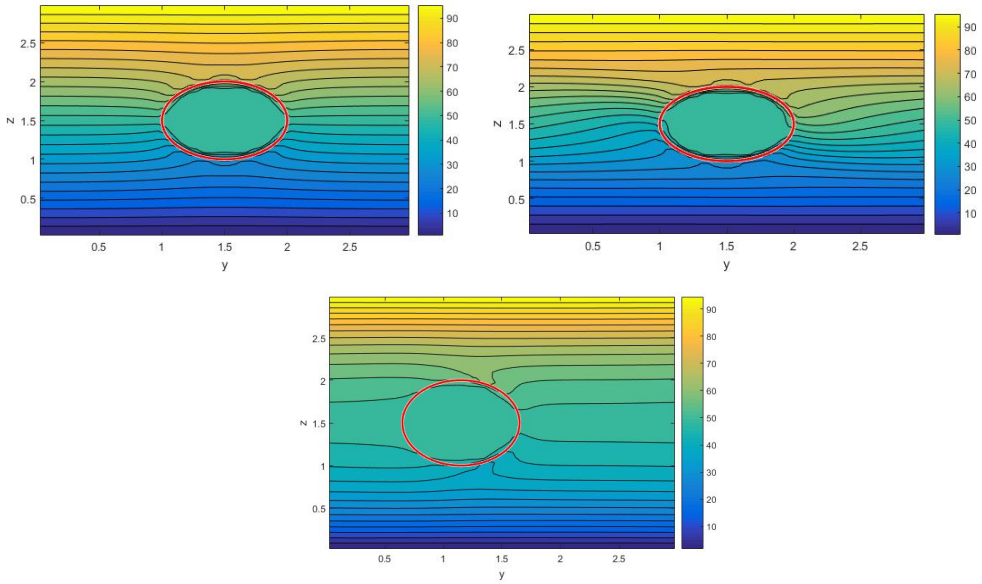


Figure 4.5: Resulting fluid temperature for the single isolated fixed (top left), Couette flow (top right), and moving Poiseuille flow(bottom) sphere verification cases plotted for a plane parallel to the flow direction through the middle of the sphere. The red circle indicates the current particle position.

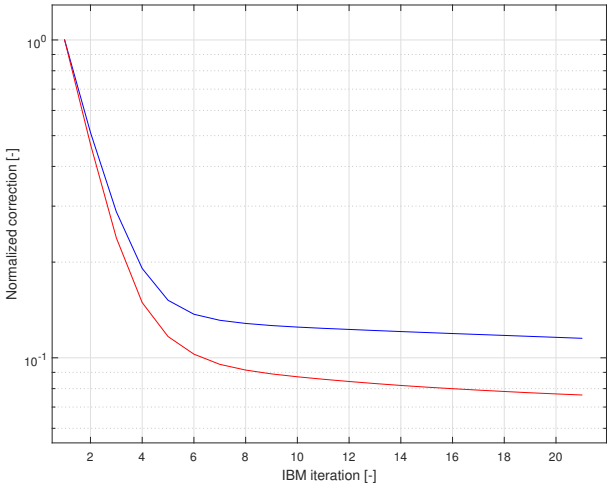


Figure 4.6: Total correction applied per IBM iteration step normalized with the first step for the Biot 0 particle (blue) and Biot infinite particle (red).

## 4.5. REQUIRED AMOUNT OF IBM ITERATIONS

To fulfill the particle boundary condition, it is required to iterate the IBM loop a few times (as described in section 3.3.1).In order to find the minimum required amount of IBM iterations, the non moving, no flow cases from section 4.4 and 4.2 are repeated. With these cases, the IBM heat flux correction is determined by summing up all contributions of the Lagrangian points:

$$\epsilon = \sum_{L} \sum_{i,j,k} |q| \tag{4.5.1}$$

The absolute heat flux is used here since otherwise this would always result in zero for the isolated particle case. These results, normalized by the heat removed in the first iteration, are plotted in figure 4.6. The results given here are for converged simulations, but non converged simulations show almost the same convergence.

What can be seen is that, for both the Biot 0 and Biot infinite particles, the largest IBM corrections are applied in the first 4 iterations. Furthermore, after 6 to 8 iterations, the error does not lower anymore. This is probably due to the way the error is determined, by using the absolute heat flux applied. A further reason the error is not decreasing anymore is the Lagrangian points overlapping and constantly correcting each others correction. From these results, it thus can be concluded that 5 IBM iterations are sufficient.

## 4.6. COLLIDING PARTICLES

To verify that particle collisions do not add or remove any thermal energy from the flow for both the Biot 0 and infinite particles, simulations were done in which 2 particles were initialized such that they should collide in the middle of the fluid domain. As further verification, simulations with a single particle colliding with the wall were also done (see table 4.5). For the Biot 0 particles, it was further checked if the temperatures of the particles changed faster at the moment the particles collided. In order to verify that no energy is added, the fluid boundary conditions are isolated walls.

For the colliding particle cases, what can be seen is that almost no thermal energy is added or removed from the flow. This indicates that the collision between particles doesn't cause any problem. Furthermore, it was seen that for the Biot 0 particle, the temperature of the particles quickly changed when they were close to or colliding with each other.

For the Biot 0 wall collision case, the difference in temperature is of the same order as was the case for the moving Biot 0 sphere. Furthermore, the result from the isolated sphere case shows a very small error. From this, it can be concluded that wall collisions don't cause any problem.

Table 4.5: Properties of the colliding particles verification cases

| Property | | Particle collision | Particle collision | Wall collision | Wall collision |
|---|---|---|---|---|---|
| Biot | | 0 | $\infty$ | 0 | $\infty$ |
| $L(x,y,z)$ | $[m]$ | 3.0x10.0x3.0 | | 3.0x3.0x3.0 | |
| $N(x,y,z)$ | | 48x160x48 | | 48x48x48 | |
| $cores(x,y,z)$ | | 2x2x1 | | 2x2x1 | |
| $V_{top}$ | $[m/s]$ | 0 | | | |
| $V_{bot}$ | $[m/s]$ | 0 | | | |
| $Pr$ | | 1 | | | |
| $c_{p,f}$ | $[J/(kgK)]$ | 100 | | | |
| $\rho_f$ | $[kg/m^3]$ | 1000 | | | |
| $k_f$ | $[J/(mKs)]$ | 1200 | | | |
| $BC_{top}$ | $[W/m^2]$ | Q=0 | | | |
| $BC_{bot}$ | $[W/m^2]$ | Q=0 | | | |
| $T_{init,fluid}$ | $[°C]$ | 50 | | | |
| $N_p$ | | 2 | 2 | 1 | 1 |
| $d_p$ | $[m]$ | 1 | 1 | 1 | 1 |
| $\rho_p$ | $[kg/m^3]$ | 1000 | 1000 | 1000 | 1000 |
| $c_{p,p}$ | $[J/(kgK)]$ | 561.845 | - | 561.845 | - |
| $X_{p1,init}(x,y,z)$ | $[m]$ | 1.5,2.5,1.5 | 1.5,2.5,1.5 | 1.5,1.5,1.5 | 1.5,1.5,1.5 |
| $U_{p1,init}(u,v,w)$ | $[m/s]$ | 0,1,0 | 0,1,0 | 0,0,-0.5 | 0,0,-0.5 |
| $T_{p1,init}$ | $[°C]$ | 0 | - | 100 | - |
| $X_{p2,init}(x,y,z)$ | $[m]$ | 1.5,7.5,1.5 | 1.5,7.5,1.5 | - | - |
| $U_{p2,init}(u,v,w)$ | $[m/s]$ | 0,-1,0 | 0,-1,0 | - | - |
| $T_{p2,init}$ | $[°C]$ | 100 | - | - | - |
| $T_{end,expected}$ | | 50.000 | 50.000 | 55.000 | 50.000 |
| $T_{end,simulation}$ | | 50-4.11·$10^{-5}$ | 50-1.45·$10^{-4}$ | 55.011 | 50-2.55·$10^{-4}$ |

## 4.7. LARGE AMOUNT OF NON-MOVING PARTICLES

To verify the overall correct working of the code, a large number of randomly distributed, non-moving particles are simulated in a non-moving fluid (properties of simulation in table 4.6). These results are compared to results from the Maxwell equation (see also section 1.4.1):

$$\frac{k_0}{k_f} = 1 + \frac{3\phi}{\frac{k_p+2k_f}{k_p-k_f} - \phi} \tag{4.7.1}$$

which is valid for particle volume fractions below 25 % and for randomly distributed non moving particles and non moving liquid. This equation becomes for the limiting cases of Biot 0 and infinite:

$$\frac{k_0}{k_f} = 1 + \frac{3\phi}{1-\phi} \qquad \text{For } Biot = 0 \tag{4.7.2}$$

$$\frac{k_0}{k_f} = 1 - \frac{3\phi}{2+\phi} \qquad \text{For } Biot = \infty \tag{4.7.3}$$

The results from these simulations are an effective conductivity of 180.6 $J/(mKs)$ (+3% off) for Biot 0 particles and an effective conductivity of 72.5 $J/(mKs)$ (-0.2%) for isolated particles. This verifies that the overall working of the code for the heat transfer in finite sized particle suspensions is correct.

Table 4.6: Properties of the large amount of particles verification cases

| Property | | Biot 0 particles | Biot $\infty$ particles |
|---|---|---|---|
| $L(x,y,z)$ | $[m]$ | 5.0x5.0x5.0 | 5.0x5.0x5.0 |
| $N(x,y,z)$ | | 80x80x80 | 80x80x80 |
| $cores(x,y,z)$ | | 2x2x1 | 2x2x1 |
| $c_{p,f}$ | $[J/(kgK)]$ | 100 | 100 |
| $\rho_f$ | $[kg/m^3]$ | 1000 | 1000 |
| $k_f$ | $[J/(mKs)]$ | 100.0 | 100.0 |
| $BC_{top}$ | $[^\circ C]$ | T=100 | T=100 |
| $BC_{bot}$ | $[^\circ C]$ | T=0 | T=0 |
| $T_{init,fluid}$ | $[^\circ C]$ | 50 | 50 |
| $N_p$ | | 48 | 48 |
| $d_p$ | $[m]$ | 1 | 1 |
| $T_{init,p}$ | $[^\circ C]$ | 50 | - |
| $c_{p,p}$ | $[J/(kgK)]$ | 500 | - |
| $\rho_p$ | $[kg/m^3]$ | 1000 | 1000 |
| $\phi$ | [%] | 20.1 | 20.1 |
| $k_{0,expected}$ | $[J/(mKs)]$ | 175.5 | 72.6 |
| $k_{0,simulation}$ | $[J/(mKs)]$ | 180.6 | 72.5 |

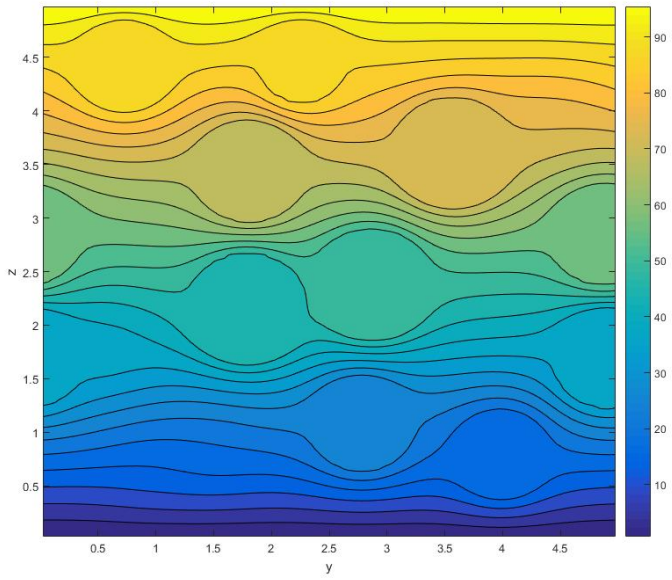


Figure 4.7: Temperature distribution for the non moving large amount of particles case for Biot 0 at a cross section plane in yz direction. The temperatures shown are the fluid and particle temperature.

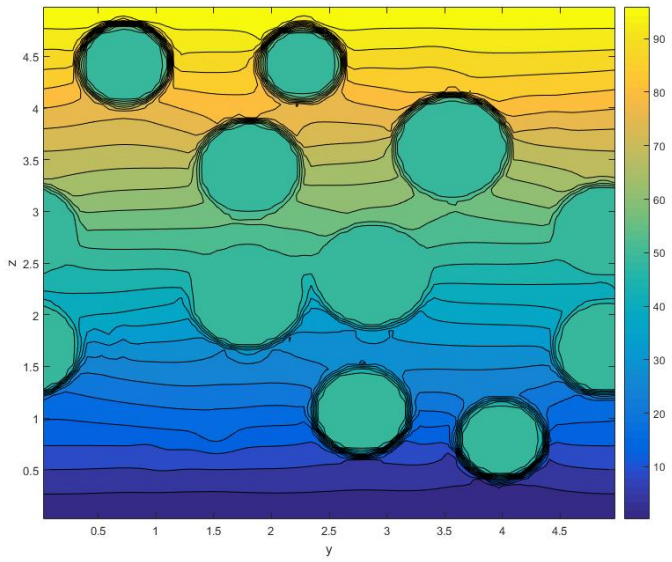


Figure 4.8: Temperature distribution for the non moving large amount of particles case for isolated particles at a cross section plane in yz direction. The temperatures shown are the fluid and ghost fluid temperatures.

## 4.8. STABILITY

The coupling between the particles and the fluid creates a lower limit on the values for $\frac{c_{p,p}}{c_{p,f}}$, as determined in section 3.4. Since this was an upper limit, the verification case for the large amount of non-moving particles is used with different values for the particle heat capacity to determine the actual limit. This resulted in simulations up to a $\frac{c_{p,p}}{c_{p,f}}$ of 0.25 being stable and simulations for a $\frac{c_{p,p}}{c_{p,f}}$ of 0.2 or lower being unstable independent of the time step size used. Since the fluid cell size used ($\frac{dx}{r_p} = \frac{1}{8}$) would result in simulations below 0.38 to be unstable according to section 3.4, this means that the conclusion of section 3.4, that the given equation poses an upper limit and the actual simulations might still be stable for lower values of $\frac{c_{p,p}}{c_{p,f}}$, is correct.

## 4.9. FINITE BIOT NUMBER PARTICLES

In this section, the two implemented methods mentioned in section 3.5 to simulate finite Biot numbers will be verified. It will furthermore be determined which of the two methods is more suitable to solve heat transfer in particle suspensions.

### 4.9.1. LAGRANGIAN PARTICLE GRID IBM

To verify the correct working of the heat transfer inside of the particle and the coupling with the surrounding fluid by means of a correction factor as described in section 3.5.1, verification was done. The first verification was the same as the 0 velocity case from table 4.3 with a particle conductivity equal to the fluid conductivity, which was to verify that the correction factor worked to correct the heat exchange between the particle and fluid on a per point basis for the heat sent to the ghost fluid. The result from this was an end temperature of $0.10033°C$ when the parameters were chosen such that the expected end temperature, should all energy be conserved, was $0.10000\ °C$. This is only a 0.33% error, which although larger than for the Biot 0 verification cases, is still quite small. This thus verifies the correct working of the correction factor to make the particle conserve thermal energy.

However, when verifying the correct heat transfer by simulating a large number of non-moving particles, stability issues due to the small outer shell thickness of the particles arose. This issue has to do with the explicit coupling between the particle shells and the fluid. This is the same instability mechanic as described in section 3.4. These issues could only be resolved by increasing the thermal capacity of the particles to 10 times the thermal capacity of the fluid. This caused further problems since this increase in thermal capacity would mean that there would be strong temperature gradients near the particle surface, and thus would require smaller particle grid cells, thus thinner particle shells, and thus result in the original problem where a further increase in heat capacity is needed to keep this method stable. This makes this method of simulating heat transfer for finite Biot numbers unsuitable for any simulations except when only needing a rough estimate for high thermal capacity particles.

### 4.9.2. VOLUME OF FLUID METHOD

In order to determine if the volume of fluid method is correctly implemented and if this method is suitable to simulate particle suspensions, several simulations were run as verification. The first verification was the same as done for the Lagrangian particle grid IBM (table 4.3, 0 velocity case) with the fluid and particle conductivity equal, checking if the energy in the simulation is conserved. This simulation resulted in an end temperature of $0.094°C$, where $0.1000°C$ was expected. This error of 6% is mostly caused during the initialization, in which the correct temperatures and enthalpies are assigned to each cell. When looking at the overall thermal energy present during the simulation, it is seen that except for the energy loss during the initialization, no further energy is lost.

This simulation was repeated for a moving particle (table 4.3, Poiseuille flow), which produced similar results concerning the thermal energy loss. However, a small increase in temperature at the front, and an decrease in temperature at the back appeared. This is probably caused by the sudden change in the thermal capacity of the cells when the particle enters or leaves the cell. This temperature error appeared to scale with the particle over the fluid thermal capacity. Thus this method is only usable for thermal capacity ratios relatively close to unity (also time step size dependent). This error is only a local, nonphysical, temperature increase/decrease, and does not cause any instabilities as long as the heat capacity ratio is not chosen too big. This is unlike the low thermal capacity for the Lagrangian particle grid IBM method, where the method became unstable for too low heat capacity ratios. This makes this method suitable to investigate the effect of

the thermal and mechanical timescales, but only for a thermal capacity ratio near unity, and only to get an estimate of the actual thermal conductivity.

Finally, to verify the correct working of the heat transfer for both the fluid and the particles, a large number of non-moving particles was simulated (table 4.6) for the thermal conductivity ratios of 0.1, 1 and 10, and these results were compared to equation 1.4.2. The expected effective thermal conductivity ratio is 0.7620, 1 and 1.5327. The results from the simulations are 0.766 (+0.5%), 1 and 1.64 (+6%). Since these errors are of the same order of magnitude as for the Biot 0 and infinite simulations, and are probably also caused by the assumption for the used equation that each particle behaves as if it was in an infinite fluid. These results indicate that the heat transfer is working correctly.

In conclusion, since this method allows for varying the heat capacity ratio around 1, with only small errors for heat capacity ratios of 1/1.1 and 1.1/1, this method is suitable for determining the effect of the thermal and mechanical timescales on the effective thermal conductivity. It should be noted, however, that since the grid cells in the fluid are always the same size as inside the particles, that if a large thermal conductivity ratio is used, the time step size needs to be lowered to keep the simulation stable. This is because it is not possible to increase the particle cell size on its own. Furthermore, simulating with small conductivity ratios might not be very precise, since this would cause large thermal gradients on the inside of the particle. These thermal gradients can't be simulated except when the overall grid cell size is reduced, causing the low thermal conductivity ratio simulations to either be less precise, or require much more grid cells.

# 5

# SIMULATIONS AND RESULTS

## 5.1. SIMULATION PARAMETERS

All simulation were done for Couette channel flow with the constant parameters as shown in table 5.1, unless specifically specified otherwise for several verification cases. It was chosen to have the walls move in y direction. All these parameters are normalized with the particle diameter. The changed parameters are the mechanical particle response time (for all cases) and the thermal particle response time (only for 0 and finite Biot numbers). These are defined as:

$$\tau_m = \frac{d_p^2}{18\nu_f}\frac{\rho_p}{\rho_f} = \frac{d_p}{18V_{wall}}\frac{\rho_p}{\rho_f}\frac{d_p}{L_z}\cdot Re_{wall} \tag{5.1.1}$$

$$\tau_{th} = 3\tau_m Pr \cdot \frac{c_{p,p}}{c_{p,f}} \tag{5.1.2}$$

These timescales are varied by changing the wall Reynolds number defined as $Re_{wall} = \frac{V_{wall}L_z}{\nu_f}$ (by changing the fluid viscosity) in order to change the mechanical timescale, and by changing the heat capacity ratio to determine the changes in thermal timescale.

All simulations were done with a grid cell size of $\frac{dx}{d_p} = 1/16$. This grid size was shown to be sufficiently small for solving the fluid equations [3], and since by using a Prandtl number of 1 the thermal and mechanical length scales are supposed to be approximately equal, should also be sufficient for solving the temperature. For the Biot 0 particles and finite Biot particles the central difference space discretization was used, for the isolated particles the second order upwind space discretization was used (as described in section 3.1).

In section 5.3, the results for simulations with a constant particle concentration of 20% are given, in order to get an understanding of the effect of these timescales. Next, in section 5.4 and 5.5, the effect of the particle conductivity will be determined by simulating isolated particles and heat transfer inside the particles. To verify the validity of these timescales, the results for simulations with a different channel height are given in section 5.6. Finally, in section 5.7, the effect of the particle concentration is analyzed, resulting in an understanding of the heat transfer behaviour for suspensions in laminar Couette flow.s.

Table 5.1: Parameters kept constant during the simulations unless specified otherwise

| Property | | Value | Property | | Value |
|---|---|---|---|---|---|
| $L_x$ | $[m]$ | 8 | $N_x$ | | 128 |
| $L_y$ | $[m]$ | 12 | $N_y$ | | 192 |
| $L_z$ | $[m]$ | 6 | $N_z$ | | 96 |
| $cores_x$ | | 4 | $cores_y$ | | 6 |
| $V_{wall,top}$ | $[m/s]$ | -1 | $V_{wall,bot}$ | $[m/s]$ | 1 |
| $T_{bot}$ | $[^\circ C]$ | 0 | $T_{top}$ | $[^\circ C]$ | 1 |
| $Prandtl$ | | 1 | $\frac{\rho_f}{\rho_p}$ | | 1 |
| $d_p$ | [m] | 1 | | | |

## 5.2. DATA PROCESSING

The results from the simulations are processed in order to give a better insight in both the effect of the changing parameters on the effective heat transfer coefficient, and the underlying mechanisms.

The effective heat transfer coefficient is determined by:

$$q_{top} = \sum_{i,j} k_f \frac{T_{top} - T_{i,j,kmax}}{0.5dz} \cdot \frac{dxdy}{L_x L_y} \tag{5.2.1}$$

$$q_{bot} = \sum_{i,j} k_f \frac{T_{i,j,1} - T_{bot}}{0.5dz} \cdot \frac{dxdy}{L_x L_y} \tag{5.2.2}$$

$$k_{eff,top} = q_{top} \frac{L_z}{T_{top} - T_{bot}} \tag{5.2.3}$$

$$k_{eff,bot} = q_{bot} \frac{L_z}{T_{top} - T_{bot}} \tag{5.2.4}$$

Due to the moving particles, no steady state will be reached. This causes the heat transfer on the top wall and on the bottom wall to be slightly different and thus also causes a difference between the heat transfer coefficient based on the heat transfer of the top and bottom wall. To define a mean effective heat transfer coefficient, the average of both these top and bottom heat transfer coefficients is time averaged, resulting in the average effective heat conductivity.

Furthermore, to better understand the contribution of the particles to the overall heat transfer, both the advection and diffusion terms due to the fluid and the particle are determined at the top border of each cell:

$$\chi_{i,j,k} = \begin{cases} 1, & \text{if } \varphi_{i,j,k} = \varphi_{f,i,j,k+1} = 1. \\ 0, & \text{if } \varphi_{i,j,k} = \varphi_{f,i,j,k+1} = 0. \\ \text{undefined}, & \text{otherwise} \end{cases} \tag{5.2.5}$$

$$q_{adv,f,k} = \frac{dxdy}{L_x L_y} \sum_{i,j} w_{f,i,j,k} \rho_f c_{p,f} \cdot 0.5(T_{f,i,j,k+1} + T_{f,i,j,k})\chi \tag{5.2.6}$$

$$q_{adv,p,k} = \frac{dxdy}{L_x L_y} \sum_{i,j} w_{p,i,j,k} \rho_p c_{p,p} \cdot 0.5(T_{p,i,j,k+1} + T_{p,i,j,k})(1-\chi) \tag{5.2.7}$$

$$q_{dif,f,k} = \frac{dxdy}{L_x L_y} \sum_{i,j} k_f \frac{T_{f,i,j,k+1} - T_{f,i,j,k}}{dz} \chi \tag{5.2.8}$$

The interface phase indicator is used to prevent using a discontinuous temperature to determine the properties at the cell boundary. From these results per time step, the average thermal advection and diffusion contributions of the fluid and the particle can be determined at each horizontal cell layer by averaging over time steps sufficiently far away from the starting time:

$$\overline{q_{adv,f,k}} = \frac{1}{N_t} \sum_{n_t} q_{adv,f,k} \tag{5.2.9}$$

$$\overline{q_{adv,p,k}} = \frac{1}{N_t} \sum_{n_t} q_{adv,p,k} \tag{5.2.10}$$

$$\overline{q_{dif,f,k}} = \frac{1}{N_t} \sum_{n_t} q_{dif,f,k} \tag{5.2.11}$$

$$\overline{q_{dif,p,k}} = k_{eff} \frac{T_{top} - T_{bot}}{L_z} - \left(\overline{q_{adv,f,k}} + \overline{q_{dif,f,k}} + \overline{q_{adv,p,k}}\right) \tag{5.2.12}$$

The definition for the average diffusion in the particle is chosen in this manner since it can't be determined directly from the outputs due to the particles having an uniform temperature (for the 0 and infinite Biot cases) and thus being unable to define the amount of heat transported due to diffusion in the particles. This definition is based on the conservation of energy, that all energy transported at the top, should also be transported in the rest of the fluid. While it is possible to formulate the particle diffusion directly for the intermediate Biot cases, this would only serve to verify the correctness of either this particle diffusion, or the overall wall conductivity. It was thus chosen to use the same method to determine the particle conduction for all cases.

Based on these, the averaged contributions of the fluid and particle conduction and convection towards the overall conductivity can be determined for each height by:

$$\frac{\overline{k_{adv,f,k}}}{k_f} = \overline{q_{adv,f,k}} \frac{L_z}{k_f(T_{top} - T_{bot})} \tag{5.2.13}$$

With these contributions per height the overall contributions towards the effective thermal conductivity can be determined by:

$$\frac{k_{adv,f}}{k_f} = \frac{1}{N_z} \sum_{Nz} \frac{\overline{k_{adv,f,k}}}{k_f} \tag{5.2.14}$$

In a similar manner, the contributions of the fluid conduction, and the particle conduction and convection are determined. These averaged properties give an insight in the effect of the particles towards the overall effective heat conductivity.

Next to these averaged thermal properties, the stresses acting on the moving upper and lower wall are also saved. This is used for the effective viscosity of the suspension to be obtained in a similar manner as the effective conductivity in equation 5.2.1-5.2.4. This allows for determining the ratio between the increase in effective conductivity over effective viscosity, and thus allow determining if the increase in effective thermal conductivity is worthwhile.

The last average quantities determined are the time averaged particle and fluid temperature at each horizontal cell layer, and using a volume of fluid approach the time averaged particle and fluid concentration also at each other horizontal cell layer. These give an indication about the distribution of the temperature and concentration of the particles. This furthermore allows splitting the channel in a centre and wall region, each with their own temperature and velocity gradient. This will eliminate the effect of the presence of the wall for the centre region, and thus allow for determining the effective conductivities for a uniform shear flow case.

### 5.2.1. CONVERGENCE

To determine if enough time was simulated for the results to be converged to statistical averages, the moving average of the effective total conductivity, the effective conductivity per component for the full channel and the effective conductivity per component at 1/4, 1/2 and 3/4 channel height are used. The resulting moving averages for the total thermal conductivity and centre of channel component conductivity for the medium mechanical and thermal timescale simulations can be seen in figure 5.1. The main indication of convergence appeared to be the heat transfer components at single heights. This was checked for all simulations.

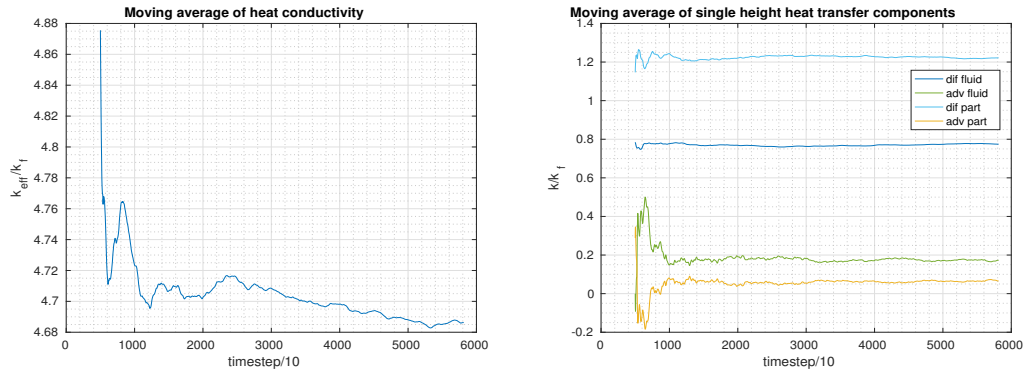


Figure 5.1: Moving averages for the Biot 0 simulations for a thermal timescale of 15s and a mechanical timescale of 5s.

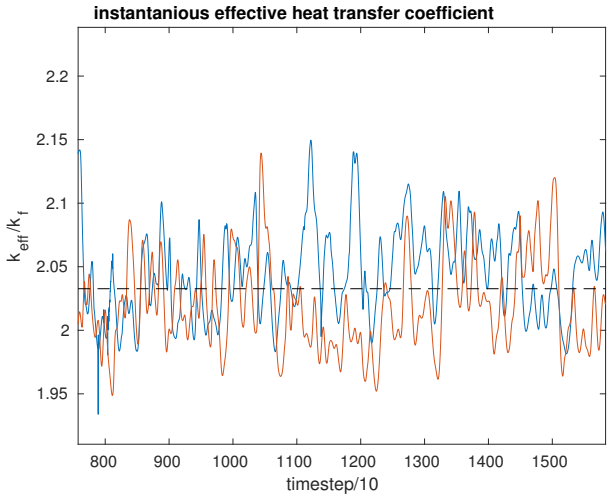


Figure 5.2: Sample of the instantaneous heat transfer coefficient based on the top wall heat flux (red) and the bottom wall heat flux (blue) for thermal timescale of 45s and a mechanical timescale of 15s.

## 5.3. RESULTS FOR ZERO BIOT PARTICLES

The results given in this section are for simulated suspensions with highly conductive particles, causing them to have an uniform temperature. The used thermal and mechanical timescales are shown in table 5.2. These combinations of mechanical and thermal timescales are chosen such that they allow for the comparison of results as function of changes in thermal and mechanical timescale separately.

The simulations were run up to the point that the average conductivity and the average heat transfer properties did not show any oscillations anymore. In most cases, this meant the simulations took 8 hours. The reason these simulations took quite long was that, while the temperature distribution in the fluid quite quickly adapts to the boundary condition, the particle movement influences the heat transfer at the walls. This causes the heat transfer at the wall to be dependent on the particle positions, and thus causes the heat transfer at the wall to show oscillations (see figure 5.2, most notable for higher mechanical particle timescales). Since the overall particle motion is slower than the fluid flow motion adapting to the particles near the wall, low frequency oscillations with higher frequency peaks can be seen. The high frequency peaks that can be seen are due to the flow around near wall particles and due to particle collisions, the larger oscillations are due to more particles at the current time-step being present near one of the walls compared to the other wall.

Another reason for the simulations taking long to be converged enough is that for the heat transfer profiles in height direction, the convection of the particles requires the simulation to be sufficiently long to not show the influence of the individual particles. This effect is strongest for the low mechanical timescale (the particles move only a little in height direction), and high thermal timescale cases (each moving particle immediately causes a large contribution to the overall heat transfer).

Table 5.2: Parameters changed between simulations. For a mechanical timescale of 1.66, the timescale ratio of 27 is also simulated.

| Property | Variable changed | Values of property | | | Values of variable | | |
|---|---|---|---|---|---|---|---|
| $\tau_m$ | $Re_{wall}$ | 1.66 | 5.0 | 15 | 187 | 560 | 1680 |
| $\tau_{th}/\tau_m$ | $c_{p,p}/c_{p,f}$ | 1 | 3 | 9 | 1/3 | 1 | 3 |

### 5.3.1. OVERALL EFFECTIVE CONDUCTIVITY

The effective thermal conductivity resulting from the simulations for the Biot 0 particles is given in figure 5.3. As can be seen in these bar graphs, the thermal timescale only has a significant influence on the contribution of the particle convection to the overall heat transfer. For the cases in which the mechanical particle timescale was changed, it can be seen that the main change in contributions to the total conductivity is the particle convection. It should furthermore be noted that for all the simulated cases, the effective viscosity increases more than the thermal conductivity increases.

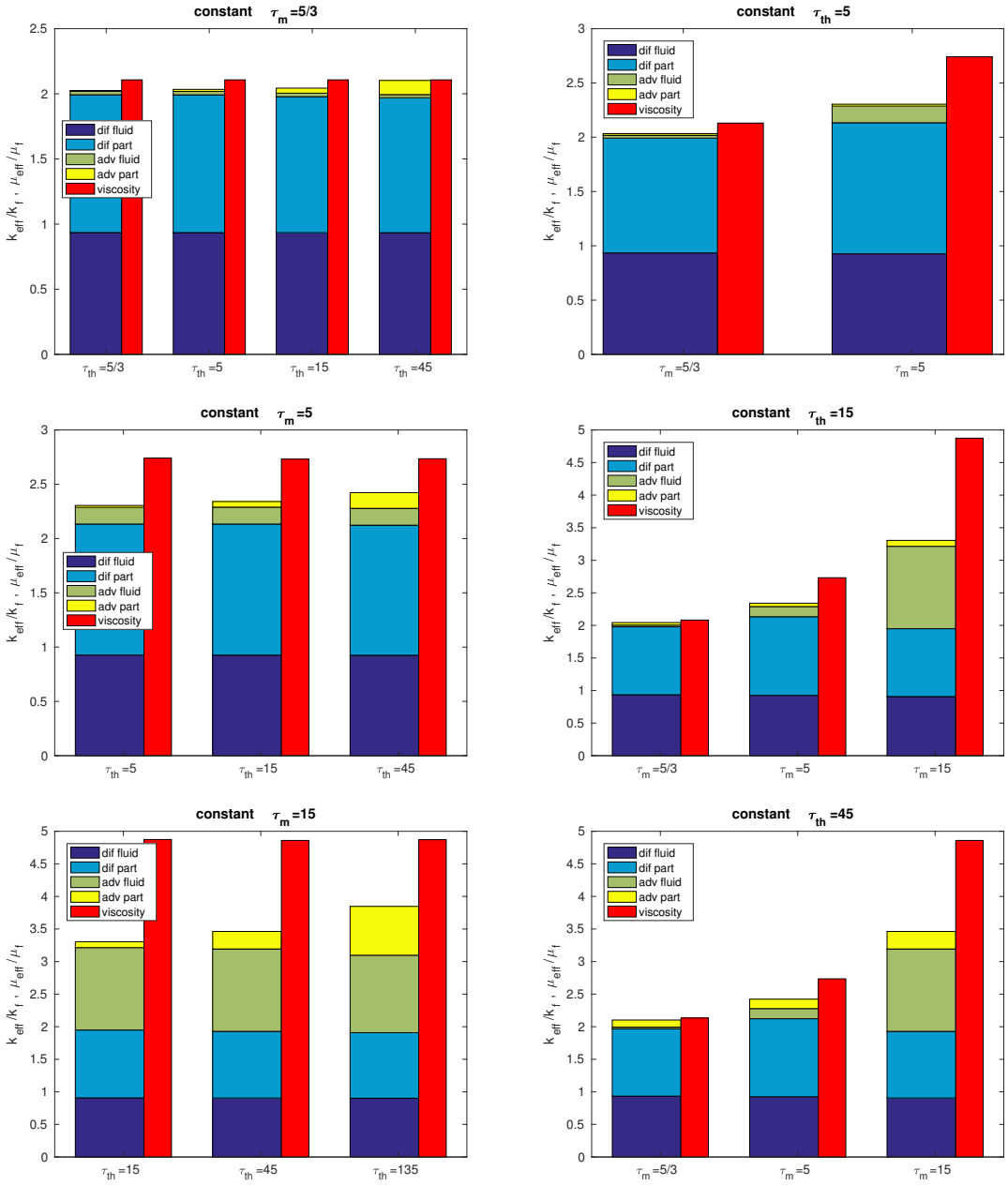


Figure 5.3: Thermal conductivity coefficients for constant mechanical (left) and thermal (right) particle timescales for the zero Biot cases

### 5.3.2. HEAT TRANSFER PROFILES

The contributions towards the overall heat transfer resulting from the fluid and particle conduction and convection are given in figure 5.4 for changes in thermal particle timescale and in figure 5.5 for changes in mechanical particle timescale.

What can be seen is that a change in thermal timescale mainly changes the effect of the particle convection in the centre of the channel, and changes the particle conduction in the region close to the wall. The increase in heat transfer by convection in the centre of the channel can be explained by the increase in thermal timescale causing the particles to require a longer time to adapt to changes in the surrounding fluid temperature. This causes the particles to absorb or release more energy before an thermal equilibrium between the particles and the surrounding fluid is reached. Because of the particles absorbing or releasing more thermal energy, more energy is transported from the hot wall at the top to the bottom wall and this thus causes an increase in effective thermal conductivity.

For an increasing mechanical timescale, the main change in the centre of the channel is the fluid convection. This increase in fluid convection can be explained by an increase in mechanical particle timescale causing the particles to take longer to adapt to flow velocity changes. Once a particle has a velocity in the height direction, it will keep this velocity longer for a higher mechanical response time. This will cause more movement in the fluid for higher mechanical particle timescales, and moving particles are more likely to also

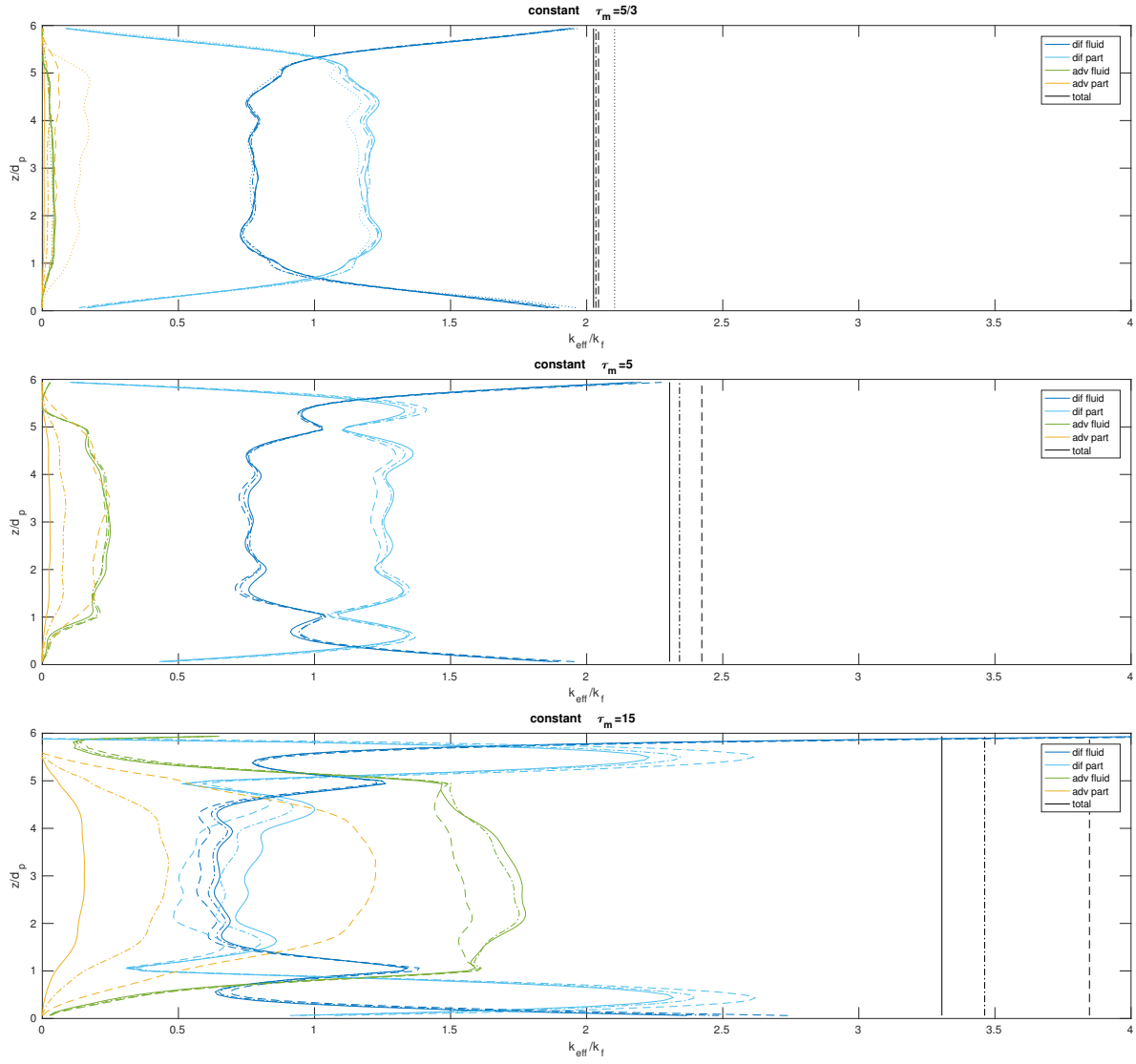


Figure 5.4: Heat transfer profiles with varying thermal particle timescale and constant mechanical particle timescale with the same grouping as used for figure 5.3 (left column).

influence other particles to move in height direction (either due to direct collisions, or due the surrounding flow field). This all causes the fluid to mix in height direction in the region of large particle movements, and thus causes a larger heat transfer due to fluid convection, resulting in a higher thermal conductivity for a higher mechanical particle response time.

The change in heat transfer due to particle conduction can be explained by the infinitely conductive particles trying to match the temperature of the surrounding fluid to the particle temperature. If the surrounding fluid mixes more, the surrounding fluid in the centre of the channel will have a smaller temperature difference. This causes the particles to transfer less thermal energy to keep matching the fluid temperatures around the particle, and thus causes a lower contribution of the particle conduction to the overall heat transfer in the centre of the channel for high particle mechanical timescales.

The increase of thermal conductivity due to particle conduction near the wall is a result from the increase in heat transfer in the centre of the channel. The reason the particles react more to this change in the centre of the channel is because of the high conductivity of the particles. They will conduct all heat instantly in order to match the temperature of all the fluid surrounding the particle. Since in the near wall region, the top or bottom of the particles is very close to the constant temperature walls, this means that all heat that is able to be transferred in the centre will be transferred by the particles towards the walls. This increase is much more visible for changes in mechanical timescale than it is for changes in thermal timescale since not only the

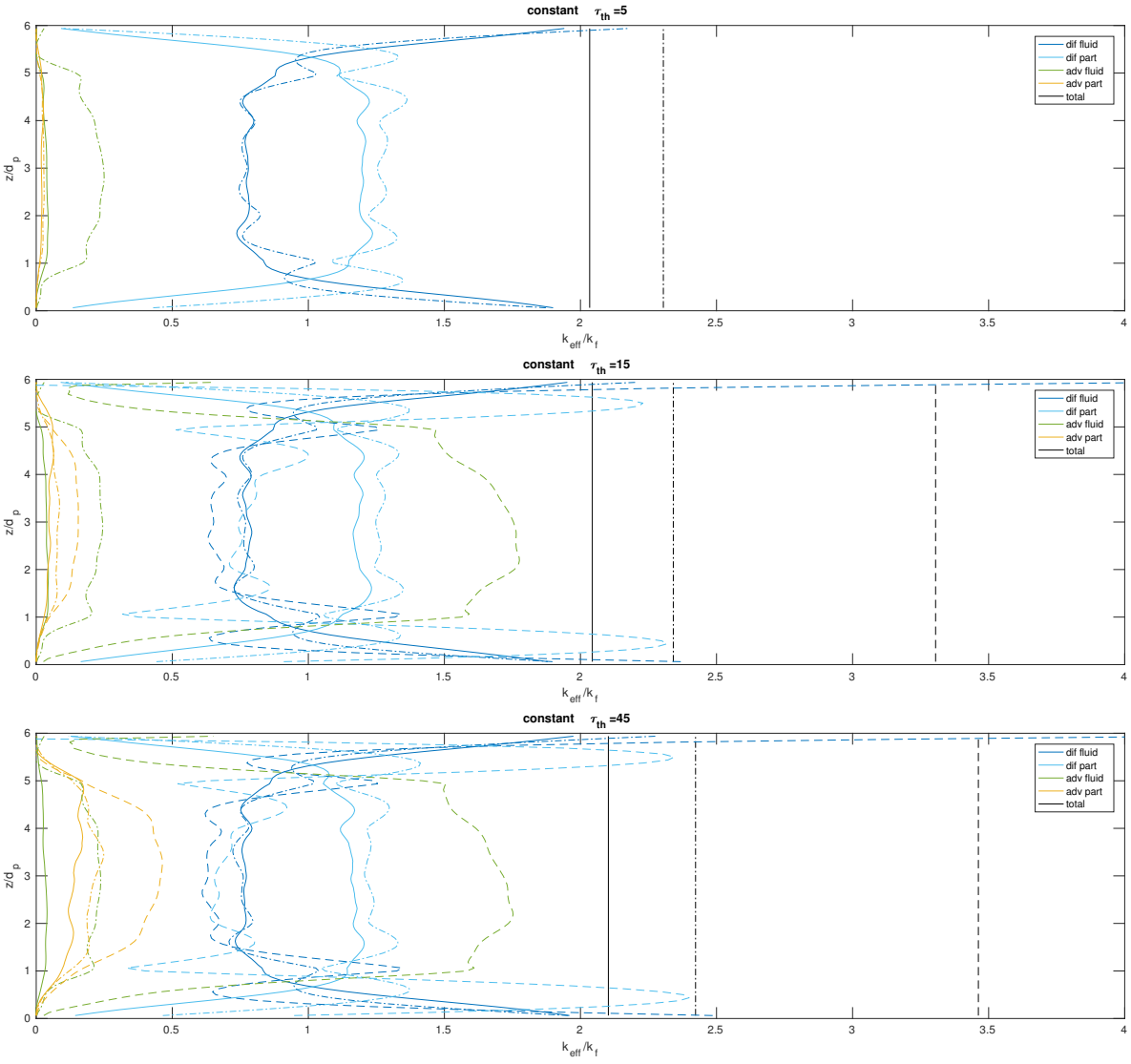


Figure 5.5: Heat transfer profiles with varying mechanical particle timescale and constant thermal particle timescale with the same grouping as used for figure 5.3 (right column).

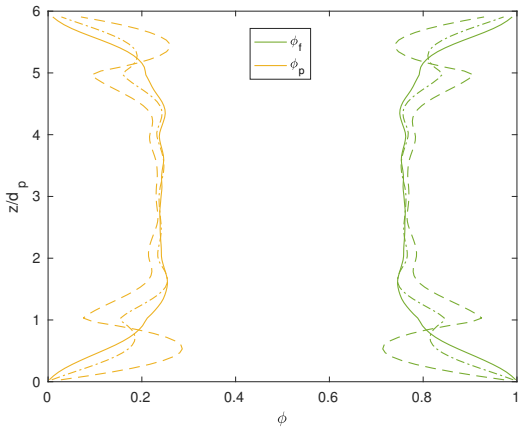


Figure 5.6: Distribution of particles in channel height for mechanical particle timescales of 5/3 (solid line), 5 (dashed line) and 15 (dot-dashed line).

enhanced mixing for larger particle timescales increases the total heat transfer more than the particle convection, but for an increasing mechanical timescale, the particle concentration near the wall also increases, which also results in an increased particle conduction heat transfer. In figure 5.6, this particle concentration distribution can be seen. The increased particle concentration near the wall for higher mechanical timescales is caused by the increase in mechanical timescale giving the particles more vertical movement, which causes the blocking effect of the wall to be more visible and significant.

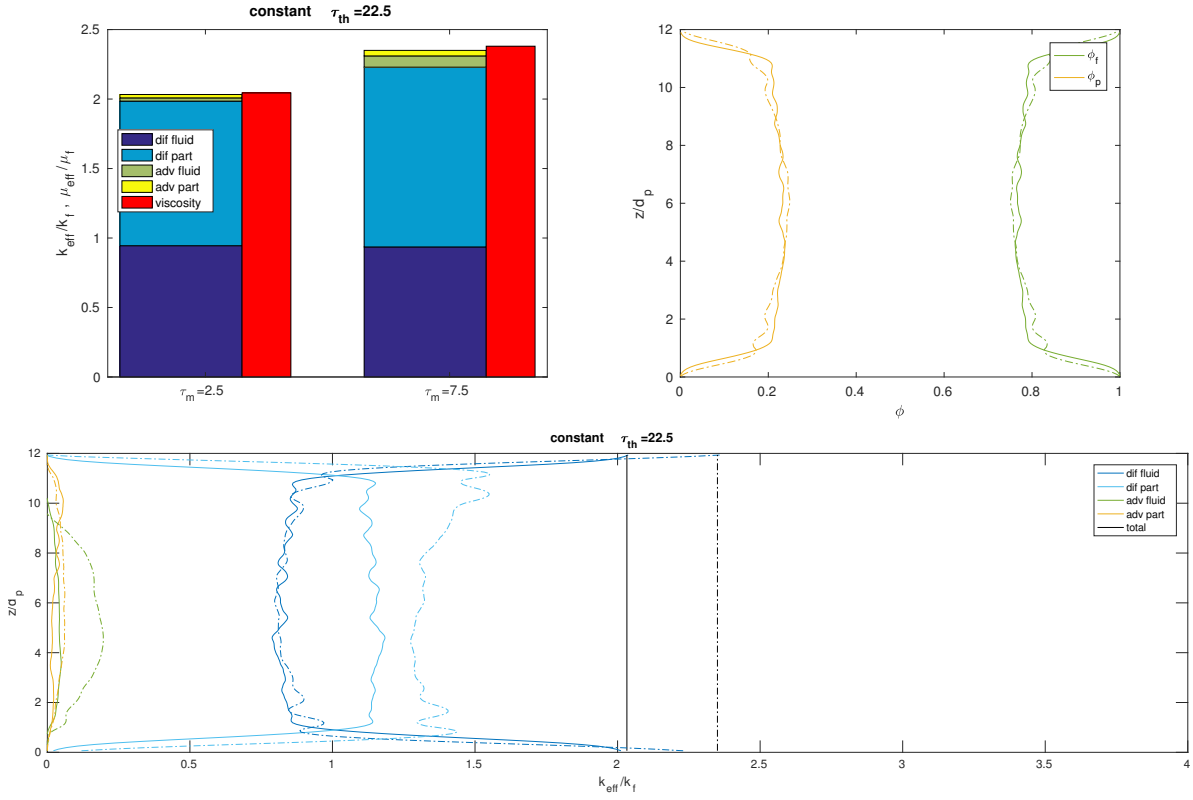


Figure 5.7: Results for the large channel height Biot 0 particle simulations with a constant thermal timescale of 22.5s and a mechanical timescale of 2.5s and 7.5s.

### 5.3.3. LARGER CHANNEL HEIGHT

To verify that the large particle conduction peaks near the walls are indeed the result of the presence of the wall, simulations were done for a channel with a height of 12 particle diameters. These simulations were done for a thermal timescale of 22.5 and mechanical timescales of 2.5 and 7.5. The mechanical, and thus thermal, timescales are chosen differently compared to the smaller channel height cases in order to prevent the Reynolds number getting close to the turbulent flow regime (used Reynolds numbers are 560 and 1680). Furthermore, only 2 different mechanical timescales are simulated, since it appeared from previous results that the lower 2 timescales vary only a small amount, while the difference between the upper 2 timescales is much more notable.

The results are given in figure 5.7. It can be seen that the inner region has an approximate constant heat transfer profile, with the exception of the fluid convection for the large mechanical particle timescale. Furthermore, the particle concentrations also show a more constant profile, with only an increase in concentration showing in the near wall region up to 1 particle diameter away. Finally, it should be noted that the decrease in particle concentration near the walls results in the increase in effective viscosity is closer to the increase in effective thermal conductivity compared to the 6 particle diameter height channel.

From these simulations with a larger channel height it can be concluded that the 6 particle diameter channel is sufficiently large to analyze the influence of the changes in thermal and mechanical particle timescale for both the near wall region and the centre of the channel qualitatively.

### 5.3.4. CENTRE OF CHANNEL HEAT TRANSFER

To further analyze the influence of the thermal and mechanical timescales, the inner heat transfer profile is further analyzed. To be able to do this, the heat transfer contributions are scaled, using that the total heat flux is constant throughout the channel height, based on the total thermal conductivity in the inner channel by means of:

$$\frac{q}{k_f} = \frac{k_{eff,wall}}{k_f} \frac{T_{top} - T_{bot}}{L_z} \tag{5.3.1}$$

$$\frac{k_{eff,inner}}{k_f} = \frac{q}{k_f} \frac{L_{inner}}{T_{innertop} - T_{innerbot}} \tag{5.3.2}$$

With the inner region height ($L_{inner}$) spanning the height from 2 to 4 particle diameters, and the inner top and bottom temperatures being the time averaged mean fluid temperatures at these heights. Next the inner heat transfer contributions are determined by:

$$\frac{k_{adv,f,inner}}{k_f} = \frac{1}{N_{inner}} \sum_{inner} \frac{\overline{k_{adv,f}}}{k_f} \frac{k_{eff,inner}}{k_{eff}} \tag{5.3.3}$$

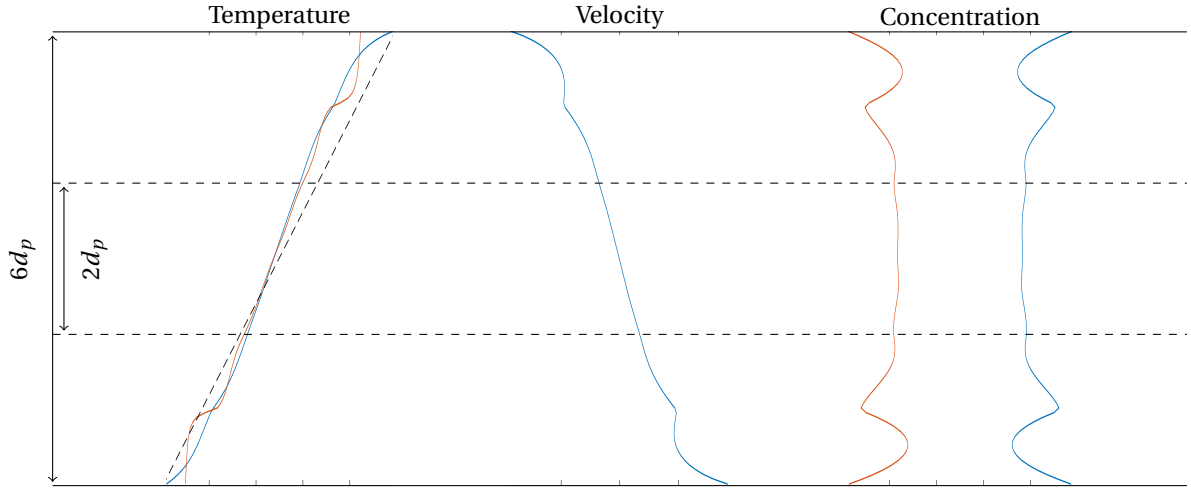


Figure 5.8: Overview of region used for centre of channel analysis with graphs giving the average temperature (left), velocity (centre) and concentration (right) in height direction for particles (orange) and fluid (blue). The results shown here are for the Biot 0, 15s mechanical timescale, 45s thermal timescale results.

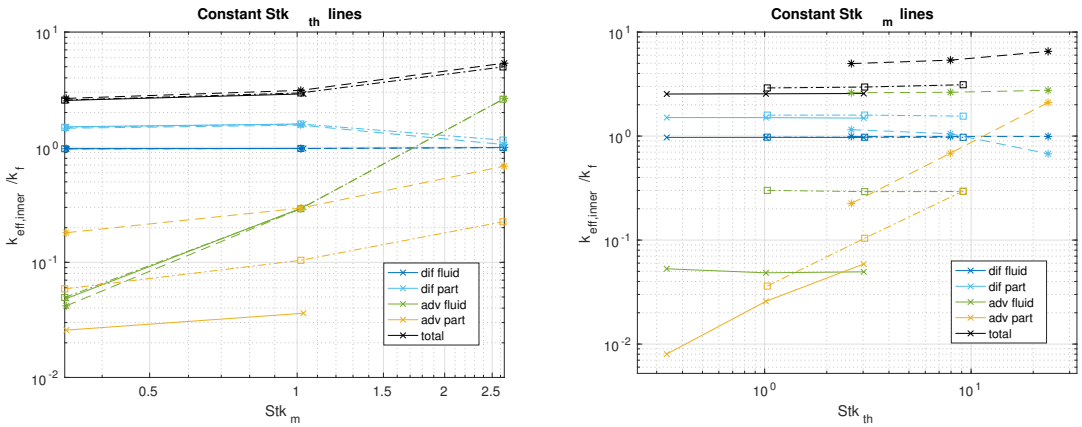


Figure 5.9: Heat transfer in centre of channel for constant thermal timescale (left) and mechanical timescale (right) for low (x markers), medium (square markers) and high (* markers) Stokes numbers.

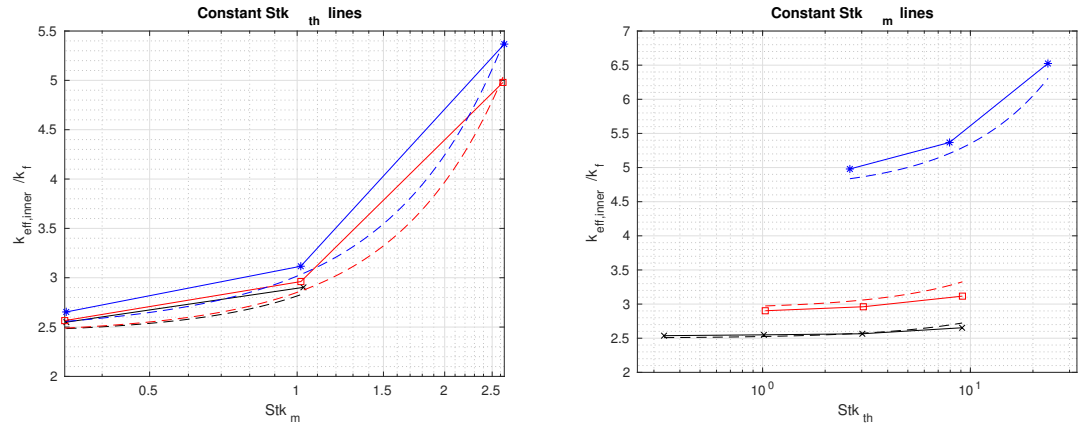


Figure 5.10: Effective heat conductivity in centre of channel for constant thermal timescale (left) and mechanical timescale (right). Solid lines correspond to the simulation results, dotted lines correspond to the results from the curve fit for low (x markers), medium (square markers) and high (* markers) Stokes numbers.

With similar equations for the fluid diffusion heat transfer and the particle heat transfer. The factor $\frac{k_{eff,inner}}{k_{eff}}$ is used to switch from the full channel height and temperature difference to the centre of channel height and temperature difference.

The resulting heat transfer contributions are shown in figure 5.9 in a double logarithmic plot, to account for the large difference in magnitudes. The horizontal axis contains the Stokes number based on the thermal and mechanical timescale:

$$Stk_{th} = \tau_{th} \frac{v_{innertop} - v_{innerbot}}{L_{inner}} \tag{5.3.4}$$

$$Stk_{m} = \tau_{m} \frac{v_{innertop} - v_{innerbot}}{L_{inner}} \tag{5.3.5}$$

In which $v_{innertop}$ and $v_{innerbot}$ are the time averaged mean fluid velocities at the top and bottom of the inner region taken. What can be seen is that for the inner region, increasing the mechanical timescale significantly increases the contribution of the fluid convection to the total heat transfer and slightly increases the contribution of the particle convection. In contrast, increasing the thermal timescale only increases the contribution of the particle convection, while all other contributions stay almost constant.

In order to investigate the influence of the timescales more quantitatively, curves are approximately fitted to these heat transfer contributions. This resulted in the following curve fit for the total heat transfer in the centre of the channel for a centre particle concentration of 24% (and an overall concentration of 20%):

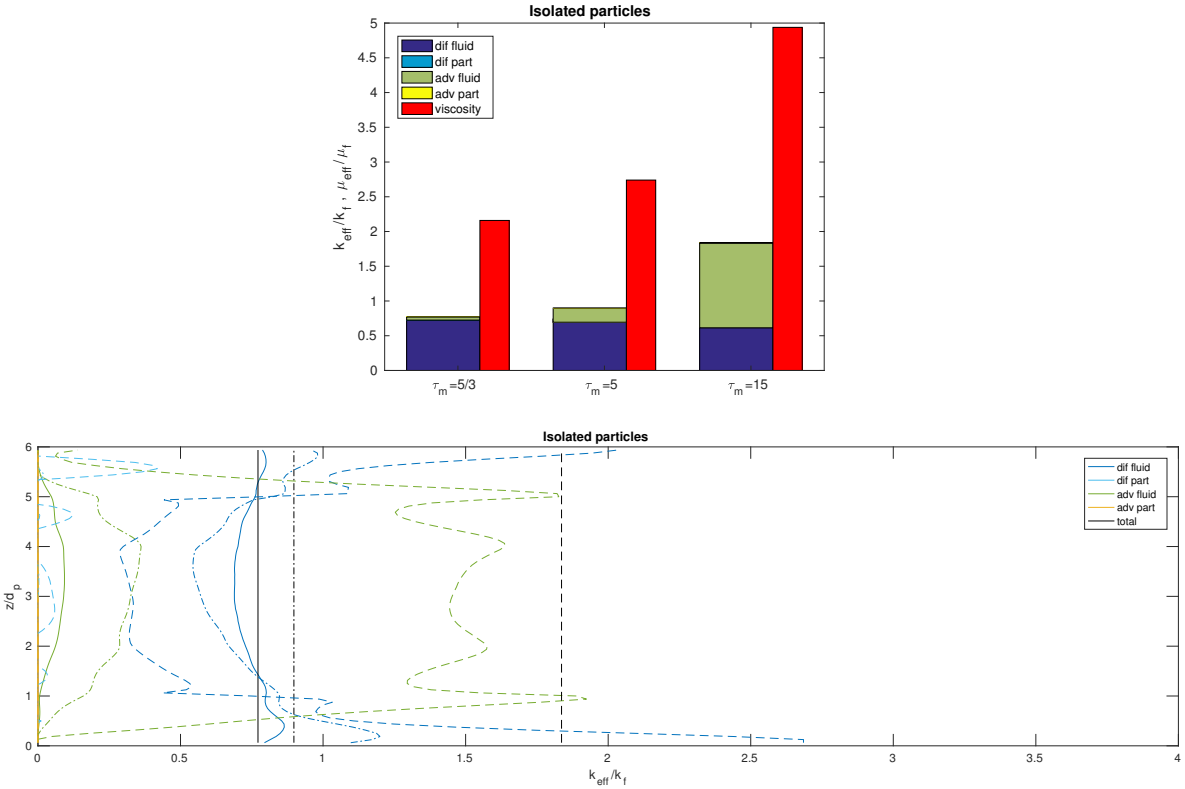


Figure 5.11: Results for the Biot infinite simulations with a varying mechanical timescale of 5/3s, 5s and 15s.

$$\frac{k_{eff,inner}}{k_f} = D_f + D_p + A_f Stk_m^2 + A_p Stk_m^{0.5} Stk_{th} \tag{5.3.6}$$

With the parameters $D_f, D_p, A_f, A_p$ possibly being dependent on the parameters that were kept constant for the simulations (Biot number, Prandtl number, concentration, density ratio). The values for the current parameters are approximately equal to: $D_f = 0.97, D_p = 1.3, A_f = 0.35, A_p = 0.041$. The comparison of this curve fitted equation to the thermal conductivity resulting from the simulations can be seen in figure 5.10.

## 5.4. RESULTS FOR INFINITE BIOT PARTICLES

The same analysis as was done for Biot 0 particles is repeated for the Biot infinite particles. While more calculations are required in order to fulfill the isolated particle boundary condition and for the second order upwind discretization, the particles not absorbing any heat caused the averaged heat transfer profiles to converge faster. This meant that these simulations also took around 8 hours each, while simulating less timesteps. Since the thermal capacity of the isolated particles doesn't play a role in the heat transfer since they don't absorb or release any thermal energy, only changes in mechanical particle timescale were simulated.

### 5.4.1. FULL CHANNEL RESULTS

The results from these simulations are shown in figure 5.11. It can be seen that the only two significant contributions towards the heat transfer are related to the fluid. The small amount of heat transfer due to the particle diffusion visible in the line graph, which should not occur in isolated particles, could be due to two sources. The IBM spreading affecting a small area in stead of releasing the thermal energy in the exact same spot that it entered might results in heat transfer due to particle conduction. Another reason might be that, even though the upwind scheme should be more stable than the central difference scheme, small oscillations in the solution were still observed near the particles. Since the strongest thermal gradients occur near the walls due to enhanced fluid mixing in the middle, this is also where most of these oscillations occurred. It can be seen in the heat transfer profiles that indeed the largest particle diffusion contributions are in the near wall regions.

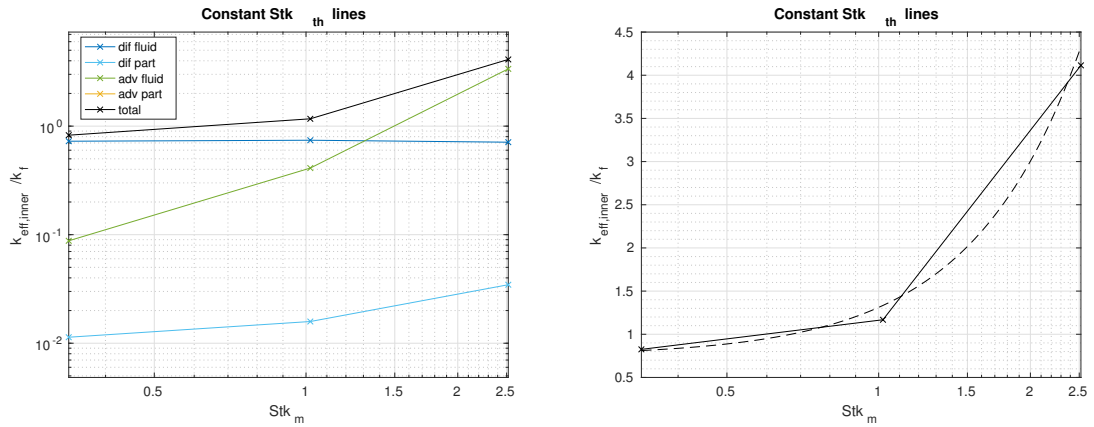


Figure 5.12: Isolated particles suspension heat transfer in centre of channel for constant thermal timescale (left) and effective heat conductivity in centre of channel for constant thermal timescale (right). Solid lines correspond to the simulation results, dotted lines correspond to the results from the curve fit

Furthermore, while the fluid conduction decreases slightly in the centre of the channel, the large increase in fluid conduction near the walls to adapt to the larger amount of heat being conducted makes the total fluid conduction over the whole channel almost constant. The large increase in fluid convection is similar to the increase in fluid convection for the Biot 0 particles. This increase is also caused by the particles taking a longer time to adept to changes in velocity, and thus mixing the fluid in the height direction more when they obtain a vertical velocity, either due to collisions or due to interaction between particles through the fluid.

From this it can be concluded that the same effects occur as for the Biot 0 particles. The fluid and particle conduction stay close to constant, while the increase in mechanical particle timescale greatly enhances the effect of the fluid convection.

### 5.4.2. CENTRE OF CHANNEL RESULTS

Similarly to the Biot 0 simulations, a region of up to 2 particle diameter from the wall shows a different behaviour compared to the core of the flow. In order to analyze the core flow, the same analysis as was done for the Biot 0 particles was repeated (see figure 5.12). In this analysis, the equation resulting from the Biot 0 particles was used and the following coefficients were obtained: $D_f = 0.73, D_p = 0.021, A_f = 0.56, A_p = -$, in which the particle advection coefficient could not be obtained due to the thermal timescale being 0.

It is interesting to note that the curve still shows the same trend as obtained from the Biot 0 simulations. Furthermore, the sum of the diffusion coefficients (0.75 and 2.27) show a clear effect of the particle conductivity. When compared to the non moving particle solution from equation 1.4.2 for a centre concentration of 24% (0.68 and 1.95) it can be seen that, while these are not an exact match, they are strongly correlated. This could indicate that instead of using the fluid and particle conduction as separate terms, these two terms can be combined and based on the non-moving effective conductivity. The main difference between the obtained effective conductive heat transfer and the conductivity resulting from the non moving particle equation could be caused by particles being close to each other and forming layers due to the particle motion. It was seen in the verification for a large amount of non moving particles (section 4.7) that the particle interaction has an influence on the obtained thermal conductivity. For non moving particles, these interactions were just due to the random positioning of the particles, but for moving particles, they tend to collide and organize in layers thus the assumption of an infinite medium around each particle becomes even less valid, which could explain the larger deviation from this equation.

It can also be seen that the fluid advection coefficient for the isolated particles is somewhat close to the fluid advection coefficient for Biot 0 particles. This might indicate that the effect of the particles mixing the fluid and thereby enhancing the heat transfer is only weakly dependent on the conductivity of the particles itself.

## 5.5. RESULTS FOR FINITE BIOT PARTICLES

To verify that the conductive heat transfer is strongly related to the non moving suspension conduction, and to verify that the fluid convection term is indeed independent of the particle conductivity, a few simulations

for finite Biot particles were done. Since the implemented volume of fluid method is most stable for a thermal capacity ratio of 1, the simulations were done at this thermal capacity ratio, and thus the thermal and mechanical timescales are coupled. However, based on the previous results, it should be possible to deduce the independent effects of both the timescales.

The simulations were done for the same mechanical timescale as used before, and a thermal conductivity ratio between the fluid and the particles of 1/3, 1 and 5. These values were chosen to span a wide range between the previous cases, while also spanning a range between the non moving suspension heat conductivity ratios. The Biot numbers corresponding to these heat conductivity ratios are equal to 6, 2 and 2/5, assuming only a small effect of forced convection towards the total heat transfer due to a low velocity difference between the fluid and particles, and thus a Nusselt number of approximately 2.

### 5.5.1. TOTAL CHANNEL RESULTS

The results for the total channel height heat transfer are given in figure 5.13. It can be seen that the most significant change in the thermal conductivity results from the increase in particle diffusion, and a small increase in fluid diffusion. Furthermore, the heat transfer contributions due to the fluid and particle advection stay almost constant for constant timescales.

When looking at the heat transfer profiles in figure 5.14 it can be seen that indeed the fluid and particle convection show a similar behaviour for all cases independent of the thermal particle conductivity. The small differences between the cases can be explained by a change in particle conductivity changing the overall heat distribution around the particles, and thus slightly changing the location at which the thermal energy is available to be convected.

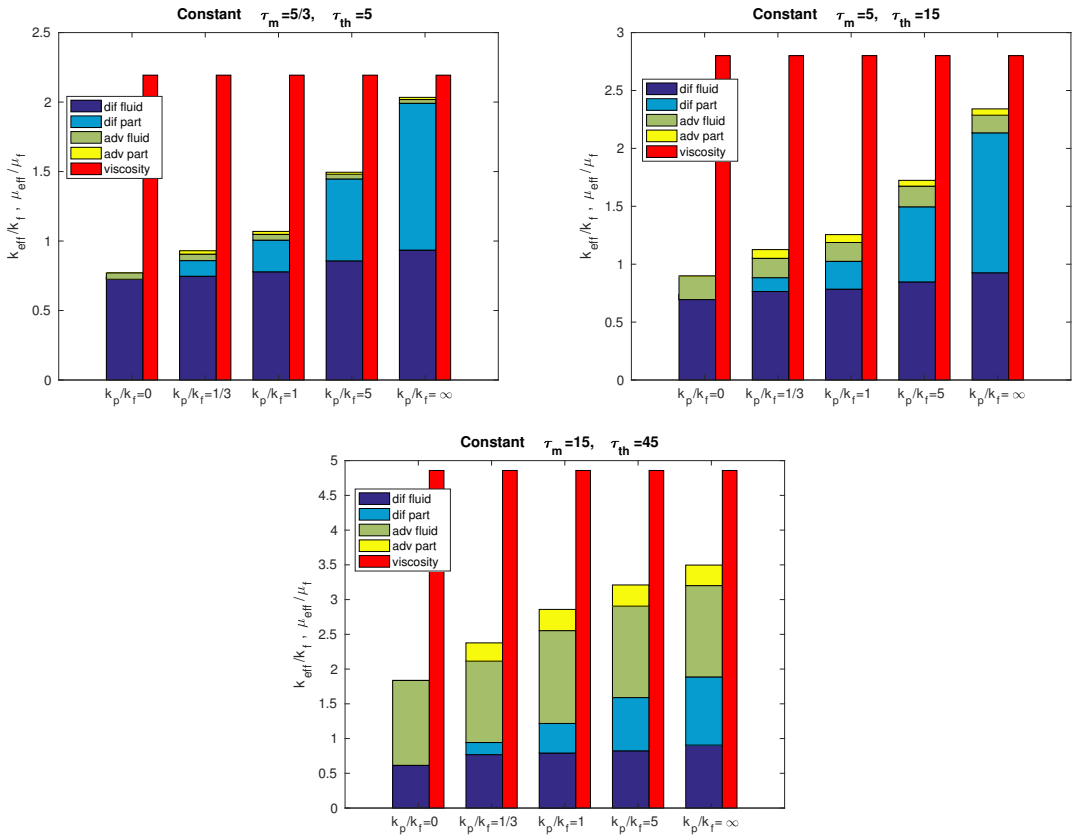


Figure 5.13: Results for a varying particle conductivity for the full channel height. the results for the $k_p/k_f = 0$ particles are from Biot infinite IBM particle simulations, the results for the $k_p/k_f = \infty$ IBM particles from the Biot 0 simulations and the intermediate conductivities are from VOF simulations.

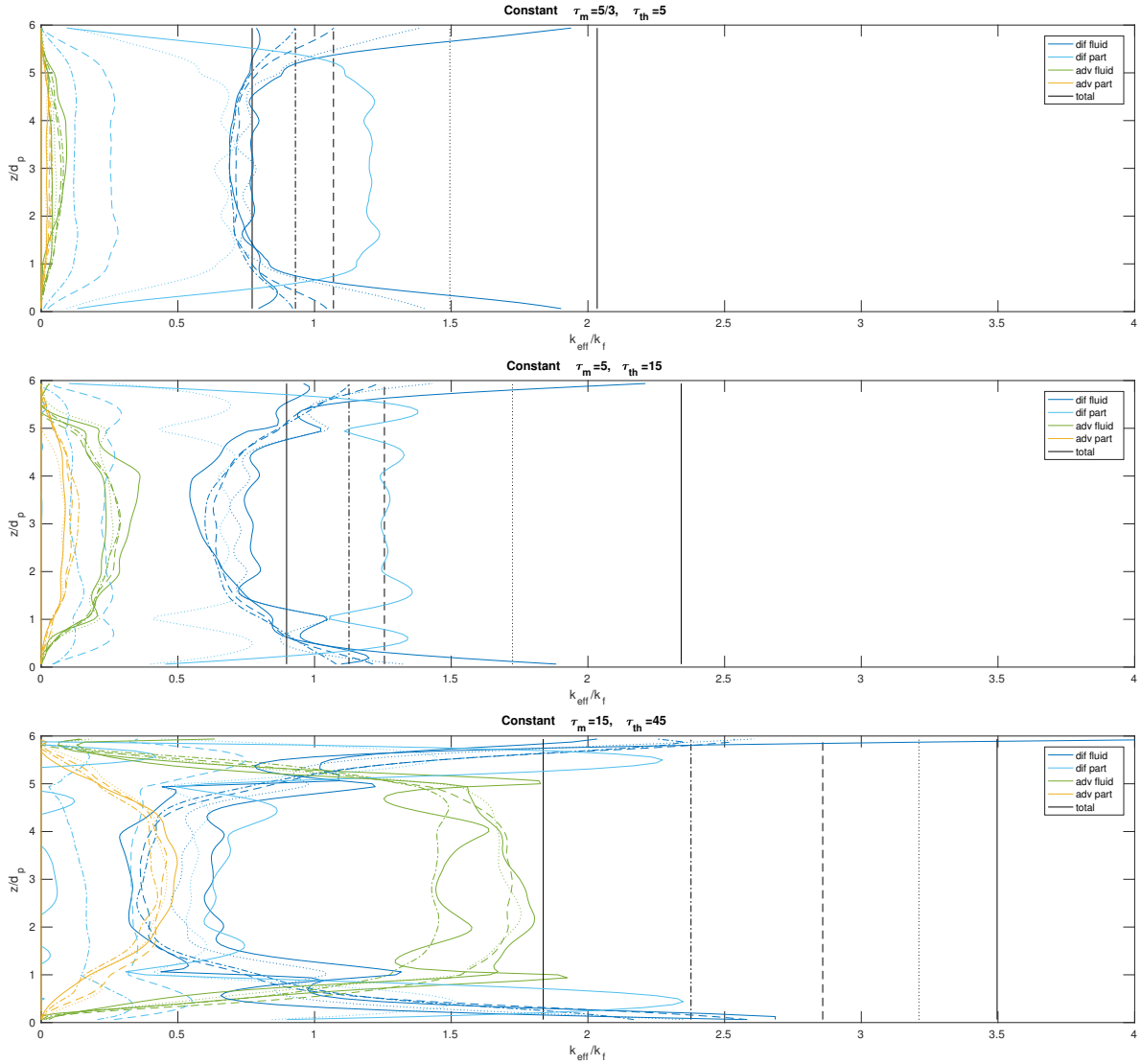


Figure 5.14: Resulting heat transfer profiles for a varying particle conductivity for the full channel height. the results for the $k_p/k_f = 0$ particles are from Biot infinite IBM particle simulations, the results for the $k_p/k_f = \infty$ IBM particles from the Biot 0 simulations and the intermediate conductivities are from VOF simulations.

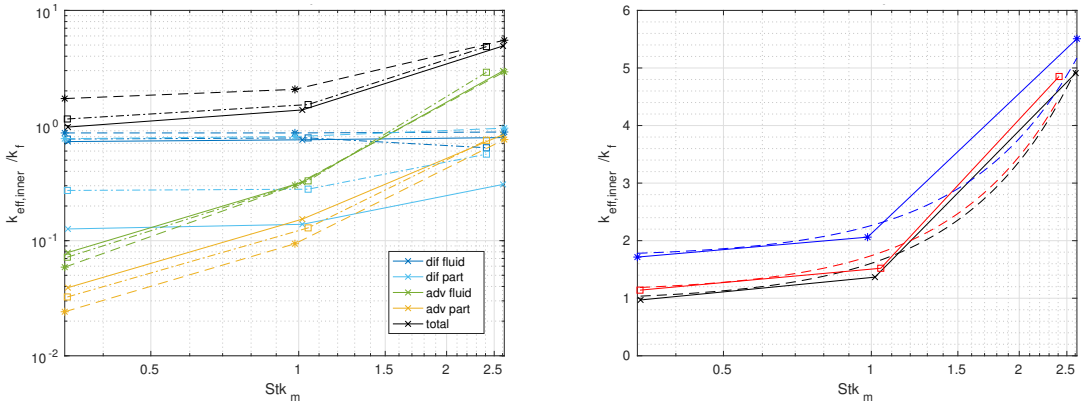


Figure 5.15: Finite Biot particles suspension heat transfer in centre of channel for varying mechanical and thermal timescale at constant particle conductivity(left) and effective heat conductivity in centre of channel for varying thermal and mechanical timescale (right). Solid lines correspond to the simulation results, dotted lines correspond to the results from the curve fit for conductivity ratios of 1/3 (x markers), 1 (square markers) and 5 (* markers) Stokes numbers.

### 5.5.2. CENTRE OF CHANNEL RESULTS

The same centre of channel analysis is also applied to the finite Biot cases. The results can be seen in figure 5.15. What can be seen is that the same curve fit used for the Biot 0 and infinite particles represents the overall behaviour correctly, but shows larger deviations for high mechanical (and thus also thermal) particle timescales.

The coefficients for the curve fit (based on equation 5.3.6) are given in table 5.3. From these coefficients, it seems that there is indeed a strong correlation between the non-moving suspension thermal conductivity and the total diffusion in the centre of the channel. Furthermore, the advection coefficients are only slightly dependent on the thermal conductivity ratio, and thus the particle Biot number. This indicates that for low particle timescales, the thermal conductivity ratio is the most important parameter for increasing the thermal conductivity of the suspension. When the mechanical timescale is increased, however, the effect of the conductivity of the particles itself stays almost constant, while the effect of the fluid convection increases due to the enhanced mixing induced by the particles. This leads to the most significant contribution for higher mechanical particle timescales being the fluid convection. The downside of this increase, however, is that this increase comes together with an increase in effective viscosity, and thus introduces more losses. For increasing the effective conductivity without increasing the effective viscosity, the thermal timescale can be increased. While the effect of this timescale on the total effective conductivity is low compared to the increase in mechanical timescale, it gives a small boost to the overall conductivity, while not having the negative effect of increasing the effective viscosity.

Table 5.3: Parameters resulting from the curve-fit for the finite Biot number particles and the earlier results for Biot 0 and infinite particles. Also includes the effective conductivity for non moving suspensions based on equation 1.4.2 for a centre particle concentration of 24%.

| Parameter | $k_p/k_f$=1/3 | $k_p/k_f$=1 | $k_p/k_f$=5 | $k_p/k_f$=0 | $k_p/k_f$=$\infty$ |
|---|---|---|---|---|---|
| $D_f$ | 0.75 | 0.73 | 0.87 | 0.73 | 0.97 |
| $D_p$ | 0.19 | 0.37 | 0.84 | 0.021 | 1.3 |
| $A_f$ | 0.48 | 0.48 | 0.43 | 0.56 | 0.35 |
| $A_p$ | 0.061 | 0.054 | 0.045 | - | 0.041 |
| $D_f + D_p$ | 0.95 | 1.1 | 1.7 | 0.75 | 2.3 |
| $k_0/k_f$ | 0.80 | 1.0 | 1.5 | 0.68 | 2.0 |

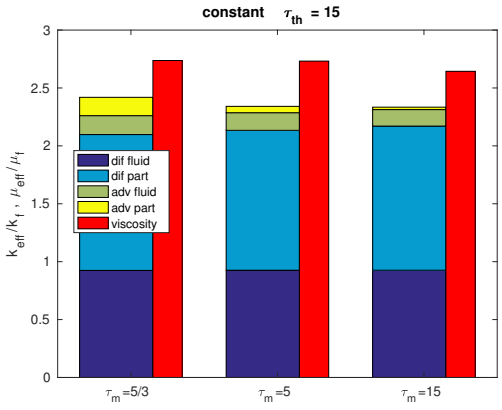


Figure 5.16: Simulation results for the different wall velocity case for a constant thermal timescale and Reynolds number

## 5.6. ACCURACY OF TIMESCALES

While the results given in this chapter show a clear correlation to the mechanical and thermal timescales, these timescales are defined for point particles. To verify that this correlation is indeed dependent on the timescale, and not on the changes in thermal capacity ratio and Reynolds number, 3 simulations were done for a thermal timescale of 15 and a mechanical timescale of 5/3, 3 and 15. The mechanical timescale is varied by changing the wall velocity, while keeping the Reynolds number constant at 560 by also varying the fluid viscosity.

The results from this are given in figure 5.16. It can be seen that a change in mechanical timescale by means of the wall velocity while keeping the thermal timescale constant (by adapting the thermal capacity ratio) only primarily the particle convective heat transfer. Based on previous results, this would indicate no changes in mechanical timescale while the thermal timescale is decreased. When, however, instead of the thermal and mechanical timescale, the thermal and mechanical stokes number are used to specify the particle characteristics, the mechanical Stokes number stays constant, while the thermal Stokes number decreases, due to the changed thermal capacity ratio to keep a constant thermal timescale. This corresponds to earlier results, in which due to the wall velocity not being changed, the relation between the Stokes number and the timescales stayed constant. This thus indicates that the particle timescales are not a good indication of the heat transfer behaviour of the suspension, but rather the thermal and mechanical Stokes number should be used, which for the full channel height can be defined as:

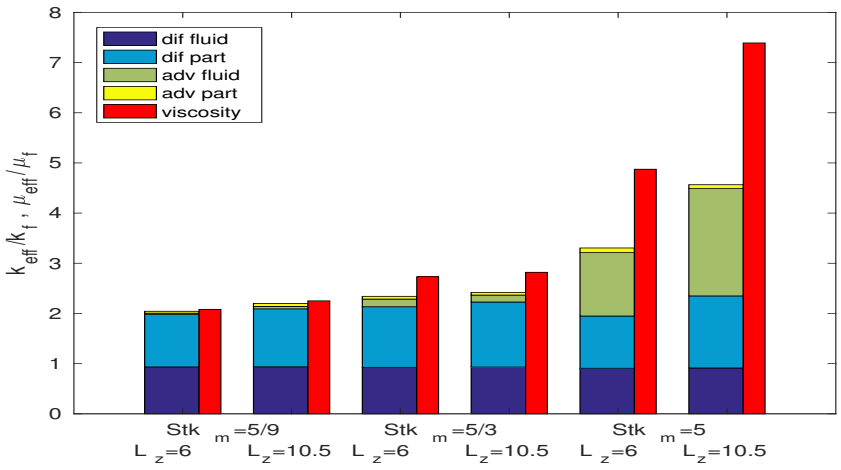


Figure 5.17: Simulation results for the 10.5 and 6 particle diameters high channel at the low, medium and high Stokes numbers.

$$Stk_m = \frac{1}{9}\frac{\rho_p}{\rho_f}\frac{d_p^2}{L_z^2}Re_{wall} \tag{5.6.1}$$

$$Stk_{th} = 3\,Stk_m\,Pr\frac{c_{p,p}}{c_{p,f}} \tag{5.6.2}$$

To further validate these Stokes numbers, simulations were done with a different channel height. The used particle diameter over height ratio was 1/10.5, and the simulated Reynolds numbers were 560, 1680 and 5040, which correspond approximately to the mechanical Stokes number cases for the Biot 0 particles. The thermal Stokes number was kept constant.

What can be seen (figure 5.17) is that the results for Stokes number 5/9 and 5/3 correspond quite well, thus verifying the correctness of the mechanical Stokes number as relevant parameter. The results for the Stokes number of 5, however, differ quite a lot, mainly due to the large difference in fluid convective heat transfer. While this might indicate that the Reynolds number itself is also an important parameter, a more logical explanation for this is that, due to the high Reynolds number used for the large channel, the flow regime of this case is not in the inertial shear thickening flow regime, but in the turbulent flow regime. This indicates that the main role of the Reynolds number for the heat transfer in the inertial shear thickening flow regime is to define the limits of the flow region in which the Stokes number similarity is valid.

## 5.7. EFFECT OF PARTICLE CONCENTRATION

Since it appeared from the previous simulations that for the particle concentration of 20% the effective viscosity always increases more compared to the effective heat conductivity, it is interesting to look at the effect of the particle concentration on both the effective conductivity and the effective viscosity.

### 5.7.1. PARTICLE CONCENTRATION DIFFERENCES

Simulations were done for mechanical Stokes number of 5/9, 5/3 and 5 ($\tau_m$ = 5/3, 5, 15s, $Re_{wall}$ = 187, 560, 1680), a thermal Stokes number of nine times the mechanical stokes number ($\tau_{th}$ = 15, 45, 135s) and Biot 0 particles. The particle concentrations were chosen to be 1%, 5%, 10%, 20% and 30%, thus spanning a range between near to no particles, up to half the maximum possible particle concentration. The Stokes numbers were chosen such to include the whole range of mechanical Stokes numbers previously used while only using the highest thermal Stokes number since the mechanical Stokes number significantly influences the effective heat transfer, while a large thermal Stokes number is needed to see any effect of the particle convection.

The full channel results for the heat transfer are given in figure 5.18 and the particle distributions are given in figure 5.19. What can be seen is that for the low particle concentration cases up to 10% the increase in effective heat conductivity is larger than the increase in effective viscosity. This result was also seen in [1], in which for well conducting particles the increase was bigger up to 10%, and for ill-conducting particles up to 3%.

From the results, however, it is clear that the mechanics of the increase in conductivity between the two Stokes numbers shown is completely different. For the medium Stokes number cases, the increase is mainly due to the conductivity of the fluid and particles itself, with a slight addition of fluid and particle convection for denser suspensions. In contrast, the main increase in thermal conductivity for the high Stokes number cases is due to the fluid convection. Even for the 1% suspension, the effective heat conductivity is significantly increased. This increase can be attributed to the very small amount of particles inducing mixing as soon as they collide and start moving in height direction. Since the particles have enough inertia to significantly influence the flow, the fluid starts to behave turbulent-like. This also explains the large difference in effective viscosity between the two Stokes number cases. For medium mechanical Stokes number the flow is laminar with a near to constant velocity gradient, while for high Stokes number, the velocity gradient near the wall is significantly larger and thus the effective viscosity felt by the wall is significantly larger.

For the high Stokes numbers cases, it can also be seen that the fluid convective heat transfer decreases with increasing concentration. This is probably both because of a decrease in volume of the fluid due to the increased particle concentration, and due to the larger amount of particles limiting the movement of the fluid by them keeping their own direction and velocity due to having a relative large amount of inertia. This decrease in fluid convection, while the total conduction increases because of the increase in concentration, causes the maximum effective conductivity to not appear for the densest suspension but for the 5% and 10% suspensions. This indicates that even when particles are added to maximize the thermal conductivity, while

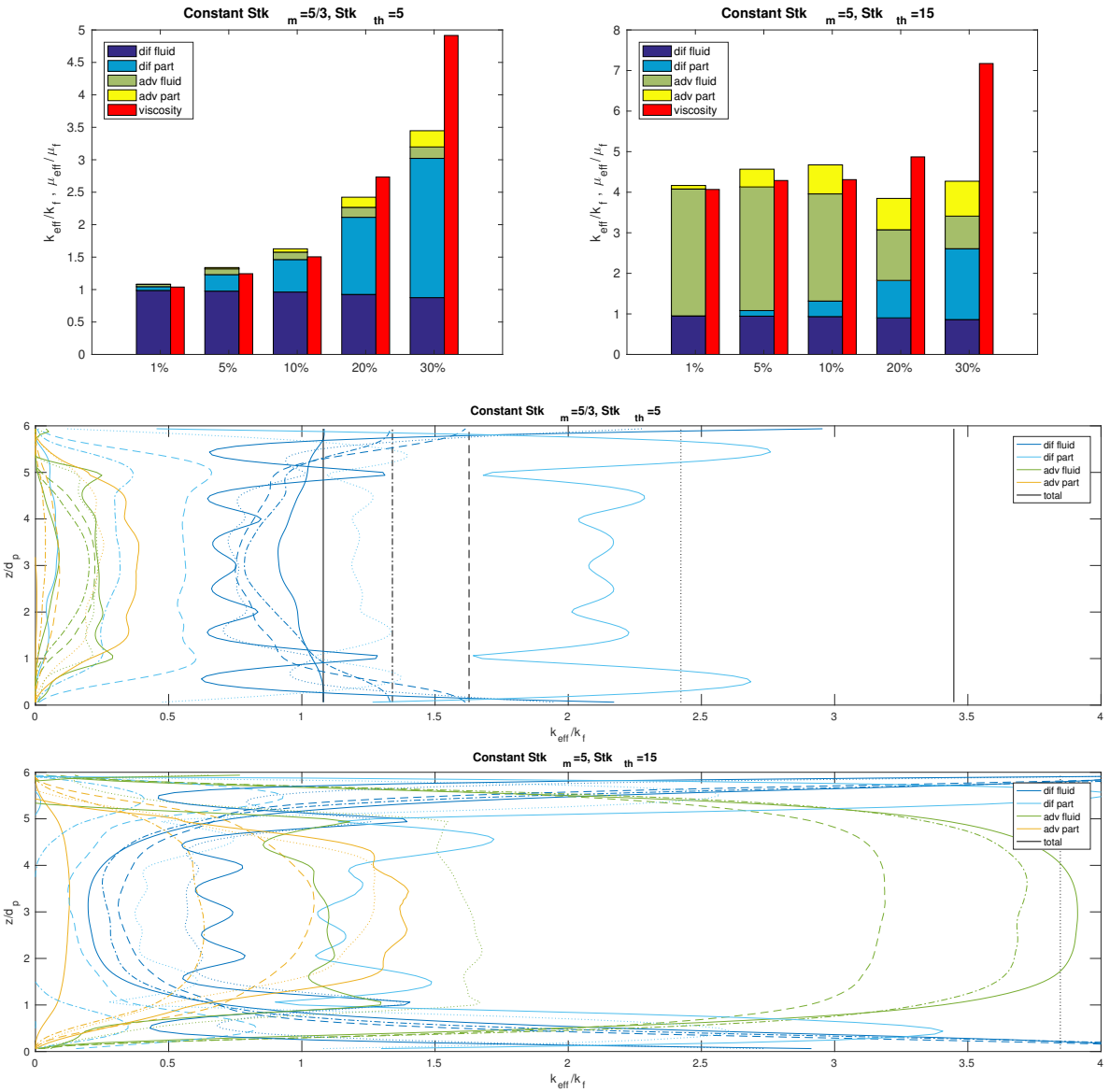


Figure 5.18: Results for the varying particle concentration cases based on the full channel results. Results for the low Stokes number cases not shown, these were similar to the medium (left) Stokes cases.

the effective viscosity is not important, a denser suspension doesn't always result in an increase in effective conductivity.

When trying to apply the same analysis for the centre of the channel heat transfer, it appeared that for the low particle concentration cases the mechanical Stokes number decreased due to the mixing caused in the centre of the fluid by the high inertial particles. This caused the centre of the channel to have a very low velocity gradient, while the wall velocity gradient increased. This decrease in velocity gradient caused the mechanical Stokes number to decrease between the medium and high full channel mechanical Stokes number.

Because this resulted in a decrease of the heat transfer components for an increased centre of channel Stokes number, it was not possible to analyze the centre of flow heat transfer by using exponential functions in the same manner as was done for the previous, 20% suspension, cases. This indicates that the heat transfer behaves completely different for laminar and turbulent flows for low particle concentrations. Since these different regimes do not exist for high particle concentrations, since the flow regime is always in the inertial shear thickening regime [10], it is possible to do this analysis for higher mechanical Stokes numbers for high particle concentrations.

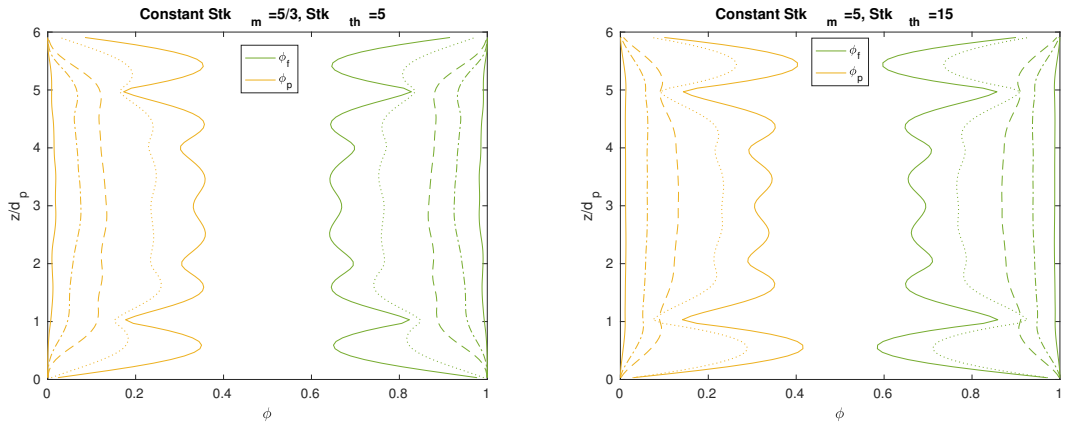


Figure 5.19: Particle concentration distribution for varying suspension densities.

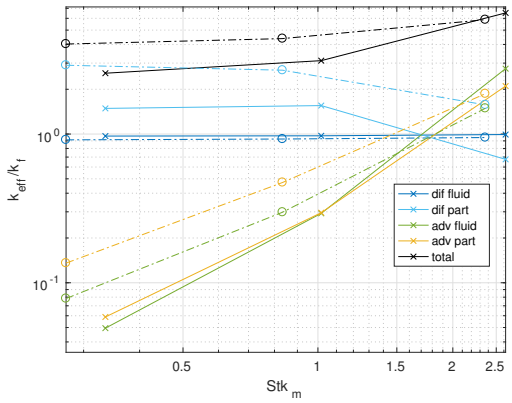


Figure 5.20: Heat transfer contributions towards the overall effective conductivity for the 20% (solid line) and 30% (dashed line) particle concentration cases.

When looking at the heat transfer contributions for the denser suspensions in figure 5.20, it can be seen that the lines for the fluid and particle advection are not parallel to each other. This thus indicates that changes in particle concentration also result in changes in the behaviour of the heat transfer, and thus the exponents of equation 5.3.6 also change. This made it not possible to apply the previously used curve-fit to analyze the behaviour of different concentrations suspensions quantitatively.

### 5.7.2. LOW CONCENTRATION LAMINAR SCALING

To investigate the effect of the particles in the fully laminar, low concentration regime, more simulations were done for particle concentrations of 1, 5 and 10 %, with Reynolds numbers of 187, 373, 560, 747 and 1120, which correspond to mechanical Stokes numbers varying from 0.83 to 2.1. The thermal capacity ratio is taken to be 1 and 3, corresponding to a thermal stokes number of 3 and 9 times the mechanical stokes number. The simulations were done with Biot 0 particles, and the other parameters are as defined in table 5.1.

From these cases, the simulations which do not show any signs of transition towards a turbulent flow structure are selected. A clear example of the difference between the laminar and turbulent flow heat transfer can be seen in figure 5.21. The parameters used for this case resulted in a flow in the region of transition between laminar and turbulent flow. This resulted in the instantaneous heat transfer displaying peaks when the flow temporarily behaved turbulent-like, and low heat transfer when the flow behaved laminar-like.

The heat transfer contributions for both the full channel height as the core of the channel can be seen in figure 5.22 and the overall thermal conductivity can be seen in figure 5.23. What can be seen is that the conduction and the fluid convection are the most significant and the particle convection provides a somewhat relevant contribution for the 10%, high thermal Stokes number case.

The same method as was used for the quantitative analysis of the 20% concentration cases was used to

analyze these results. This resulted in an equation predicting the behaviour of the effective conductivity as function of the mechanical and thermal Stokes numbers, and the particle concentration for the complete channel height:

$$\frac{k_{eff,full}}{k_f} = \frac{k_0}{k_f} + A_f Stk_m^{1.9+5\phi}\phi(1-\phi) + A_p Stk_m^{0.4} Stk_{th}^{0.5}\phi^{1.5} \tag{5.7.1}$$

For the core channel, in which a close to constant temperature and velocity gradient exist, the equation found is:

$$\frac{k_{eff,inner}}{k_f} = \frac{k_0}{k_f} + A_f Stk_m^{1.7+5\phi}\phi(1-\phi) + A_p Stk_m^{0.7} Stk_{th}^{1.25}\phi^{1.5} \tag{5.7.2}$$

The resulting predictions, based on these equations can be seen in figure 5.23. The used constants are $A_f = 1.0, A_p = 0.37$ for the full channel and $A_f = 3.0, A_p = 0.24$ for the channel core. The constant $\frac{k_0}{k_f}$ is the non-moving thermal conductivity due to conduction for the average location of the particles, which is independent of the mechanical and thermal Stokes number.

It is interesting to note that, even though the scaling of the thermal conductivity depends differently on the thermal and mechanical Stokes number for the complete channel and core channel, the influence of the concentration is similar in both equations. For the fluid convective heat transfer, two separate effects exist: an increase in mixing due to the increased amount of particles, and a decrease in fluid advective heat transfer due to a decrease in fluid for increased particle concentration. In contrast, the particle heat convection only depends on the concentration increase, since this will both increase the available amount of particles to move thermal energy, and increase the amount of collisions between particles, which cause more vertical particle movement.

When comparing these results to the results obtained for the 20% concentration cases, it appears that the prediction given here for variable concentrations not correspond to the 20% concentration prediction. This is probably due to this prediction being based on dilute suspensions, in which particle collisions (and their corresponding defining collision parameters) do not play a significant role for dilute suspensions. In contrast, for the 20 % and 30 % suspension cases, the particle collisions become much more important. This different behaviour in thermal conductivity scaling corresponds to the different flow regimes mentioned in section 1.2, thus indicating that different thermal scaling behaviour appears for the different suspension flow regimes.

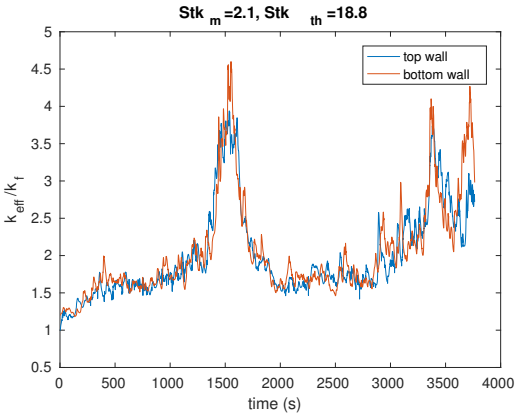


Figure 5.21: Instantaneous heat transfer based on the top wall flux and the bottom wall flux for a flow case in the laminar-turbulent transition regime.

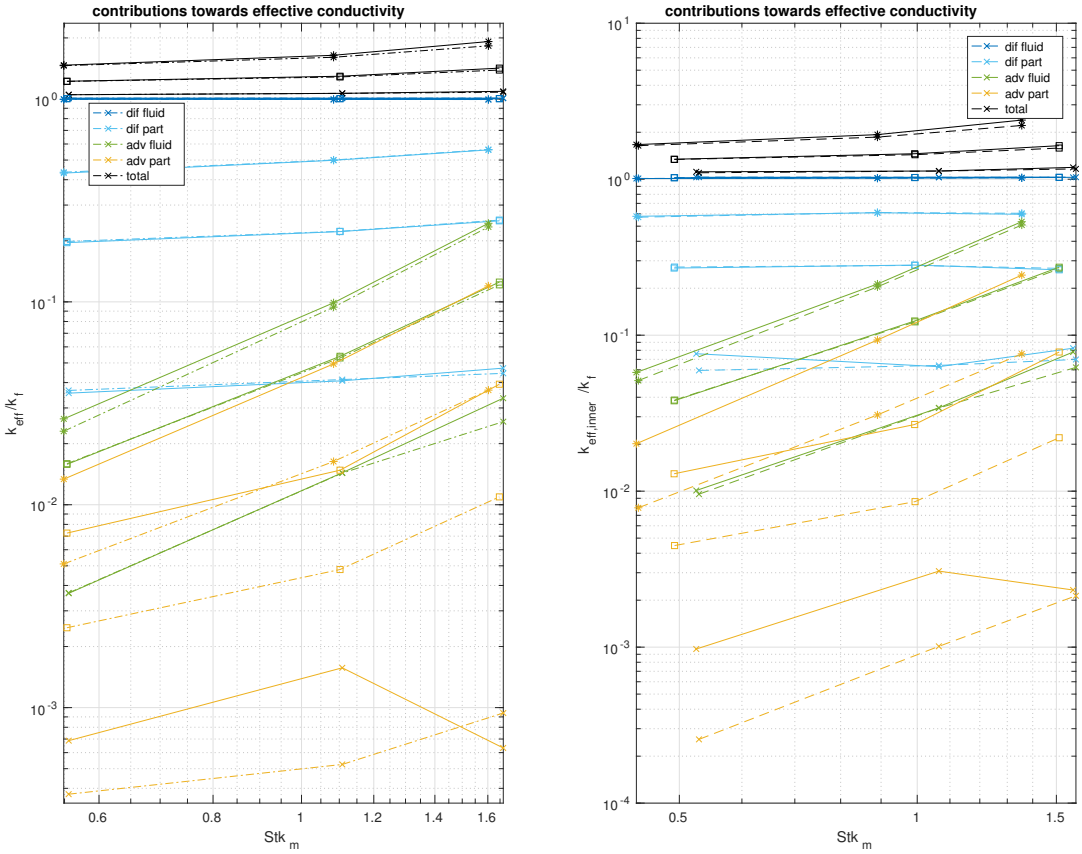


Figure 5.22: Contributions towards the overall thermal conductivity for 1% (x markers), 5% (square markers) and 10% (* markers) for thermal Stokes numbers of 3 (dashed line) and 9 (solid lines) times the mechanical Stokes number. Results for the full channel height on the left and centre of channel on the right.

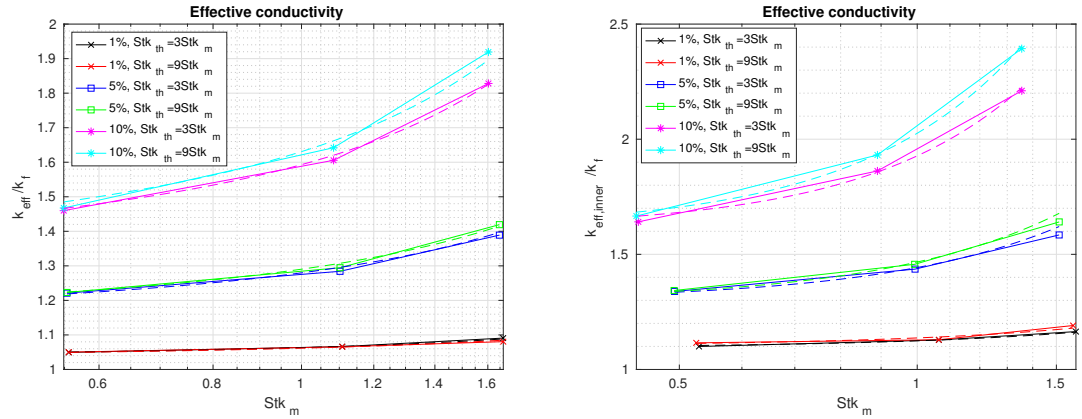


Figure 5.23: Effective heat conductivity for different particle concentrations in the fully laminar flow regime resulting from simulations (solid lines) and curve-fit (dashed line).

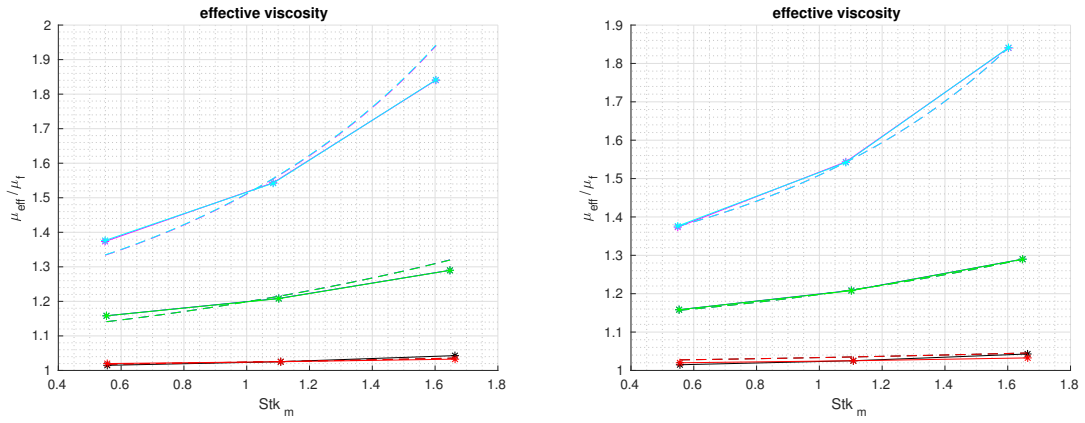


Figure 5.24: Comparison between fitted curve and simulation results with the curve for the effective viscosity based on the Eilers fit (left) and the corrected Eilers fit (right) for 1%, 5% and 10% concentrations.

## 5.8. EFFECTIVE VISCOSITY

Since not only a high thermal conductivity is important for efficient heat transfer but the increase in effective viscosity is also significant, in this section a more detailed look is given to the effect of the mechanical Stokes number onto the effective viscosity. An useful relation for predicting the behaviour of the viscosity of suspensions is, as also mentioned in the literature study, the Eilers fit [15]:

$$\frac{\mu_{eff}}{\mu_f} = \left(1 + B\frac{\phi_{eff}}{1-\phi_{eff}/\phi_{max}}\right)^2 \tag{5.8.1}$$

By using this equation with $\phi_{max} = 0.60$ and fitting it to the simulation results for the fully laminar channel flow, an expression for the effective particle concentration based on the influence of the mechanical Stokes number can be determined:

$$\phi_{eff} = \phi + A\,\phi Stk_m^{1.4} = \phi\left(1 + A\,Stk_m^{1.4}\right) \tag{5.8.2}$$

The results of this fit can be seen in figure 5.24. What can be seen is that, even though the general trend is the same, large deviations occur for low and high mechanical Strokes numbers. This can be corrected by introducing an extra dependence on the Stokes number in the maximum concentration, resulting in a better fit with:

$$\phi_{eff} = \phi(1 + A\,Stk_m^{1.5}) \tag{5.8.3}$$

$$\phi_{max} = 0.6 - C\,Stk_m^{0.5} \tag{5.8.4}$$

With the values A=0.4, B=1.15 and C=0.12. This relation is shown in figure 5.24. What can be seen is that this curve almost perfectly fits the simulation results for 5% and 10% suspensions. The viscosity still differs

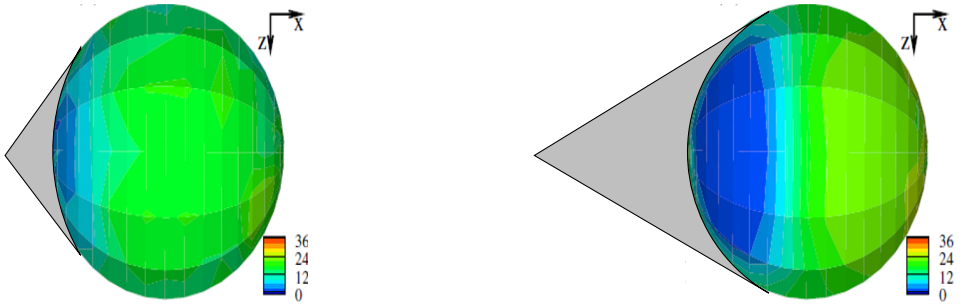


Figure 5.25: Results for the excluded volume for low Reynolds number (left) and high Reynolds number (right) particles, and thus low and higher Stokes number particles, from [15](colored spheres) and a rough indication of the effect of the excluded volume (shaded area) on the effective particle shape.

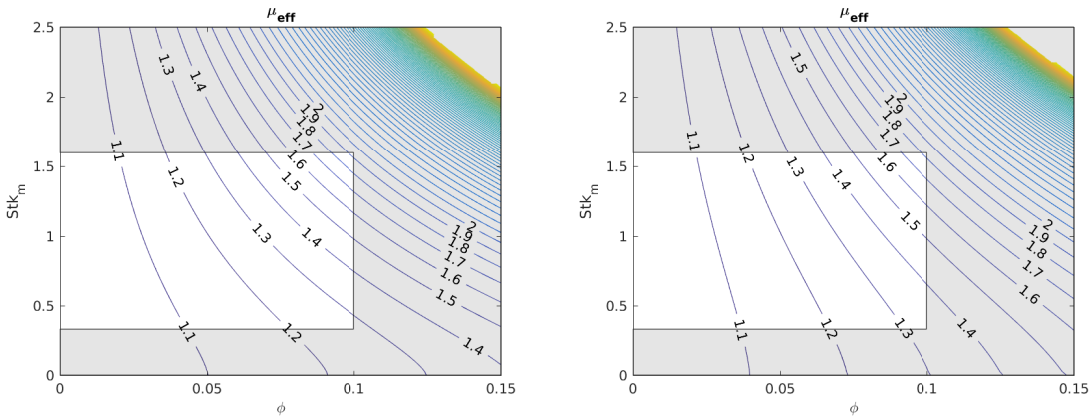


Figure 5.26: Effective viscosity based on the Eilers fit (left) and the corrected Eilers fit (right). Shaded region indicates that the properties are extrapolated, non shaded region means the properties are interpolated from the simulation results.

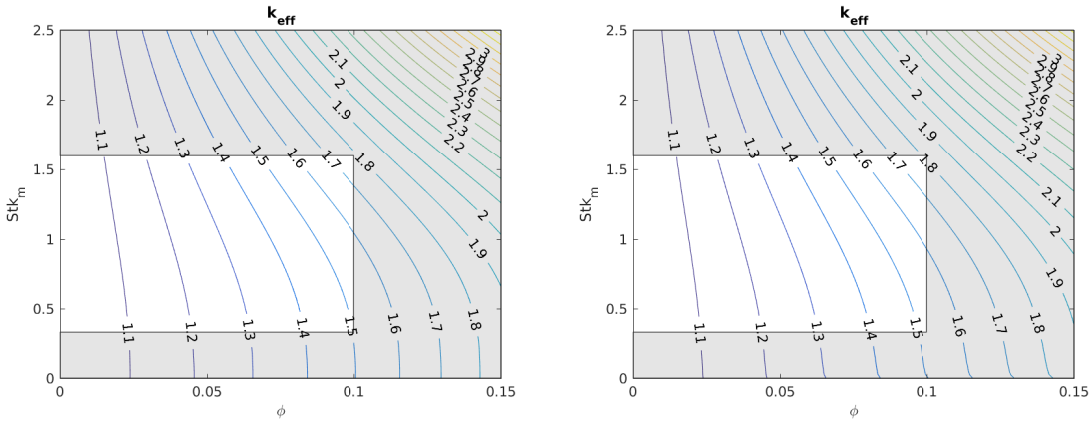


Figure 5.27: Effective conductivity based on curve fit for the fully laminar flow region for a thermal Stokes number of 0 (left) and 5 (right). Shaded region indicates that the properties are extrapolated, non shaded region means the properties are interpolated from the simulation results.

between the Eiler fit prediction and the simulation results for the 1% cases. This difference is probably due to the extremely low amount of particles, and thus the increased influence of the initial position of the particles.

The decrease in maximum concentration and increase in effective concentration can be explained with the results from [15]. The increase in effective concentration is due to the particles having an excluded region behind them where no other particles can exist. This effect is indicated in figure 5.25, where a rough indication of the shape of the excluded region is given.This might also explain the decrease in maximum possible concentration, since this excluded region changes the particles by adding a somewhat cone shaped shape to the back of the particles, which makes them stack less efficient, and thus have a deceased maximum concentration.

When looking back to the results used for the verification for the timescales in figure 5.17, it can be seen that the effective viscosity is dependent on the mechanical Stokes number and not directly on the Reynolds numberas long as the flow remains in the same flow domain, since a factor 3 difference between the same Stokes number different channel height cases exist. This indicates that the increase of the effective concentration being coupled by the Stokes number and not the Reynolds number seems to be correct.

With predictions for the effective conductivity (figure 5.27) and the effective viscosity (figure 5.26) being possible due to the determined relations, the ratio between the conductivity and viscosity can be determined. This results in the contours shown in figure 5.28. Even though between 10% and 20% the flow regime switches from laminar to inertial shear thickening and thus making the predictions less valid, he contours are determined up to a particle concentration of 15% to indicate the overall behaviour for denser suspensions. Similarly, a mechanical Stokes number of 2.5 might not be realistic while limiting the Reynolds number to stay in the laminar flow regime, but this region is given to make the influence of the Stokes number clearer.

The first thing that can be seen in these contour plots is that the same behaviour exists in the fully laminar regime compared to the inertial shear thickening regime: For large particle concentrations, the effective viscosity increases faster than the effective conductivity with increases in mechanical Stokes number. For a particle concentration of 15%, this ratio is bigger than one up to a mechanical Stokes number of 0.9 (for thermal Stokes number 0) and decreases fairly rapidly with increased Stokes number down to 0.4 for a mechanical Stokes number of 2.

For low particle concentrations, the dependence of the conductivity and viscosity on the Stokes number is much smaller. This results in a near to constant ratio for concentrations up to 1.5%. Both the influence of the particles and the influence of the particle collisions in this region are too low to significantly influence the viscosity and the conductivity. It can furthermore be noted that the effect of the thermal Stokes number in the fully laminar regime is low, increasing the ratio at most a few percent.

From this it appears that the highest conductivity over viscosity is reached for high concentration, low Stokes number suspensions. In this case, the particles have a low influence on the fluid and have little collisions and movement in height direction. This results in the effects of the convection of both the fluid and the particles towards the heat transfer being negligible, but also causes the mixing within the fluid to be reduced and thus have a lower wall friction. In this case, the main increase in the conductivity viscosity ratio is due to the increase in static conduction in the suspension by the addition of well-conducting particles.

This effect can also be seen in figure 5.29. This figure uses the relation 5.7.1, combined with the result from section 5.5.2 that the advection coefficients only slightly vary with the particle Biot number, to approximate the conductivity over viscosity ratio for suspensions with an equal fluid and particle conductivity. Since this figure gives results for particles with the same conductivity as the fluid, any enhancement in thermal conductivity, and thus an increase in conductivity viscosity ratio is due to the enhanced mixing by the presence of particles. The ratio is close to 1 for near to no particles, and only decreases with the addition of more particles. While increases in the Stokes number result in near to no change for low concentrations, These changes significantly decrease the ratio for higher Stokes numbers. This thus indicates that adding particles with a conductivity up to or lower than the fluid conductivity will not make the fluid more efficient in transferring heat when also considering the frictional losses.

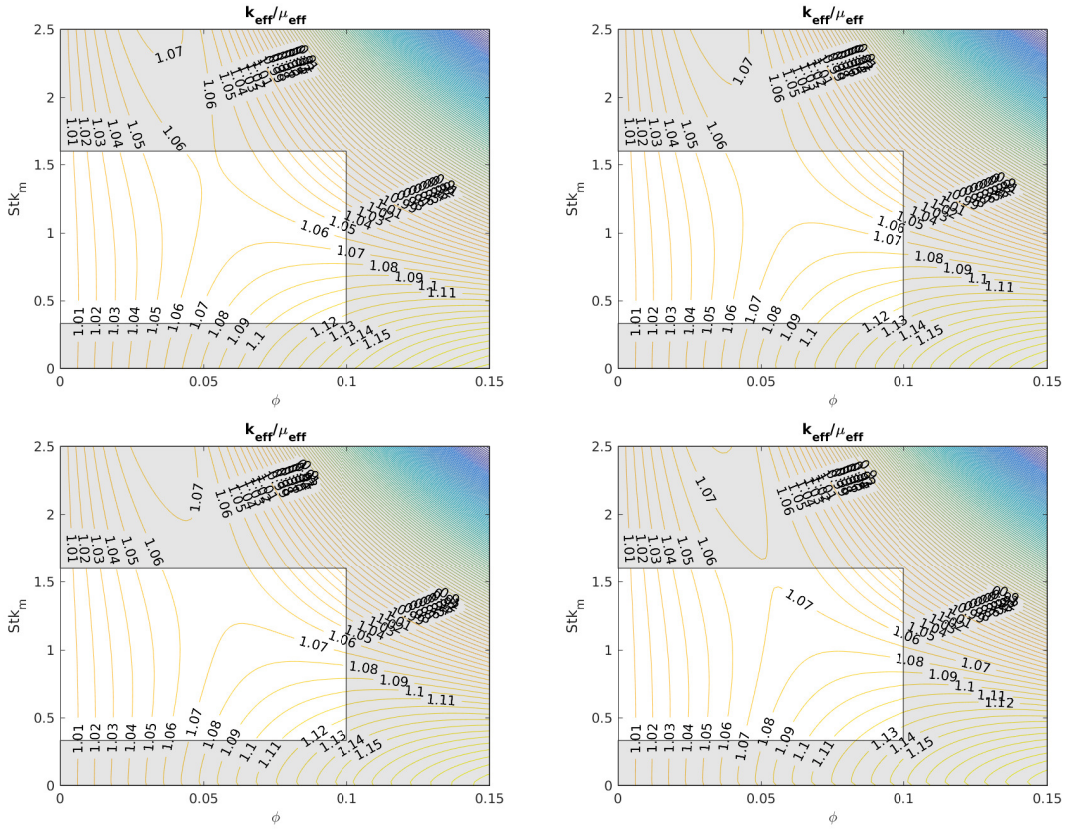


Figure 5.28: Ratio between the predicted effective conductivity and viscosity as function of the concentration and the mechanical Stokes number, for the thermal Stokes numbers of 0 (top left), 1 (top right), 2.5 (bottom left), and 5 (bottom right) for well-conducting (Biot 0) particles. Shaded region indicates that the properties are extrapolated, non shaded region means the properties are interpolated from the simulation results.

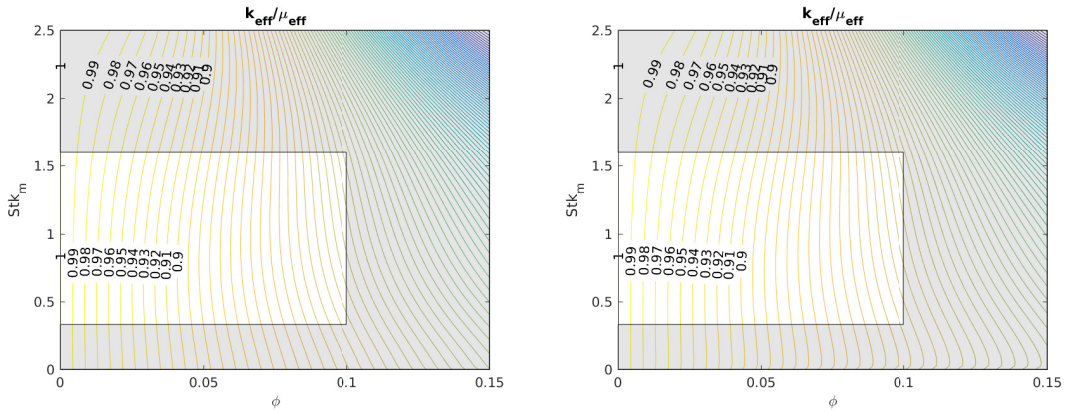


Figure 5.29: Ratio between the predicted effective conductivity and viscosity as function of the concentration and the mechanical Stokes number, for the thermal Stokes numbers of 0 (left), and 5 (right) for particles with a conductivity equal to the fluid. Shaded region indicates that the properties are extrapolated, non shaded region means the properties are interpolated from the simulation results.

# 6

# CONCLUSION AND RECOMMENDATIONS

The heat transfer in Couette channel flow for both dilute and more dense suspensions has been analyzed in the previous chapter. From this, it can be concluded that the non-dimensionalized thermal and mechanical timescales, the thermal and mechanical Stokes numbers, are important parameters for the effective conductivity for suspensions. Next to these parameters, the suspension concentration and the conductivity of the particles were also shown to play an important role.

For dense suspensions ($\phi = 0.2$) at low Stokes numbers, the main contribution towards the effective conductivity results from the addition of particles with a high conductivity. When well conducting particles are added, the effective conductivity will increase, while if particles with a lower conductivity than the fluid are added, the effective conductivity will decrease. When the mechanical Stokes number is increased, the particles start moving more in wall-normal direction due to particle-particle interactions. This also causes the fluid to mix more in height direction, and thus significantly enhancing the heat transfer due to fluid convection. Since the particles themselves also absorb and release heat, the particle convective heat transfer also starts becoming slightly more important for higher mechanical Stokes numbers, and increases significantly with increases in thermal Stokes number. This increase is due to the particles absorbing more energy when the thermal Stokes number is high, and thus transporting more thermal energy from the top hot wall to the bottom cold wall.

In the fully laminar dilute ($\phi \leq \approx 0.1$) suspension flow regime, the same effect exists as for dense suspensions, but due to the lower amount of particles, the overall contribution of the particle induced fluid convection and the particle advection is less. It is, however, possible to formulate a relation which, as function of not only the Stokes numbers but also the particle concentration and the non-moving suspension conductivity, predicts the effective conductivity. This equation confirms that the effects of the particles only start enhancing the heat transfer for higher Stokes numbers, while for very low Stokes numbers, the only enhancement to the effective conductivity is by increasing the non-moving conductivity.

When looking at the effective viscosity, the effect of the increased particle inertia due to an increased mechanical Stokes number can be included in the effective concentration and maximum concentration. This gives a good approximation of the effective conductivity, with which the ratio between the thermal conductivity and the viscosity were analyzed. What was seen is that for well-conducting particles, this ratio is only bigger than 1 for either low concentrations or low Stokes numbers, while for higher mechanical Stokes numbers the viscosity increases more than the conductivity. For ill-conducting particles however, the increase in effective viscosity is always larger compared to the increase in effective conductivity. This indicates that while it is possible to enhance heat transfer by introducing high Stokes number ill-conducting particles, it is only possible to give a bigger boost to the heat transfer compared to the friction by introducing highly conductive particles with either a low particle concentration (dilute suspensions), or a low mechanical Stokes number (particles behaving as tracer particles).

## 6.1. RECOMMENDATIONS

In this thesis, the influence of the mechanical and thermal Stokes number have been analyzed. The mechanical Stokes number has been verified to be an important parameter by changing the Reynolds number and the channel height. This has not been done for the thermal Stokes number. Thus it might be interesting to

do simulations with different Prandtl numbers. This will require analyzing the required grid size for different Prandtl numbers, and thus will also increase the understanding of the accuracy of the code.

What would be interesting to analyze in the future would be the turbulent flow regime. The complete analysis of this report is done for laminar flow, in which no mixing occurs without particles. This is in contrast to a turbulent flow, where mixing occurs naturally. This could possibly lead to the particles not causing any additional enhanced mixing and thus not causing any additional fluid convection. It might even be possible that by adding particles the fluid movement gets limited, causing a decrease in fluid convection and thus a decrease in effective conductivity due to the addition of particles.

It also might be interesting to look at the effects of density differences between the particles and the fluid. While this has been assumed to be nonexistent for this thesis, real particles with high thermal conductivity are mostly metals and thus have high densities compared to liquids. This density difference might cause the concentration near the bottom wall to be significantly higher compared to the top wall. This in turn will probably results in a difference in the heat transfer behaviour near the top and bottom wall. This might results in particle conduction being significant near the bottom wall. In contrast, near the top wall, less particles will appear and thus the effects of fluid conduction will probably be more significant. Furthermore, the lower particle concentration near the top wall might induce more mixing than the very high particle concentration near the bottom wall.

Another interesting effect to look at when looking at density differences is the effect of natural convection towards the effective conductivity. While this might not have significant influences on heat transfer with a hot top wall and a cold bottom wall, when the wall temperatures are exchanged, the natural convection in the fluid will probably cause an extra contribution towards the fluid convection in height direction and thus enhance the effective conductivity.

Finally it would be interesting to look at Poiseuille flow. While the flow used, Couette flow, allows for analyzing different flow regions due to having a close to constant shear rate in the centre, it is not a commonly used flow type for applications where heat transfer is important. A more realistic flow would be Poiseuille, pressure driven, flow between 2 flat plates. It might also be interesting to look at pipe flow instead of channel flow, since for practical applications pipe flow is more common than channel flow.

# BIBLIOGRAPHY


[1] M.N. Ardekani, O. Abouali, F. Picano, and L. Brandt. Heat transfer in laminar couette flow laden with rigid spherical particles. *Journal of fluid mechanics*, 2016.

[2] P.A. Berthelsen and O.M. Faltinsen. A local directional ghost cell approach for incompressible viscous flow problems with irregular boundaries. *Journal of computational physics*, 2008.

[3] W.P. Breugem. A second order accurate immersed boundary method for fully resolved simulations of particle laden flows. *Journal of computational physics*, 2012.

[4] S.K. Das, S.U.S. Choi, and H.E. Patel. Heat transfer in nanofluids - a review. *Heat transfer engineering*, 2006.

[5] N.G. Deen, E.A.J.F Peters, J.T. Padding, and J.A.M. Kuipers. Review of direct numerical simulation of fluid–particle mass, momentum and heat transfer in dense gas–solid flows. *Chemical Engineering Science*, 2014.

[6] A. Einstein. Bemerkung zu der abhandlung von w. r. heß „beitrag zur theorie der viskosität heterogener systeme. *Kolloid-Zeitschrift*, 1920.

[7] S. Haeri and J.S. Shrimpton. On the application of immersed boundary, fictitious domain and body-conformal mesh methods to many particle multiphase flows. *International journal of multiphase flows*, 2011.

[8] K.Luo, Z. Wang, J. Fan, and K. Cen. Full-scale solutions to particle-laden flows: Multidirect forcing and immersed boundary method. *Physical review*, 2007.

[9] J.G.M Kuerten, C.W.M van der Geld, and B.J. Geurts. Turbulence modifications and heat transfer enhancements by inertial particles in turbulent channel flow. *Phys fluids*, 2011.

[10] I. Lashgari, F. Picano, W.P. Breugem, and L. Brandt. Channel flow of rigid sphere suspensions: Particle dynamics in the inertial regime. *International journal of multiphase flow*, 2015.

[11] B. Metzger, O. Rahli, and X. Yin. Heat transfer across sheared suspensions: The role of shear-induced diffusion. *Journal of fluid mechanics*, 2013.

[12] E.E. Michaelides, C.T. Crowe, and J.D. Schwarzkopf. Multiphase flow handbook. 2017.

[13] A.F. Mills. Basic heat and mass transfer. 1999.

[14] M.H. Nakhei and B. Lessani. Effect of solid inertial particles on the velocity and temperature statistics of wall bounded turbulent flow. *International journal of heat and mass transfer*, 2016.

[15] F. Picano, W.P. Breugem, D. Mitra, and L. Brandt. Shear thickening in non-brownian suspensions: An excluded volume effect. *Physical review letters*, 2013.

[16] K. Pietrak and T.S. Wisniewski. A review of models for effective thermal conductivity of composite materials. *Journal of power technologies*, 2015.

[17] C. Santarelli and J. Frohlich. Immersed boundary methods for heat transfer. *International journal of numerical methods for heat and fluid flow*, 2016.

[18] A. Shakibaeinia and Y.C. Jin. Mesh-free lagrangian modeling of multiphase flow. *CFD society of Canada*, 2012.

[19] W. Shyy, H.S. Udaykumar, M.M. Rao, and R.W. Smith. Computational fluid dynamics with moving boundaries. 1996.

[20] H. Tavassoli, S.H.L. Kriebitzsch, M.A. van der Hoef, E.A.J.F. Peters, and J.A.M. Kuipers. Direct numerical simulation of particulate flow with heat transfer. *International journal of multiphase flows*, 2013.

[21] Y.H. Tseng and J.H. Ferziger. A ghost-cell immersed boundary method for flow in complex geometry. *Journal of computational physics*, 2003.

[22] M. Uhlmann. An immersed boundary method with direct forcing for the simulation of particulate flows. *Journal of computational physics*, 2005.

[23] P. Warrier, Y. Yuan, M.P. Beck, and A.S. Teja. Heat transfer in nanoparticle suspensions: Modeling the thermal conductivity of nanofluids. *AIChE Journal*, 2010.

[24] J. Xia, K. Luo, and J. Fan. A ghost-cell based high-order immersed boundary method for inter-phase heat transfer simulation. *International journal of heat and mass transfer*, 2014.

[25] J. Xia, K. Luo, and J. Fan. Simulating heat transfer from moving rigid bodies using high-order ghost-cell based immersed-boundary method. *International journal of heat and mass transfer*, 2015.

[26] F. Zonta, C. Marchiolo, and A. Soldate. Direct numerical simulation of turbulent heat transfer modulation in micro-dispersed channel flow. *Acta Mechanica*, 2008.